

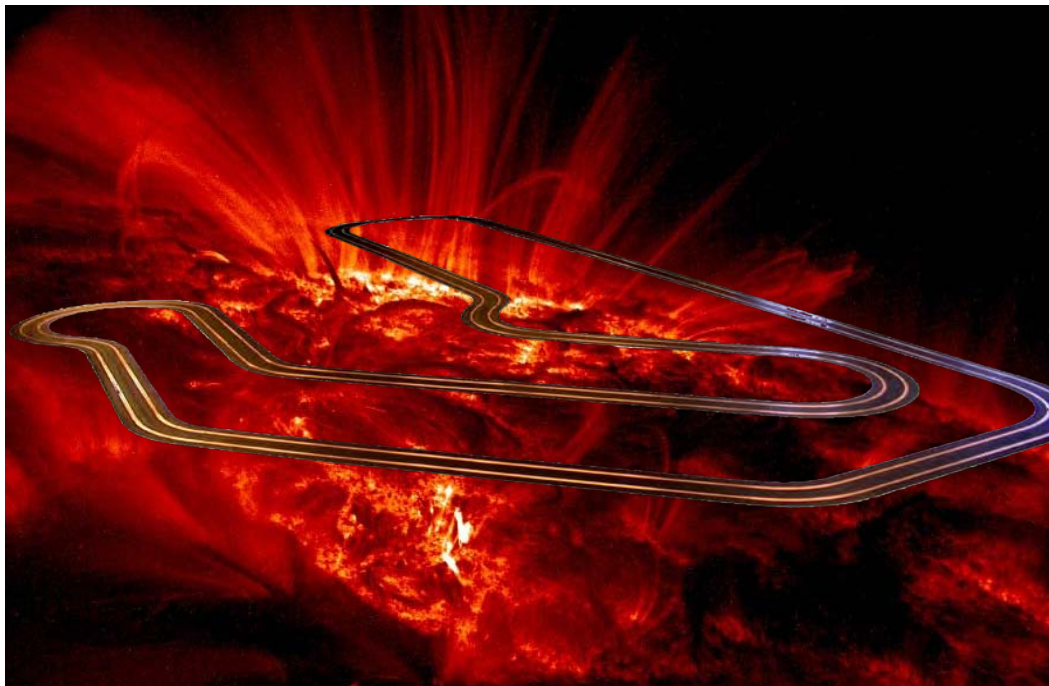


# PhD thesis

Jakob Jakobsen

## Kinematic GNSS:

Ionospheric variations and characteristics of multipath



Academic advisor: Carl Christian Tscherning

Submitted: 15/09/10



# Preface

This thesis is a summary of the work performed during the time period of my Ph.D. study. Most of the work performed is based on 4 papers, where some of the subjects has been updated and extended in order to provide an up-to-date version. Furthermore is the work performed based on an ESA project *Study and Modelling of Ionospheric Propagation Impairments at C-Band*, which was a part of the ESA GNSS Evolution Program. The 4 papers are listed below and can be read in full length in the appendices.

- Jakobsen J, Knudsen P, Jensen A (2008) Principle component analysis on absolute TEC values and its impact on Kalman filtering when using a priori information. *Proceedings of the 2008 National Technical Meeting of The Institute of Navigation*. (7):884-892, July 2008.
- Jakobsen J (2009) A new method for evaluation of the ionospheric modeling error in a VRS based network RTK service. *Proceedings of the 22nd International Technical Meeting of The Satellite Division of the Institute of Navigation (ION GNSS 2009)*, pages 2689-2695, September 2009.
- Jakobsen J, Pedersen SM (2009) Design of a GNSS kinematic slotcar test track. *Proceedings of the 13th IAIN World Congress in Stockholm. Published by the Nordic Institute of Navigation*, October 27-29 2009.
- Jakobsen J, Knudsen P, Jensen A (2010) Analysis of local ionospheric time varying characteristics with singular value decomposition. *Journal of Geodesy* 85(7) pages 449-456, <http://dx.doi.org/10.1007/s00190-010-0378-2>.

In the report is used a variety of abbreviations or acronyms, which is related to GNSS. Where not specified, the reader is referred to the homepage, <http://www.heisesgade.dk>, where an extensive list of GNSS related abbreviations are present.

This thesis would not have been the same without the financial help, scientific contributions, and support from a number of people and organisations. Among these special thanks go to

- My supervisors in Denmark: Carl Christian Tscherning, Anna B. O. Jensen and Per Knudsen
- My supervisor and the PLAN group at the University of Calgary Professor Gérard Lachapelle and Aiden Morrison
- The Geodesy department at DTU Space especially Finn Bo Madsen
- The Electronics and Mechanics department at DTU Space: Søren Møller Pedersen and Michael Hassel Avngaard
- The National Survey and Cadastre: Lolita Bahl and Casper Jepsen
- The University of Copenhagen
- My family, Mette Eklund Jakobsen, Noah Eklund Jakobsen, and Johan Eklund Jakobsen

---

Jakob Jakobsen

# Abstract

This thesis is focusing on two of the largest factors, which affect the GNSS signals on their way from the satellite transmitter to the receiver on the ground. This is the variation of the ionosphere and a characterisation of indoor multipath.

It is shown, how singular value decomposition can be used to separate the yearly and daily signal on a computed TEC time series, which locally cover the area of Denmark. Furthermore is it shown, how the analysis can be used to partly generate a local model of the variation of the ionosphere, and partly how the deviations from this model can be correlated with local geomagnetic observations. Thereby make a better foundation for detecting abnormalities in the ionosphere.

Private network RTK services are modelling the ionospheric contribution to GNSS signal over a large geographic area. A new method for evaluation of the service ionospheric modelling performance independent of a rover is presented. Furthermore are a number of dependencies shown for the ionospheric modelling error at an operating network RTK service provider. The dependencies are related to the satellite elevation angle, the distance to nearest reference station, the geographic location in the extrapolation area, and the general daily ionospheric activity.

An increasing number of new GNSS related applications demand positioning and navigation under more and more challenging GNSS conditions, especially indoor. Under these conditions the GNSS signals are heavily affected and the signal to noise ratio of each satellite link varies, especially under kinematic conditions. The design of a slot car track, which purpose is to control the kinematic behaviour of an object and provide the absolute coordinate to any given instance of time with a great accuracy, is presented in details.

Kinematic tests with this 27m test platform has been performed with two simultaneously cars, attached with a High Sensitivity GNSS receiver. The tests are performed indoor with speeds controlled in the interval of 0.6 to 1.8 m/s. Static tests are performed for comparison reasons. A characteristic of the multipath interference, in form of an analysis of the carrier to noise ratio as well as the influence in the positioning domain, is given both for the static and the kinematic case.

# Resume på dansk (Abstract in danish)

Denne afhandling fokuserer på to af de største faktorer, der påvirker GNSS signaler under deres vej fra GNSS satellitten til modtageren på Jorden. Det drejer sig om variationen i ionosfæren samt en karakterisering af multipath forstyrrelser i indendørs miljøer.

Det påvises, hvorledes singular value decomposition kan benyttes til at separere det årlige og daglige signal på en beregnet TEC tidsserie gældende lokalt for Danmark. Det vises desuden, at analysen kan benyttes dels til at lave en generel model af variationen af TEC, samt at afvigelser fra denne model kan korreleres med lokale geomagnetiske målinger og derved danne et bedre grundlag for detektering af forstyrrelser i ionosfæren.

Private netværks RTK tjenester modellerer bidraget fra ionosfæren over større områder. En ny metode til evaluering af tjenestens ionosfære modellering uafhængig af en RTK rover præsenteres. Desuden påvises der en række sammenhænge til en tjenestes fejlmodellering. Disse er en afhængighed af elevationsvinklen, en afstand til nærmeste referencestation, en geografisk placering i extrapolationsområdet, samt variationen af den generelle daglige ionosfæreaktivitet.

Et stadig støt stigende antal nye GNSS relaterede applikationer kræver positionering under mere og mere vanskelige GNSS forhold herunder indendørs positionering. Under disse forhold påvirkes GNSS signalerne kraftigt og deres signal støjforholdet varierer, specielt under kinematiske forhold. Design af en racerbane, med det formål at kunne styre et objekts kinematiske opførsel med så stor kontrol, at dets absolutte koordinat til enhver given tid kan bestemmes med stor nøjagtighed, præsenteres i detaljer.

Kinematiske forsøg med denne 27m testplatform er foretaget med to simultane biler, påmonteret en High Sensitivity GNSS modtager. Forsøgene er foretaget indendørs med kontrollerede hastigheder imellem 0.6 og 1.8 m/s. Til sammenligning er der desuden foretaget statiske forsøg. En karakterisering af multipathforstyrrelsen er foretaget i form af en analyse af signalstøjforholdet, samt en evaluering i positionsdomænet. Dette gælder både for de statiske samt de kinematiske forsøg.



# Contents

<b>Preface</b>	<b>i</b>
<b>Abstract</b>	<b>iii</b>
<b>Resume på dansk</b>	<b>v</b>
<b>Contents</b>	<b>vii</b>
<b>List of figures</b>	<b>xi</b>
<b>List of tables</b>	<b>xv</b>
<b>1 Introduction and Motivation</b>	<b>1</b>
<b>2 Ionospheric variations</b>	<b>5</b>
2.1 Morphology . . . . .	6
2.1.1 Height characteristics . . . . .	6
2.1.2 Geographic characteristics . . . . .	8
2.2 Observed variations of the ionosphere . . . . .	9
2.2.1 Time varying parameters . . . . .	9
2.2.2 Ionospheric bubbles . . . . .	11
2.2.3 TID . . . . .	17
2.3 Effect on satellite navigation signals . . . . .	18
2.3.1 General first order effects . . . . .	18
2.3.2 Scintillation effects . . . . .	21
2.4 Models of the Total Electron Content . . . . .	26
2.4.1 Klobuchar . . . . .	26
2.4.2 NeQuick . . . . .	27
2.4.3 GIM . . . . .	29
	<b>vii</b>

2.5	Generation of local vertical TEC time series . . . . .	30
2.6	Identify local time varying characteristics . . . . .	33
2.6.1	Strength of the TEC signal . . . . .	33
2.6.2	SVD . . . . .	34
2.7	Use of models . . . . .	39
2.7.1	Recomposition of yearly models . . . . .	39
2.7.2	Correlation with geomagnetic measurements . . . . .	40
2.7.3	Implementations in the kalman filter calculation . . . . .	42
2.8	Ionospheric model error in a NRTK service . . . . .	43
2.8.1	Different NRTK solutions . . . . .	44
2.8.2	Model error of the ionospheric correction in a VRS NRTK . . . . .	45
2.8.3	Extracting the variation of the model error . . . . .	47
2.8.4	Real time data collection for the VRS . . . . .	48
2.8.5	Post processed data collection for the VRS . . . . .	49
2.8.6	Verification of the method . . . . .	50
2.8.7	Elevation angle dependency . . . . .	52
2.8.8	Day to day variation . . . . .	54
2.8.9	Dependency on the distance to nearest reference station . . . . .	55
2.9	Conclusion on ionospheric variation effects . . . . .	56
<b>3</b>	<b>Characteristics of multipath</b>	<b>59</b>
3.1	Effects on GNSS signals . . . . .	59
3.1.1	Pseudorange error . . . . .	62
3.2	HS GNSS . . . . .	63
3.3	Controlled kinematic behaviour . . . . .	65
3.3.1	The design of the slot car track . . . . .	66
3.3.2	Time synchronization . . . . .	78
3.3.3	Registration of time to a sensor . . . . .	79
3.3.4	Computer controlled speed . . . . .	79
3.3.5	Exported data . . . . .	80
3.3.6	Verification . . . . .	80
3.4	Tests and methodology . . . . .	82
3.4.1	Scenario . . . . .	82
3.4.2	Testing equipment . . . . .	83
3.4.3	Assembled track and surveying . . . . .	83
3.4.4	Data collection flow and methodology . . . . .	85
3.5	Results . . . . .	88

3.5.1	Static characteristics . . . . .	88
3.5.2	Kinematic characteristics . . . . .	92
3.6	Conclusion on characteristics of multipath . . . . .	98
<b>4</b>	<b>Conclusion and perspectives</b>	<b>101</b>
	<b>Bibliography</b>	<b>103</b>
	<b>Appendix A: Principle component analysis on absolute TEC values and its impact on Kalman filtering when using a priori information</b>	<b>111</b>
	<b>Appendix B: A new method for evaluation of the ionospheric modeling error in a VRS based network RTK service</b>	<b>121</b>
	<b>Appendix C: Design of a GNSS kinematic slotcar test track</b>	<b>129</b>
	<b>Appendix D: Analysis of local ionospheric time varying characteristics with singular value decomposition</b>	<b>139</b>



# List of Figures

2.1	The deflection of the solar wind against the magnetic field . . .	5
2.2	Ionospheric layers and electron density day and night . . . . .	7
2.3	Major geographic regions of the ionosphere . . . . .	8
2.4	Monthly averaged sunspot numbers from 1850 to 2010 . . . . .	10
2.5	Example of a plume generation . . . . .	13
2.6	5 sectors divided by their geographic longitude . . . . .	15
2.7	Monthly occurrence rates of plasma bubbles from 2000 - 2006	16
2.8	Illustration of the single layer model of the ionosphere . . . . .	21
2.9	Illustration of the scintillation phenomena . . . . .	22
2.10	Global variation of amplitude fading in scintillations during solar maximum and minimum conditions . . . . .	22
2.11	Example of $S_4$ as function of latitude [ $^\circ$ ] of the ionospheric pierce point and local solar time [hour] for Ny Alesund at 78.9 $^\circ$ latitude November 20th and 21st 2003. . . . .	23
2.12	Probability density functions for $S_4$ for Ny Alesund November 20th and 21st 2003. . . . .	24
2.13	Example of the daily variation of TECU using the Klobuchar model . . . . .	28
2.14	Example of a vertical TEC map using NeQuick 2 . . . . .	29
2.15	Example of a global ionospheric map . . . . .	31
2.16	Example of the computed vertical TEC time series for three summer and three winter days in 2001, 2004, and 2007 . . . . .	32
2.17	Histogram of residual data . . . . .	33
2.18	Power spectrum for the TEC time series from 1999 - 2009 . . .	34
2.19	Strength of the TEC signal from 1999 - 2009 . . . . .	35
2.20	The <b>U</b> and <b>V</b> matrixes for the first singular value for 11 years	36
2.21	First five singular values in the <b>S matrix</b> . . . . .	37
2.22	The <b>U</b> and <b>V</b> matrixes for the second singular value for 11 years	38

2.23	The $\mathbf{U}$ and $\mathbf{V}$ matrixes for the third singular value for 11 years	39
2.24	Recomposed ionospheric models for 2001, 2004 and 2007. . . .	40
2.25	Two events in 2001 . . . . .	41
2.26	The initialisation time with and without using a priori information. . . . .	42
2.27	The general processes involved in NRTK services and the relation between the different solutions . . . . .	44
2.28	The procedure for calculating a position using the VRS approach separated into two segments . . . . .	46
2.29	1 dimensional illustration of the NRTK service ionospheric model error. . . . .	46
2.30	The procedure for collecting real time data from a NRTK service provider . . . . .	48
2.31	Location of the selected stations . . . . .	50
2.32	Example of a satellite pass . . . . .	52
2.33	Standard deviation of the model error for two stations with different distance to nearest reference station. . . . .	53
2.34	The daily TEC cycle for two days in 2009 . . . . .	53
2.35	Mean standard deviation for visible satellites of the ionospheric model error for two days for the station 39.7 km. from the nearest reference station. . . . .	54
2.36	Mean standard deviation for visible satellites of the ionospheric model error for stations in the interpolation area . . .	55
2.37	Mean standard deviation for visible satellites of the ionospheric model error for stations in the extrapolation area. . .	56
3.1	Indoor multipath environment. . . . .	59
3.2	In-phase and out-of-phase reflected carrier relative to the direct ray . . . . .	62
3.3	Correlation peak in the presence of constructive and destructive interference . . . . .	63
3.4	Bounds on the C/A code pseudorange error due to multipath for different correlator spacing . . . . .	64
3.5	Sequential coherent integration . . . . .	65
3.6	Overall system design of the slot car track. . . . .	67
3.7	Top and bottom side of a plate. . . . .	68

3.8	Schematic illustration of the entry and exit radiuses for the 90° turn plate. . . . .	68
3.9	The RTR slot car fully equipped with GNSS testing equipment. . . . .	69
3.10	Electrical diagram of the position sensors implementation. . . . .	70
3.11	Print of position sensor. . . . .	70
3.12	Electrical diagram of the motor control implementation. . . . .	72
3.13	The microcontroller box. . . . .	73
3.14	Illustration of noise spikes on a signal line. . . . .	74
3.15	The control panel. . . . .	75
3.16	Main window for the logging software. . . . .	77
3.17	The time synchronisation procedure. . . . .	78
3.18	Round detection principle. . . . .	79
3.19	The procedure used for verification of the interpolation. . . . .	81
3.20	Building used for the tests . . . . .	82
3.21	The assembled car. . . . .	84
3.22	The location of the assembled track and skyplot for the visible considered satellites . . . . .	85
3.23	The assembled track inside the building and illustration of the length for the outer lane . . . . .	86
3.24	The data flow during the collection phase. . . . .	87
3.25	The DOPs and fading values per SV in a time window of 7 minutes and 10 seconds. . . . .	88
3.26	Static influence of multipath in a time window of 7 minutes and 10 seconds . . . . .	89
3.27	Static influence of multipath on the height component in a time window of 7 minutes and 10 seconds . . . . .	90
3.28	Static influence of multipath in point 039 and 152 . . . . .	91
3.29	Length and horizontal distribution of fading [dB] for two selected SV for 7 rounds at speed 1.6 m/s for the outer lane. . . . .	93
3.30	Fading for SV 15 for two lanes for 6 rounds with speed at 1.0 m/s . . . . .	94
3.31	Horizontal distribution of fading for SV 15 for two lanes for 6 rounds with speed at 1.0 m/s. . . . .	95
3.32	Histogram of differenced fading values for two selected satellites and three selected speeds. . . . .	95
3.33	Example of horizontal distribution of positions for the outer lane for round number 4 for speed 1.2 m/s . . . . .	96

3.34 Example of height measurement for the dataset in figure 3.33. 97



# List of Tables

2.1	Three classes of TIDs . . . . .	17
2.2	First order time and range delay for a selected group of GNSS signals and a possible future signal in the C-band . . . . .	20
2.3	Mean time to loose lock for selected RMS tracking error variance values . . . . .	26
2.4	Correlation coefficients for the singular values for each year and the yearly mean sunspot number . . . . .	37
2.5	The result of a PP baseline between a VRS and a physical reference station. . . . .	51
3.1	Material effects on the GPS L1 LOS propagation measurement.	60
3.2	Average and max. velocities of the car for two setups. . . . .	70
3.3	Offsets and standard deviations (mean value) for the four points in the static analysis . . . . .	90
3.4	Offsets and standard deviations (mean value) for the position differences . . . . .	97



# Chapter 1

## Introduction and Motivation

As GNSS signals travel from the satellite transmitter to the receiver antenna they are affected by many parameters. These include atmospheric effects, effects related to the nearby surroundings as well as hardware specific effects in the receiving equipment. In case of indoor navigation are the signals furthermore affected by penetrating through the materials of the building. Common to these is that they can all affect the calculated position and thus can have an influence on the position accuracy.

*This thesis is focusing on two of the largest effects which are related to the variation in the ionosphere and the characteristics of indoor code multipath.*

The ionospheric effect on the satellite signals will cause an error that must be handled in the positioning process when GNSS is used for positioning and navigation. With data from permanently continuously operating GNSS reference stations, can the ionospheric effect be extracted and used for ionospheric modelling. Several techniques for estimation of the Total Electron Content (TEC) exist, see for instance Komjathy (1997a).

The TEC has different time varying characteristics for different latitudes, thus an important factor for obtaining a local accurate model is to use data from local GNSS reference stations. Precise ionospheric modelling will improve the accuracy of the position of single frequency GNSS receivers. Furthermore is precise ionospheric modelling also important for other space

based observation systems as well as communication systems and space weather studies. The observed rapid evolution of the ionosphere currently defies sufficient modelling to allow its prediction to future time epochs and therefore is studies of its time varying behaviour needed.

Over the last several years has the number of Network Real Time Kinematic, NRTK, services increased. The advantages of modelling the different error sources present over a large geometric area have shown its great potential. Many of these services cover the same area and they are based on software from private companies. The handling of the error sources in these services is proprietary information as well as the implemented modelling algorithms. An end user needs parameters in order to evaluate or to compare NRTK services before he/she can choose the most appropriate NRTK service in his/her coverage area. Evaluation or comparison between NRTK services is mostly done in the positioning domain, which includes the rover equipment. The rover equipment on the market today, consists of receivers with different brands, different age, different firmware version and different antenna, which all have an effect on the position accuracy. A full evaluation of a NRTK service would include all these differences. Therefore is an evaluation of the NRTK service independent of the rover needed. A new method to evaluate the NRTK service independent of the rover will be addressed focusing on evaluating the variation of ionospheric modelling error.

Conventional GNSS theory is limited to applications where signals have a direct line of sight (LOS) between the satellite and the receiver, and thus not applicable to environments with highly attenuated signals. However the demand for Location Based Services (LBS), safety and rescue application related to the emergency call services E-112 and E-911, and personal navigation indoor in general has been the driving factor for research and development of enhanced civilian GNSS receivers. The ever increasing new applications demand operation in increasingly difficult operational GNSS environment. Receivers with longer integration time assisted with external possibilities for acquiring the navigation message has been developed. It opens for the possibility to lower the acquisition and tracking power threshold to levels where even indoor operation is possible. Signals in these environments are highly attenuated with fluctuating carrier to noise ratio and can introduce errors on the pseudorange which leads to large positioning errors. The deterioration can be caused by many factors such as obstructions from buildings or foliage,

---

interference from reflected signals, signal self-interference, jamming, antenna effects, and receiver implementation losses, and the impact of one of these can result in partial or total loss of signal tracking or tracking errors.

Signal analysis and performance under various indoor conditions have been researched over the last couple of years. Also different techniques for weak signal tracking using High Sensitivity (HS) receivers has been performed, see for instance Watson et al (2006), Lachapelle et al (2004), and Borio and Lachapelle (2009). Common to these analyses is that the indoor performance is focused on static conditions. The lack of a kinematic test platform, which can control the kinematic behaviour of the measuring/testing equipment in a certain defined geometry, currently limits the ability to characterise the multipath inference under these circumstances. Such a test platform has therefore been produced in order to characterise the multipath interference effect under kinematic conditions.

This thesis is divided into two main chapters each covering the two areas of focus. In the variation of the ionosphere chapter a general description of the time varying characteristics as well as observed variations of the ionosphere will be given. This is followed by a description of the effects on satellite navigation signals and a literature review of three existing TEC models. Then it is described how the time varying characteristics can be extracted based on the generation of a local TEC time series and how they can be recomposed in order to be used in detecting abnormal variations and as a priori information in the TEC calculation procedure. In the end is given a description of how the ionospheric model error within a Network RTK system can be extracted and how it correlates with the different identified variations in the TEC.

In the characteristics of multipath chapter is first described the effects on GNSS signals in indoor environment and how this relates to pseudorange errors. Then a brief introduction is given to High Sensitivity (HS) receivers and the processing required in order to obtain acquisition and tracking for weak signals. This is followed by a full description of the produced kinematic slot car track and the control of the kinematic behaviour as well as a verification of the procedure. In the end of the chapter are the results of the indoor tests presented in terms of signal fading and the effect of multipath interference in the positioning domain. The characteristics for both static and kinematic are also given.

In the end is given an overall conclusion and perspectives related to the investigated subjects.

## Chapter 2

### Ionospheric variations

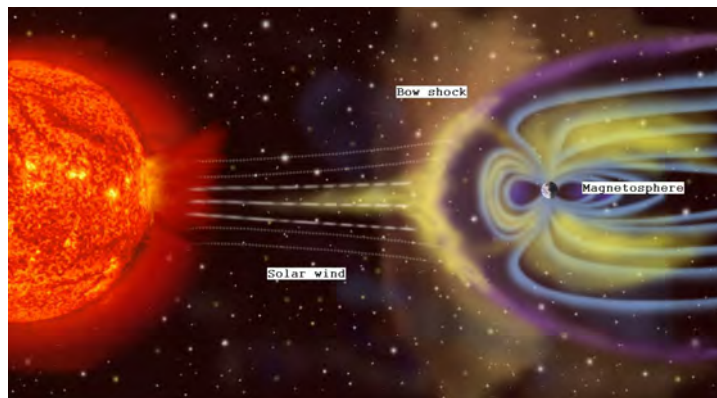


Figure 2.1: The deflection of the solar wind against the magnetic field, <http://sec.gsfc.nasa.gov/popscise.jpg>.

The Earth magnetic field in a simplified manner can be described as a dipole with magnetic field lines surrounding the Earth. The strength of the field decrease as the distance to the Earth increase. When a magnetic field is present within an electric conductor it takes time to change the magnetic field, it is said to be "frozen in", and for the same reason a magnetic field cannot quickly penetrate into a highly conductive body. This is what happens with the solar wind as it is an electric conductor. This is how the geomagnetic field prevents particles from the solar wind from entering the Earth atmosphere. The geomagnetic field cannot penetrate into the flow of particles, and the particles are thus trapped in the solar wind and are diverted around the

Earth. The phenomenon is called the bow shock, see figure 2.1.

The bow shock is characterised by compressed field lines on the day side and on the night side is the field decompressed and reach out to distances of 100 times the Earth radius. The magnetosphere confined by the deformed Earth magnetic field is strongly influenced by the dynamic coupling with the interplanetary magnetic field, IMF, and therefore determined by the characteristics of the solar wind. Normally are the geomagnetic field lines closed, but interactions with the IMF can happen, when the Z-component of the IMF becomes negative. In this situation is the IMF in a southward direction interacting with the north directed geomagnetic field lines. This opens the magnetosphere, and particles from the solar wind can enter the geomagnetic field through the night side of the magnetosphere and in the polar regions. The result is an increased ionization.

The source for the solar wind is the sun's outermost region, the corona, which by convection and radiative transport processes establishes the particle content and magnetic relations of the solar wind. These solar processes have large variations in time, energy and orientation. The variations of the magnetosphere, caused by the interaction with the solar wind, are in turn also observed in the ionosphere.

The ionosphere is the region of the atmosphere covering the altitude from app. 60-1000 km. above the surface of the Earth. It consists of an equal amount of free electrons and positively charged ions, which means that overall the ionosphere is considered to be neutral. It is ionized by the short wavelength part of the solar radiation (UV and soft X-ray) and to some extent also by particle precipitation. This means that the ionization state has large diurnal variations with maximum electron densities in the sunlit sector of the Earth.

## **2.1 Morphology**

### **2.1.1 Height characteristics**

The ionosphere can be divided in the vertical direction into four layers based on the electron density shown in figure 2.2.



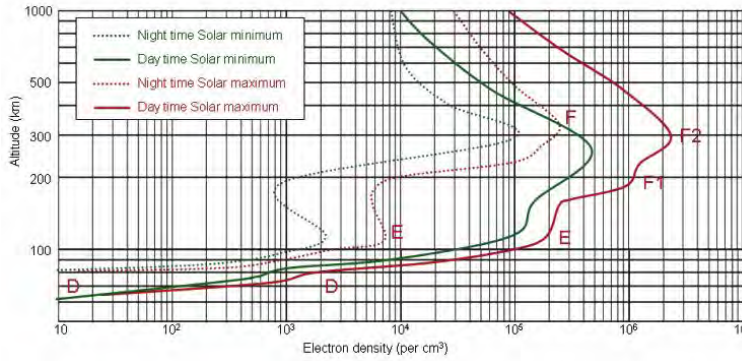


Figure 2.2: Ionospheric layers and electron density day and night, Papon et al (2010).

- **D layer:** Ranging from 60-90 km. and electron density from  $10^8 - 10^{10}$  electrons  $m^{-3}$ . Normally has this layer very little effect on GNSS signals. The layer tends to vanish at night.
- **E layer:** Ranging from 105-160 km. and electron density on several  $10^{11}$  electrons  $m^{-3}$ . This layer is characterized by the presence of irregularities in the electron density at high latitudes in the auroral region. These irregularities can effect the signal propagation significantly. The layer becomes much weaker during the night.
- **F1 layer:** Ranging from 160-180 km. and electron density on several  $10^{12}$  electrons  $m^{-3}$ . This layer is characterized by large electron density and it tends to vanish at night.
- **F2 layer:** Ranging from 180-1000 km. and electron density up to several  $10^{12}$  electrons  $m^{-3}$ . This layer is also characterized by having large electron density and the maximum intensity of electrons is located in this layer, at app. 300-400 km. altitude. Therefore the largest effect on GNSS signals happens in this layer. The upper part of the F2 layer does not vanish significantly in the night time.

The D-layer has almost the same densities and shape regardless of solar minimum or maximum. The E, F1, and F2 layers have the same characteristic profile, but they are magnified during high solar activity, Johnson (1961).

### 2.1.2 Geographic characteristics

The ionosphere can be divided into three latitudinal regions as described for instance by Jensen (2002). They are also illustrated in figure 2.3.

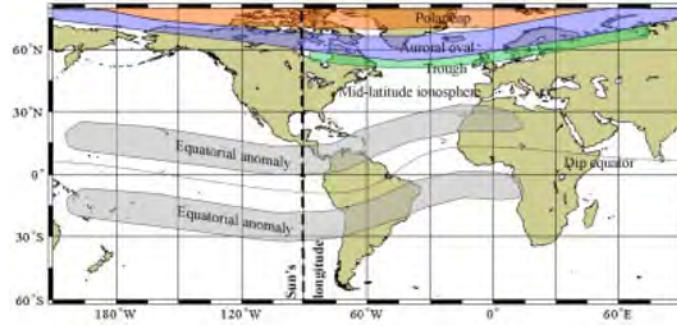


Figure 2.3: Major geographic regions of the ionosphere, Komjathy (1997b)

**The Equatorial region:** This region is located about  $30^\circ$  on each side of the geomagnetic equator. It is caused indirectly by the neutral wind, which pushes the ions and electrons upwards and in opposite north-south directions forming two electron density peaks at app.  $10^\circ$  at either side of the geomagnetic equator. When the ions and the electrons are pushed away from the geomagnetic equator these results in a lower electron density at the geomagnetic equator and therefore large gradients can be observed. Steep vertical walls, called bubbles, are present, which causes irregularities, which again can cause scintillation effects, see section 2.2.2 and 2.3.2.

**The mid latitude region:** This region spans from  $30^\circ$  geomagnetic latitude to the auroral oval at app.  $60^\circ$  to  $65^\circ$ . It is characterized by very few disturbances and thus the variation of total electron content (TEC) is well predicted. However on the border to the auroral oval large gradients in the north-south direction can be seen.

**The auroral and polar cap region:** This region spans from the mid-latitude region and up to the poles. The geomagnetic field lines are nearly vertical in this region which causes that the charged particles descend to E layer altitudes at app. 100 km. These particles can collide with the neutral atmospheric gases causing local enhancements in the electron content, which is associated with auroral activity. The auroral zones are relatively narrow

rings with an average width of approximately  $5-7^\circ$  and is situated at about  $65-70^\circ$ . Patches of geomagnetic field aligned electron density with a horizontal size of 50 - 1000 km. are present and concentrated in the F2 layer. Inside these patches, irregularities with size of app. 1 km. exist and these can cause scintillation. The ovals expand towards the equator with increasing levels of geomagnetic disturbances. On the equatorial side of the auroral oval lies the mid latitude trough which is a narrow region with a width of a few degrees. It can be characterised by a sudden drop in the electron densities which gives large gradients, and can cause scintillation effects, see section 2.3.2. The geographical regions enclosed by the auroral rings are called polar caps.

## **2.2 Observed variations of the ionosphere**

### **2.2.1 Time varying parameters**

The existence of the ionosphere is directly related to the emitted radiations from the sun, thus the movement of the Earth about the sun or changes in the sun's activity will result in variation in the ionosphere observed from ground. There exist 4 regular variations which can be predicted to a certain degree as they occur in cycles. These are:

- Daily
- Seasonal
- 11 year
- 27-day

The daily variations in the ionosphere are a direct result of the 24 hour rotation of the Earth around its axis. The variation can be considered as if the bow shock is considered constant and the Earth is rotating beneath. As such the cyclic is well described with little variation in the prediction. The D layer has little effect on very high frequencies and it disappears at night. In the E layer, ionization depends on the angle of the sun, but it is greatly reduced at night. The structure and density of the F layer depends on the time of day and the angle of the sun. The F layer consists of one

layer in the night, but splits into two layers in the daylight hours. The F2 layer is the most variable part having its height and density change with time of day, season, and sunspot activity. In general this results in daily variations in the mid latitude region described as an increase in the Total Electron Content (TEC) at sunrise with a peak approximately 14.00 local time. A slower decaying phase during the afternoon and a low almost constant activity during the night. TEC is defined in section 2.3.1.

The seasonal variations of the ionosphere are the result of the Earth revolving around the sun that is the relative position of the sun moves from one hemisphere to the other with changes in the seasons. Seasonal variations of the D, E, and F1 layers correspond to the highest angle of the sun, meaning that the ionization density of these layers is greatest in the summer period and lowest in the winter. The F2 layer follows the opposite pattern with ionization greatest in the winter times and lowest in the summer. The seasonal variation is also a result of the neutral composition. The production rate of electrons depends on number of atomic O, while the recombination rate depends on the number of  $N_2$ . If the  $N_2$  is colder it means less effective recombination of  $N_2$  with electrons, meaning a higher number of electrons. Thus TEC is dependent on the temperature. In general this results in TEC values which are highest in the winter period, near the equinoxes in February and October. Skone (2007).

The 11 year period is related to the appearance and disappearance of sunspots. These are dark irregular shaped areas on the surface of the sun. The exact reason for the sunspots is not known, but they are believed to be caused by violet eruptions on the sun and are characterized by unusual strong magnetic fields. The life span of each sunspot is variable and they can occur unexpectedly. However a regular cycle of sunspot activity with both a minimum and maximum

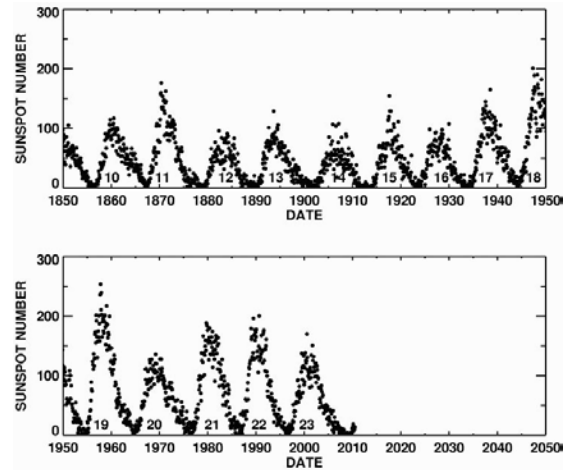


Figure 2.4: Monthly averaged sunspot numbers from 1850 to 2010, Hathaway (2010).

level occurring approximately every 11 years has been observed, see figure 2.4. The current solar cycle, number 24, has just started from a very low level in 2009. The sunspots themselves produce only minor effects in the solar emissions from the sun, but the associated magnetic variations produce variations in the ionization level of the ionosphere and the ionization density increase for all the ionospheric layers when the sunspot activity increases.

The 27-day variations are a result of the sun's approximate period for rotation around its axis. The number of sunspots in existence at any one time is continually subject to change as some disappear and new ones emerge. As the sun rotates, these sunspots are visible at 27-day intervals. The sunspots cause variations in the ionization density of the layers making precise predictions on a day-to-day basis difficult. The fluctuations in the F2 layer are greater than for any other layer.

### **2.2.2 Ionospheric bubbles**

The existence of ionospheric or plasma bubbles has been known and reported using several measurement techniques for over 30 years. This includes all-sky imagers, incoherent radar measurements, in situ measurements and GPS measurements. Many parameters are involved in describing the characteristics of this feature, as it is dependent on local solar time, location, season, solar cycle and magnetic activity and many aspects of the generation and evolution of the bubbles still remain to be clarified, which only makes the characterization more complex and difficult.

The total lifetime of a plasma bubble can be divided into two phases, the growth and the decay phase, as described by Tsunoda (1981). The definition of the start and stop conditions for these phases is not clearly defined in the literature, however different characteristics of the plasma bubble exist in these phases. The growth phase starts at approximately 1-2 hours after sunset local time. At or near the geomagnetic equator a new patch of depleted ionization is formed in the bottom side of the F2 layer. The patch grows larger in size and at the same time drifts or rises upwards into the peak of the F1 layer. It then starts to map poleward along the magnetic field lines until it reaches the Appleton anomaly (peaks at approximately  $\pm 15^\circ$  magnetic latitude) regions north

and south of the magnetic equator.

An example of a plume or patch is illustrated in figure 2.5. It shows a sequence of ALTAIR<sup>1</sup> maps to illustrate the generation and growth of a plume. Plumes, developing in the bottom side of the F-layer are associated with plasma bubbles. The plume head is growing larger in size and on the third map it has penetrated into the topside of the F-layer. It continues to grow (not shown on the figure) and app. 0927 UT it reached a peak altitude of 625 km. The slowdown of the vertical velocity marks the end of the growth phase and the beginning of the decay phase. In this example, the total duration of the growth phase was app. 50 min.

The decaying phase is characterized by the movement of the patch. The fully developed patch is moving in the east-ward direction and the velocity is slowly decaying. The small scale irregularities are at the same time also slowly vanishing. The duration of this phase can last several hours depending on the solar activity and usually last until 1 hour after local midnight. The end time of the decay phase is depending on the start time of the growth phase.

### 2.2.2.1 Rayleigh Taylor instability

Plasma bubbles and the irregularity production mechanism are widely believed to be generated by the growth of electron density fluctuations by the generalized Rayleigh Taylor instability as studied by Tsunoda (1985). Typically, the generation of the bubbles is confined to the equatorials regions. This is because of at the geomagnetic equator is the geomagnetic field,  $B$ , not perpendicular to gravity, and the plasma can fall along the field lines rather than remain in the dynamically unstable situation. In Tsunoda (1985) it is shown that a favourable condition for the Rayleigh Taylor instability is the alignment of the geomagnetic flux tubes and the sunset terminator. This happens when the conjugate E-regions enter into darkness at the same time, and thereby creates a large gradient in the E-region Pedersen conductivity. This large longitudinal conductivity gradient can enhance the eastward electric field, which can destabilize to the Rayleigh Taylor instability. This leads to

---

<sup>1</sup>A fully steerable backscatter radar located on Roi-Namur Island in the Kwalein Atoll, Marshall Islands

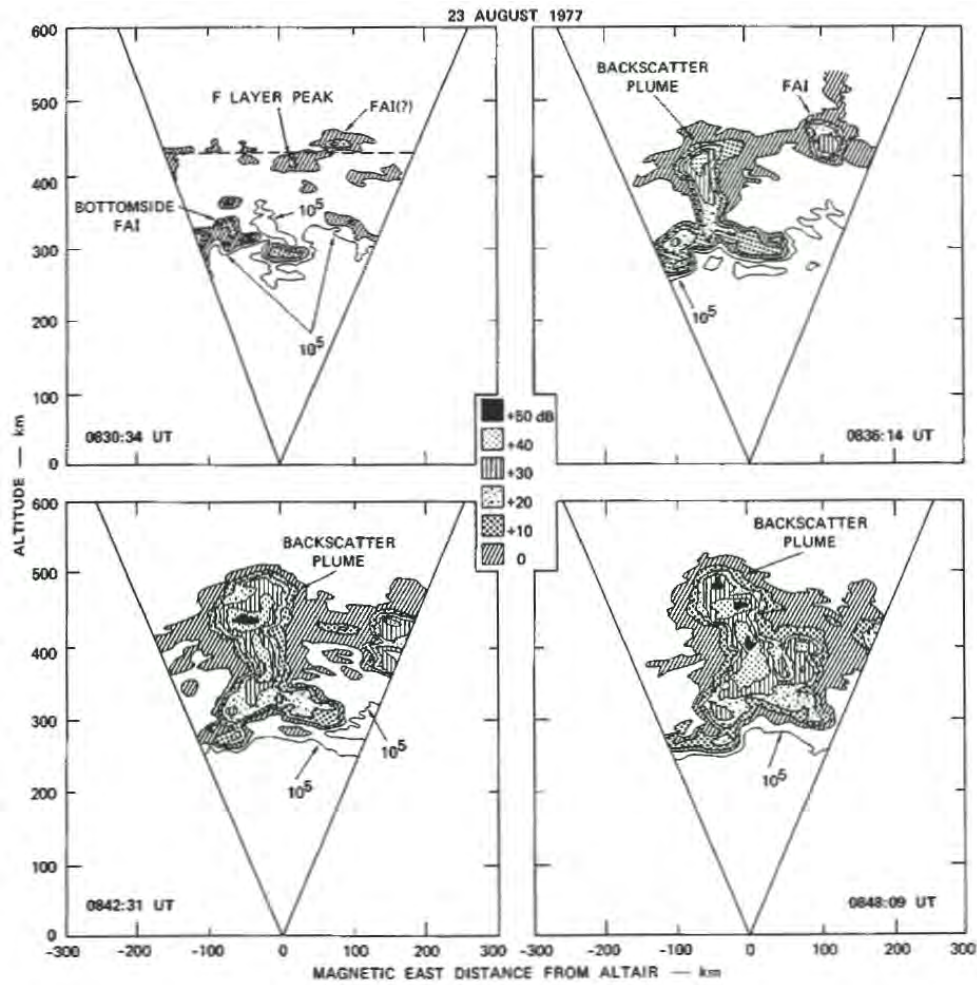


Figure 2.5: Example of a plume generation, taken from Tsunoda (1981)

the definition of sunset time lag, which is the difference between the sunset times of two conjugate geomagnetic points and represent the geometry of the geomagnetic field line and the sunset terminator line. This means that when the sunset time lag is low (the sunsets of the geomagnetic conjugate points are synchronized), there is a larger probability of plasma bubble occurrence. Due to the variability of the geomagnetic equator and its declination towards the geographic equator, the above mentioned assumption leads to a division into 5 longitudinal sectors, with different plasma bubble occurrence statistics as discussed in section 2.2.2.2.

It is also in general believed that gravity waves in the neutral atmosphere

can play a role as a seeding mechanism of ionospheric irregularities. Huang and Kelley (1996a) and Huang and Kelley (1996b) modelled the physical processes whereby the gravity waves seeded the initial perturbations in the bottom side night time ionosphere and their subsequent evolution through the Rayleigh Taylor instability.

The growth of the Rayleigh Taylor instability,  $\lambda$ , is controlled by many parameters as described in the generalized formula in equation 2.1 by Zalesak et al (1982).

$$\lambda = \frac{\sum_F^P}{\sum_F^P + \sum_E^E} \left( V_P + U_n^P + \frac{g}{\nu_{in}} \right) \cdot \frac{1}{L} - R \quad (2.1)$$

where  $\sum_F^P$  and  $\sum_E^E$  are the flux tube integrated conductivities in the E- and F-region

$V_P$  is the vertical upward component of plasma drift by  $E \times B/B^2$  drift due to the eastward electric field

$E$  is the electric field

$B$  is the geomagnetic field

$U_n^P$  is the vertical downward component of the neutral wind velocity

$g$  is the gravity acceleration

$\nu_{in}$  is the ion neutral collision frequency

$L$  is the scale length of the vertical gradient of the flux-tube integrated plasma density in the F-region on the magnetic equator, and

$R$  is the recombination rate, that is integrated along the flux tube.

The conductivity in the F-region is higher than in the E-region after sunset. Under this condition, the F-region dynamo due to the eastward neutral wind controls the electro dynamics of the ionosphere. As a result, the eastward electric field enhances around the sunset terminator and an enhanced electric field makes the  $E \times B$  speed large. The enhancement of the electric field also makes the collision frequency and the recombination rate small, which in the end makes the growth rate large. This means that the Rayleigh Taylor instability has favourable conditions soon after sunset.



### 2.2.2.2 Occurrence statistics

Many studies on the occurrence characteristics of plasma bubbles has been performed using a variety of observational data such as ionosonde, topside sounders, radio scintillations, GPS and in situ measurements. The in situ observations have an advantage of covering all longitudes, but they are largely affected by satellite orbit and altitude. The GPS receivers have a limitation in the location, but have an advantage because the numbers of receivers is large.

A study for occurrence rates in the equatorial region has been made by Nishioka et al (2008) using GPS receivers. 5 regions, shown in figure 2.6, are defined according to their geographic longitude and the geomagnetic declination angle, the angle between the geomagnetic equator and the Earth's equator. It can be seen that the declination angle is largest in the Eastern and Atlantic region, while it is almost constant in the African, Asian and Central Pacific regions.

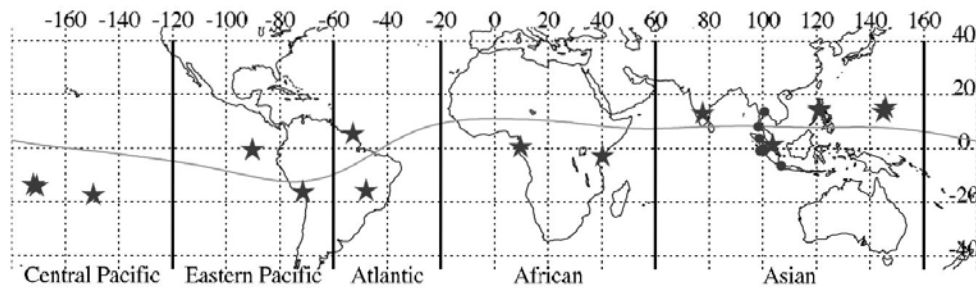


Figure 2.6: 5 sectors divided by their geographic longitude indicated by the vertical thick lines. The geomagnetic dip equator is illustrated by the curved line. The stars show the location of GPS stations used in the study of bubble occurrence shown in figure 2.7, Nishioka et al (2008).

In figure 2.7 is a summary for the 5 different regions displayed taken from Nishioka et al (2008). It has been reported by Tsunoda (1985), that the occurrence rate is affected by the geomagnetic declination angle and it controls the seasonal dependence for the longitudinal region. In general it is expected that the occurrence rate of plasma bubbles is expected to be high during periods where the sunset time lag is low. The sunset time lag is shown in the bottom of figure 2.7 and represents the geometry of the geomagnetic field

line and the sunset terminator line. It will be low when the geomagnetic conjugate points are synchronized. Even though the occurrence rates follow this trend, discrepancies do exist. There is an asymmetry in the occurrence between two solstices. For instance in the Asian region from 2000-2003 and the African region from 2000-2006, the occurrence rate of plasma bubbles are larger in the June solstice than the December solstice. Also asymmetry in the occurrence rate between two equinoxes is seen. For instance in the Asian sector from 2005-2006 is the March equinox larger than the September equinox. In contrast for the Pacific region the September equinox is larger than the March equinox.

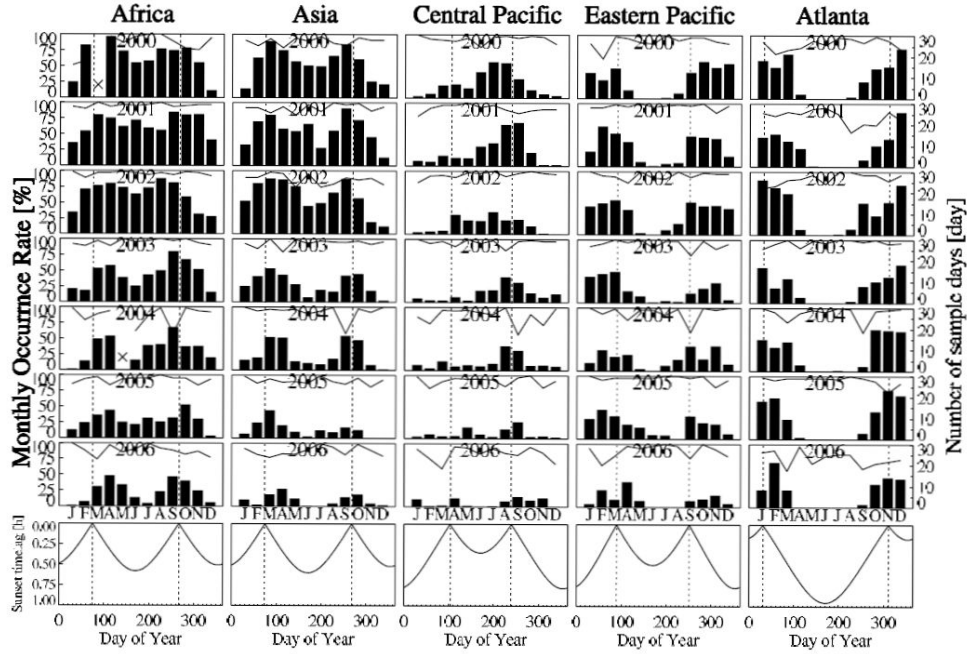


Figure 2.7: Monthly occurrence rates of plasma bubbles from 2000 - 2006. The histograms show the occurrence rate for five different longitudinal sectors. On the right hand side is the scale for the average number of sample days. In the bottom plot is sunset time lag between the geomagnetic conjugate points displayed Nishioka et al (2008).

Though the different occurrence rates show clear seasonal dependence, plasma bubbles can also be triggered or intensified during any season during magnetic storm events.

### 2.2.3 TID

Travelling Ionospheric Disturbances (TID) are short-term periodic (hours) variations in the TEC, covering a large range of periods and amplitudes. They are associated with midlatitude atmospheric gravity waves. This is the effect from motion of air that is being pushed up or down and restored again by gravity. According to Skone (2007) can the gravity waves:

- Propagate down from the auroral regions, which are associated with geomagnetic disturbances
- Propagate upwards from the lower atmosphere, which are associated with atmospheric tides, troposphere weather etc.
- Generated by electrodynamic forces in the ionosphere that generate instabilities

The TIDs are classified into three classes according to table 2.1.

TID	Wavelength [km.]	Horizontal phase velocity [m/s]	Period [minutes]
Small Scaled (SSTID)	< 100	< 100	< 12
Medium Scaled (MSTID)	100 - 1000	100 - 300	12 - 60
Large Scaled (LSTID)	> 1.000	100 - 300	30 - 180

Table 2.1: Three classes of TIDs, Memarzadeh (2009).

The MSTID are observed frequently in the mid-latitudes and most of them have amplitudes of less than 1 TECU, but occasionally MSTIDs with amplitudes of 10 TECU are observed, see section 2.3.1 for a definition of TECU. Amplitudes associated with LSTIDs are frequently observed as greater than 5-10 TECU during major magnetic storms. LSTIDs move predominantly equator wards, but the movements of MSTIDs and SSTIDs are more complex.

Since 1 TECU correspond to app. 16 cm. on the L1 carrier, see table 2.2 in section 2.3.1, the TIDs will have a large change in the range delay when the TID is passing through the observed region. Furthermore can the gradients of the TIDs have an impact in single station and network RTK applications, when the distance to nearest reference station increase.

## 2.3 Effect on satellite navigation signals

### 2.3.1 General first order effects

When the satellite signals are travelling through the ionosphere they are affected by the particles and this cause refraction, a change in speed and direction. The refractive index is the relation between the speed of light in vacuum and the speed of the signal in the medium. The refractive index changes in the ionosphere as the composition of the medium changes and the changing cause a signal bending making the signal path longer compared to the geometrical distance. For planar high frequency electromagnetic waves, the refractive relations are described by the Appleton-Hartree formulation. This express the wave field dependence of the characteristic frequencies of the medium. The refractive index is expressed as in equation 2.2, Budden (1985).

$$n^2 = 1 - \frac{X(U - X)}{U(U - X) - \frac{1}{2}Y^2 \sin^2 \xi \pm \sqrt{\frac{1}{4}Y^4 \sin^4 \xi + Y^2 \cos^2 \xi (U - X)^2}} \quad (2.2)$$

where  $X$ ,  $Y$  and  $U$  are dimensionless quantities, relating the wave frequency with the plasma frequency, gyro frequency and collision frequency.  $\xi$  defines the angle between the direction of the constant ambient magnetic field and the wave number vector.

Neglecting the higher order terms the phase refraction index can though be approximated to a first order given in equation 2.3, see for instance Hartmann and Leitinger (1984).

$$n_p = \sqrt{1 - \frac{f_P^2}{f^2}} = \sqrt{1 - \frac{80.6N_e}{f^2}} \quad (2.3)$$

where  $f_P$  is the plasma frequency given by  $\sqrt{\frac{e^2}{4\pi^2 m \epsilon_0} N_e} = \sqrt{AN_e}$

$e$  is the electron charge

$m$  is the electron mass

$\epsilon_0$  is the permittivity of free space

$$A = 80.6m^3s^{-2}$$

$N_e$  is the electron density

$f$  is the frequency of the signal

and in a further step of approximation can the square root be expanded to give

$$n_p = 1 - \frac{1}{2} \frac{80.6N_e}{f^2} = 1 - \frac{40.3N_e}{f^2} \quad (2.4)$$

The total electron content, TEC, is defined as the number of electrons in a tube of  $1m^2$  cross section extending from the receiver  $u$  to the satellite  $s$ , as expressed in equation 2.5, Misra and Enge (2006).

$$TEC = \int_u^s N_e(l)dl \quad (2.5)$$

where  $N_e(l)$  is the varying electron density along the signal path.  $TEC$  is measured in  $TEC$  units (TECU). 1 TECU equals  $10^{16}$  electrons/ $m^2$ .

The signal delay caused by the ionosphere,  $d_{ion}$  [m], is given by the actual signal path subtracted the geometrical by the geometrical distance between the receiver and the satellite, as written in equation 2.6

$$d_{ion} = \int_u^s n_p ds - \int_u^s ds = \int_u^s (n_p - 1) ds \quad (2.6)$$

as the refractive index along the geometric distance is constant 1 as the speed equals the speed of light.

By combining equations 2.4, 2.5, and 2.6 can the signal delay as a function of the TEC to a first order be described as in equation 2.7.

$$d_{ion} = -\frac{40.3}{f^2} \int_u^s N_e ds = -\frac{40.3}{f^2} TEC \quad (2.7)$$

Signal	C-band	L1/E1	E6	L2	E5b	L5/E5a
<b>Frequency</b>						
[MHz]	5015.00	1575.42	1278.75	1227.60	1207.14	1176.45
<b>Wavelength</b>						
[m]	0.0598	0.1903	0.2344	0.2442	0.2483	0.2548
1 m. range error [TECU]	62.41	6.16	4.06	3.74	3.62	3.43
1 ns delay [TECU]	18.71	1.85	1.22	1.12	1.08	1.03
1 TECU range delay [m]	0.016	0.162	0.246	0.267	0.277	0.291
1 TECU time delay [ns]	0.0534	0.5416	0.8221	0.8920	0.9225	0.9713

Table 2.2: First order time and range delay for a selected group of GNSS signals and a possible future signal in the C-band.

This implies that the signal delay is proportional to the inverse of the squared frequency and can thus be calculated when two frequencies are used, and the higher the frequency the less is the signal affected. In table 2.2 is summarised time and distance delay for a number of GPS and Galileo signals. It can be seen that if a signal on the L1/E1 frequency travels through 1 TECU, this corresponds to a distance delay of approximately 16 cm. In the table is also listed a signal in the C-band spectrum, to illustrate the effects for a possible future signal, and the effect at this frequency is almost ten times smaller than a signal on the L1/E1 frequency.

The delay in equation 2.7 is negative, which means that it corresponds to a phase advance. The group delay has the same size, but with opposite sign. The reason for this is that a GNSS signal can be considered a superposition of a group of waves of different frequencies, and since the index of refraction is a function of frequency, the modulation of the signal will experience another refraction than the pure signal.

The size of the delay is smallest in the zenith direction as the distance through the media is shorter at high elevation angles. A trend of this, given by Klobuchar (1996), is that the effect is increased by a factor of three for a signal at an elevation angle of  $10^\circ$  compared to a zenith delay. A relation between the TEC at zenith angle, called the Vertical TEC (*VTEC*) and the TEC along the signal path, called the slant TEC (*STEC*), are normally expressed using a mapping function. A frequently used model is called the single layer model, see figure 2.8. In the single layer model is the ionosphere represented by a thin spherical layer at a given height,  $h_{ion}$ , (in the range of 300-400 km.). The point of intersection between the signal and the shell is referred to as the Ionospheric Pierce Point (IPP) and the angle between the signal path and a line from the center of the Earth to the IPP is referred to as the zenith angle,  $\alpha$ . The relation between the VTEC, STEC, and the elevation angle  $E$  can then be expressed as in equations 2.8 and 2.9, see for instance Seeber (2003).

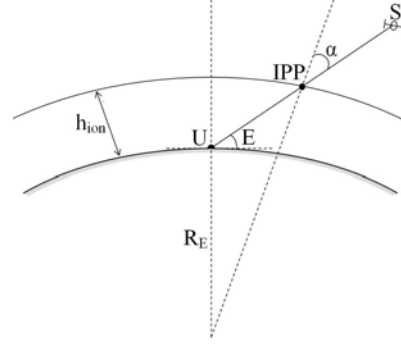


Figure 2.8: Illustration of the single layer model of the ionosphere, redrawn from Seeber (2003).

$$VTEC = \cos \alpha STEC \quad (2.8)$$

where

$$\alpha = \arcsin \left( \frac{R_E}{R_E + h_{ion}} \cos E \right) \quad (2.9)$$

### 2.3.2 Scintillation effects

The basic principle for the scintillation phenomena is visualized in figure 2.9. The propagated wave front with constant signal phase travels through ionospheric irregularities consisting of unstable plasma or small scale of electron density gradients.

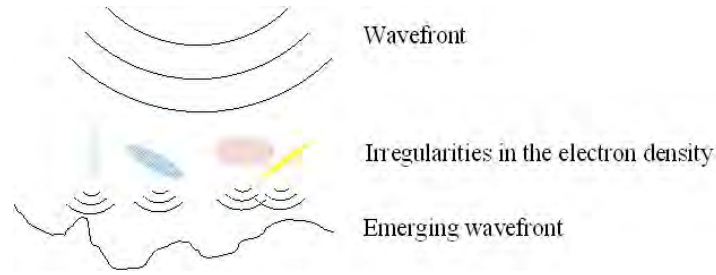


Figure 2.9: Illustration of the scintillation phenomena.

As long as the irregularities and the locations of the transmitter do not change, a single receiver at a fixed location would detect a constant amplitude and phase. But this is theory, and in reality phase shifts occur at the irregularities creating an irregular emerging wave front, that essentially is causing the wave to interfere with itself. The result is observed phase and amplitude variations on the ground. Either a signal fading or a signal enhancement and in both cases the signal strength can jump out of the threshold of the receivers tracking loop bandwidth causing cycle slips.

In figure 2.10 is the morphology for global amplitude scintillations illustrated. This outlines two regions with high probability of intense scintillations. The equatorial region at approximately 20 degrees on each side of the magnetic equator and the north region between 55 and 90 degrees. The effects in the equatorial region are associated with ionospheric bubbles, described in section 2.2.2.

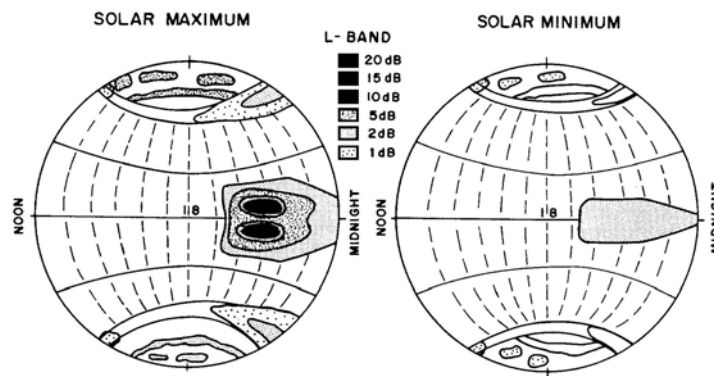


Figure 2.10: Global variation of amplitude fading in scintillations during solar maximum and minimum conditions, Basu et al (1988)



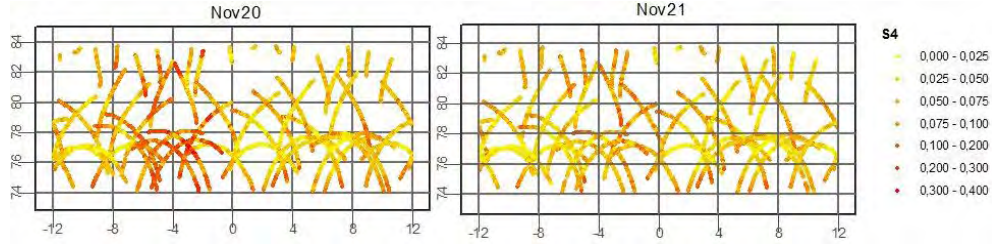


Figure 2.11: Example of  $S_4$  as function of latitude [ $^\circ$ ] of the ionospheric pierce point and local solar time [hour] for Ny Alesund at  $78.9^\circ$  latitude November 20th and 21st 2003.

The usual measure of strength of amplitude scintillation is the  $S_4$  index, which is described as the root mean square of the variance of the received power divided by the average value, see equation 2.10.

$$S_4 = \sqrt{\frac{\langle I^2 \rangle - \langle I \rangle^2}{\langle I \rangle^2}} \quad (2.10)$$

where  $I$  is the signal intensity. Averages, indicated by the bracket parentheses, are in general over 60 seconds.

An example of  $S_4$  is illustrated in figure 2.11 and the corresponding probability density functions are illustrated in figure 2.12. The data is from a high latitude station in Ny Alesund at  $78.9^\circ$  latitude and  $11.9^\circ$  longitude from November 20th and 21st in 2003, where a major ionospheric storm took place November 20th. The data is collected from a GPS Ionospheric and TEC monitor and is part of the ISACCO (Ionospheric Scintillation Arctic Coordinated Observation) project by INGV.

The estimated  $S_4$  is based on an average over 60 seconds of 50 Hz sampled data. Because of high values of the scintillation parameters for low elevation satellites, the observations have been filtered with an elevation mask of 30 degrees, which gives a better estimate of the statistical parameters. The  $S_4$  is illustrated as a function of latitude of the ionospheric pierce point and local solar time for all observed satellite tracks. In general are the values higher for low elevation satellites, though satellite tracks with variation in the values do exist. The large value around -4 hours solar time for November 20th is caused by the ionospheric storm. The probability density functions are not normal

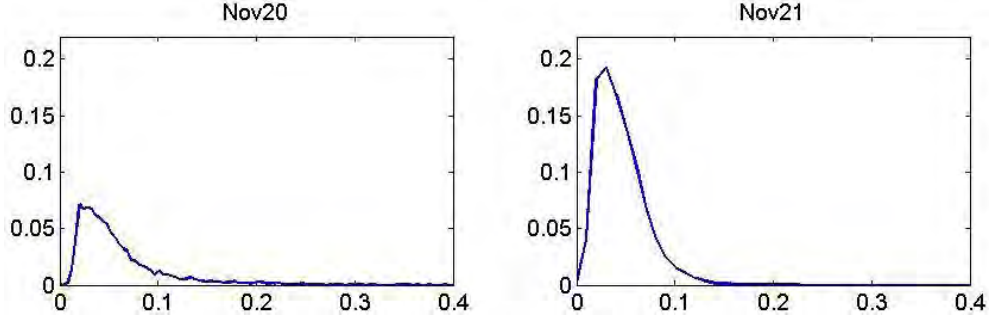


Figure 2.12: Probability density functions for  $S_4$  for Ny Alesund November 20th and 21st 2003.

distributed, but has the same shape. The 20th of November has significant higher values than November 21st.

### 2.3.2.1 Mean time between cycle slips

The effect of loosing lock to a satellite for a short period of time can have severe positioning effects in many applications, which is dependent on constant tracking of the satellite. An example is Real Time Kinematic applications, where the whole number of wavelength or ambiguity shall be recalculated after a loss of lock or cycle slip. An analysis of the expected time between cycle slips on the carrier loop inside the receiver is therefore important and will be addressed in the following with focus on the presence of scintillation. The tracking error variance,  $\sigma_{\Phi, \epsilon}$ , at the output of a single Phase Lock Loop, PLL, in the presence of scintillation, can be expressed as in equation 2.11, see for instance Conker et al (2000) and Knight and Finn (1998). It is assumed that there is no correlation between phase and amplitude scintillation and other error sources, such as multipath is neglected.

$$\sigma_{\Phi, \epsilon}^2 = \sigma_{\Phi, S}^2 + \sigma_{\Phi, T}^2 + \sigma_{\Phi, osc}^2 \quad (2.11)$$

where  $\sigma_{\Phi, S}^2$  is the phase scintillation variance, equal to zero in case of no scintillation.

$\sigma_{\Phi, T}^2$  is the thermal noise.

$\sigma_{\Phi, osc}^2$  is the receiver/satellite oscillator noise assumed to be equal to 5.7 deg,

Hegarty (1997).

In the case of no scintillation will the thermal noise and oscillator noise tracking error constitute a lower bound, since  $\sigma_{\Phi,S}$  will be zero. Thermal noise tracking error can be expressed as in equation 2.12 in case of presence of scintillation. For a derivation the reader is referred to Conker et al (2000). This equation is valid for weak scintillations, meaning  $S_4$  values below 0.707.

$$\sigma_T^2 = \frac{B_n \left[ 1 + \frac{1}{2\nu(c/n_0)_{L1-C/A}(1-2S_4^2(L1))} \right]}{(c/n_0)_{L1-C/A} (1 - S_4^2(L1))} \quad (2.12)$$

where  $B_n$  = L1 3rd order PLL one-sided bandwidth = 10 Hz.

$(c/n_0)_{L1-C/A}$  is the fractional form of signal-to-noise density ratio =  $10^{0.1C/N_0}$ .

$\nu$  is the predetection integration time, which is 0.02s for GPS.

In case of no scintillation will the thermal noise tracking error becomes the standard thermal noise tracking error for the PLL, which is given in for instance Kaplan and Hegarty (2006).

The phase scintillation variance of the carrier phase tracking is, under conditions of phase scintillations, assumed to be zero-mean. It is expressed as in equation 2.13, see for instance Conker et al (2000) for a derivation, and is legitimate as long as  $2k - 1 > 0$  and  $p > 1$ .

$$\sigma_{\Phi,S}^2 \cong \frac{\pi T}{k f_n^{p-1} \sin \left( \frac{[2k+1-p]\pi}{2k} \right)}, \text{ for } 1 < p < 2k \quad (2.13)$$

where  $T$  is the spectral length at 1 Hz

$k$  is the loop order

$p$  is the slope of the Power Spectral Density (PSD) of phase scintillation, usually in the range of 1-4.

Equation 2.11 can then be combined with equations 2.12 and 2.13 and evaluated for selected values of  $\sigma_{\Phi,\epsilon}$  to give the mean time to loose lock as done by Conker et al (2003) and shown in table 2.3.

$\sigma_{\Phi,\epsilon}$ [degrees]	t (1st order PLL) [hour]	t (3rd order PLL) [hour]
9	14149.57	141.50
10	303.02	3.03
11	17.68	0.18
12	2.04	0.02

Table 2.3: Mean time to loose lock for selected RMS tracking error variance values, Conker et al (2003)

It can be seen that higher order loops, which is used for dynamic platforms, have values of the mean time to loose lock significant smaller than lower order loops. In this case two orders of magnitude between a first and a third order loop. The table illustrates, that with a threshold of  $10^\circ$  and with a third order PLL loop, the receiver will loose lock due to carrier phase error on the L1 once every 3 hours. It shall be noted that this analyses is based on  $S_4$  values below 0.707, which is related to weak scintillation theory.

## 2.4 Models of the Total Electron Content

In order to represent the total electron density at different geographic places, solar activity and time of day a number of models have been developed. Three of these will be described in the following sections.

### 2.4.1 Klobuchar

The Klobuchar model is the GPS broadcast ionosphere model and is named after its inventor, see Klobuchar (1987). Basically it is a functional model based on 8 parameters transmitted via the navigation message to the GPS user. The input parameters is the geomagnetic coordinates of the ionospheric pierce point, the time of day and the 8 coefficients transmitted in the navigation message. Based on this the model outputs the ionospheric delay  $I_{Z,L1}$

in units of m. on the L1 carrier using equation 2.14

$$\frac{I_{Z,L1}}{c} = \begin{cases} A_1 + A_2 \left( \frac{2\pi(t-A_3)}{A_4} \right), & \text{if } |t - A_3| < A_4/4 \\ A_1 & \text{otherwise} \end{cases} \quad (2.14)$$

where  $c$  is the speed of light in vacuum

$t$  is the local time of the ionospheric pierce point

$A_1$ : Constant night time value ( $5 \cdot 10^{-9}s$ )

$A_2$ : Amplitude of the cosine function for daytime values

$A_3$ : Phase corresponding to the peak of the cosine function (fixed at 14 h local time)

$A_4$ : Period of the cosine function ( $\geq 72000s$ )

$A_2$  and  $A_4$  can each be determined by a polynomial of four of the coefficients and by the ionospheric pierce point as well as coordinates for the magnetic pole. The eight coefficients, broadcasted in the navigation message, are selected by the Master Control Station and are associated with the different seasons and levels of solar activity. It is possible to update the coefficients on a daily basis, but normally they are updated every six days. An example can be seen in figure 2.13

Many assumptions were made in the development of the model because of the limiting factor of only 8 parameters that could be used. One of the assumptions is that the daily peak of the ionospheric delay occur at 14.00 h local time at all places, at all latitudes, at all seasons and at all kind of solar activity. Other assumptions include the constant delay during the night and that the diurnal variation follows a smooth half cosine with no specific auroral/equator and yearly variations. It is estimated, that the klobuchar model can reduce the rms range error measurements due to uncompensated ionospheric delay by about 50%, Klobuchar (1996).

### 2.4.2 NeQuick

NeQuick is a three dimensional and time dependent quick-run electron density model developed at the Aeronomy and Radio Propagation Laboratory of the Abdus Salam International Center for Theoretical Physic (ICTP), Trieste, Italy, and the Institute for Geophysics, Astrophysics and Meteorology

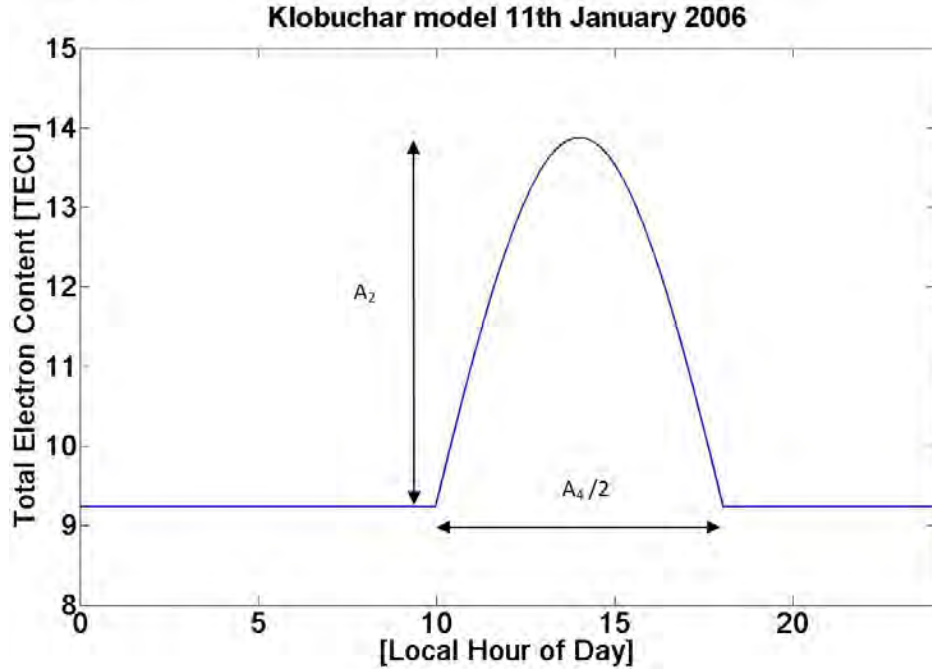


Figure 2.13: Example of the daily variation of TECU using the Klobuchar model

of the University of Graz, Austria. The first version of the model has been adopted by the European Space Agency (ESA) for single frequency positioning applications in the framework of the European Galileo project, see Nava et al (2006). The model has since been modified and updated several times with a version 2 published in 2008, see Nava et al (2008). The most important modifications are related to the bottom side formulation in terms of the modelling of the F1 layer peak electron density, height and thickness parameter.

The NeQuick model gives the electron density as a function of solar activity, month, universal time, altitude, and geographic location. It also allows easy calculation of the total electron content along a given ground station-to-satellite ray path. The model fit analytical functions on three anchor point, the peaks of the E-layer, the F1-layer, and the F2 layer, in order to represent these principal ionospheric layers and compute the electron density profile.

The model gives the large wavelength of the ionosphere, thus small scale variations, like for instance TIDs, are not present. This regards both the time and the geographic resolution. An example of a vertical TEC map produced

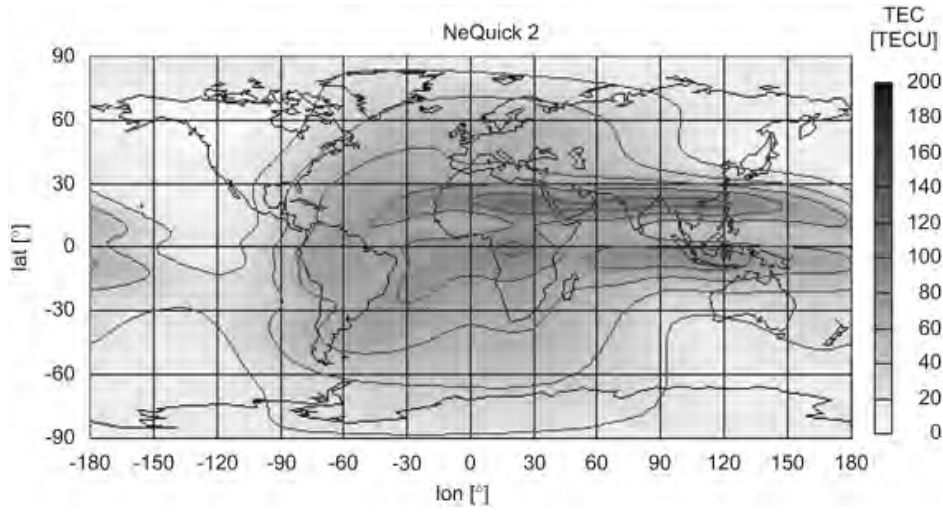


Figure 2.14: Example of a vertical TEC map using NeQuick 2. The month is October and  $F_{10.7} = 190$  and UT is 13.00, Nava et al (2008)

by the NeQuick 2 model can be seen in figure 2.14.

A recent study, see Bidaine and Warnant (2010) have assessed the NeQuick 2 model at mid-latitudes. The difference between GPS-derived vertical TEC and the corresponding values from NeQuick 2 has been investigated on a high solar activity level, year 2002. Residual errors of less than 20% in standard deviation were found.

### 2.4.3 GIM

The Center for Orbit Determination in Europe (CODE) produces Global Ionospheric Maps (GIM) based on GNSS observations from about 200 GPS / GLONASS sites. The basic assumption is, that the entire vertical ionospheric layer can be compressed into a thin single layer. This means that all free electrons are distributed in a spherical shell of infinitesimal thickness representing the vertical TEC. The height above the Earth mean surface of the single layer corresponds to the peak of the electron density. The vertical Total Electron Content is modelled in a solar-geomagnetic reference frame using a spherical harmonics expansion up to degree and order 15, see equation 2.15. The differential code biases are estimated as constant values each day for all GPS satellites and ground stations, see Schaer et al (1996) and

Schaer et al (1995) for an explanation of the procedure used by CODE.

$$VTEC(\beta, s) = \sum_{n=0}^{n_{max}} \sum_{m=0}^n \tilde{P}_{nm}(\sin \beta) (a_{nm} \cos ms + b_{nm} \sin ms) \quad (2.15)$$

where  $VTEC$  is the vertical TEC value

$\beta$  is the geocentric latitude of the pierce point of the ionosphere

$s$  is the sun-fixed longitude of the ionospheric pierce point. It is also the difference between the Earth-fixed longitude of the pierce point and the longitude of the sun

$n_{max}$  is the maximum degree of the spherical harmonics expansion

$\tilde{P} = \Lambda_{nm} P_{nm}$  are the normalized associated Legendre functions of degree  $n$  and order  $m$  based on the normalization factor  $\Lambda_{nm}$  and the classical Legendre functions  $P_{nm}$

$a_{nm}$  and  $b_{nm}$  are the coefficients of the spherical harmonics.

In order to use the model the coefficients  $a_{nm}$  and  $b_{nm}$  must be known and these values can be extracted from Global Ionospheric Maps (GIM). A user can then obtain the vertical TEC by inputting any location and interpolate from the surrounding grid points in the shell. The time spacing between each map is 2 hours and interpolation between maps is required in order to provide vertical TEC at any given instance of time. An example of a GIM for Day of Year 181 in 2010 at 14.00 Universal time, UT, can be seen in figure 2.15. CODE is not the only one producing GIMs. The International GNSS Service (IGS), Jet Propulsion Laboratory (JPL), and the European Space Agency (ESA) among others also produce GIMs.

The temporal, the horizontal, and the vertical resolution are suitable for a general global perspective of the electron density, but for analyzing regional or local electron density variations better resolution is required.

## 2.5 Generation of local vertical TEC time series

A local time series of vertical TEC with a sampling rate of 30 sec. have been computed for the period of 1999 - 2009. Dual frequency GPS observations



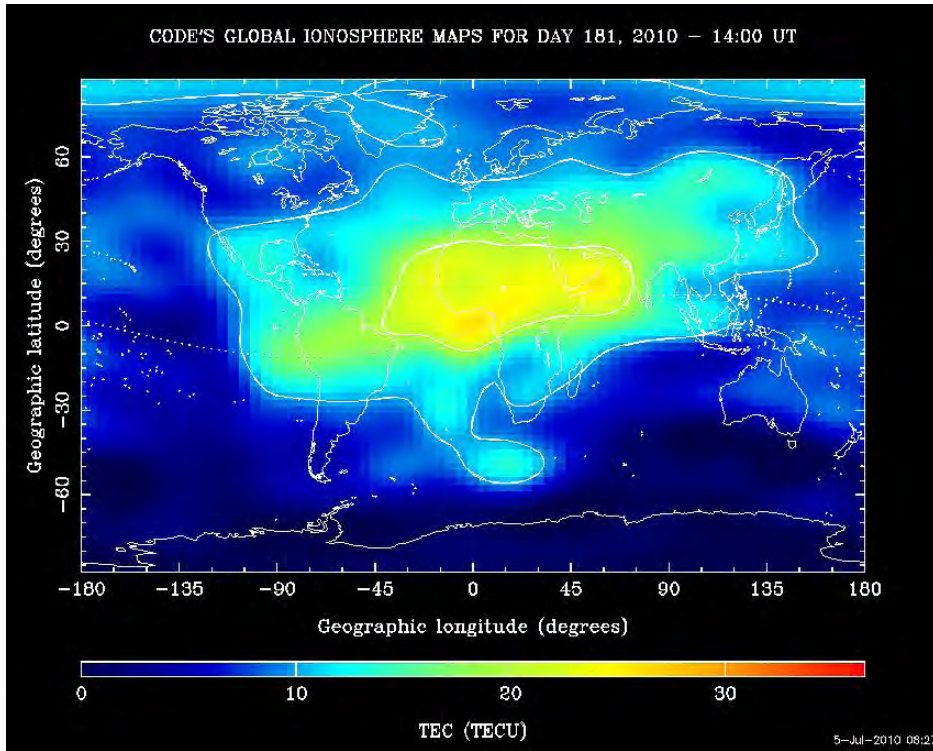


Figure 2.15: Example of a global ionospheric map

from three reference stations with a station separation of approximately 132 - 208 km. situated in Denmark have been used. In order to represent the ionospheric medium above the receivers is three station chosen. The time series have been derived using a Kalman Filter using the geometry-free L4 observation. This observation is the difference between the L1 and L2 carrier observations and consists mainly of the delay caused by the ionosphere. Three parameters are estimated, TEC, and the variations of TEC in the latitudinal and longitudinal direction, but only the TEC has been used in the data analysis. The detailed implemented procedure can be found in Jakobsen et al (2010) together with an explanation of the variables and the complete computed time series can be downloaded from <http://www.heisesgade.dk>.

An example of the computed vertical TEC time series for three summer days and three winter days for three selected years can be seen in figure 2.16. The selected years correspond to years with high, medium and low solar activity respectively. It can be seen that especially for the winter days a very clearly

daily signal is present for all the three selected years, the rise in the morning is a bit steeper than the fade in the afternoon. The summer days do not show the same night and day characteristics, but tends to be smoother over the day. The dependence of the solar cycle is clearly present as the level of the winter and summer days are separated for each year.

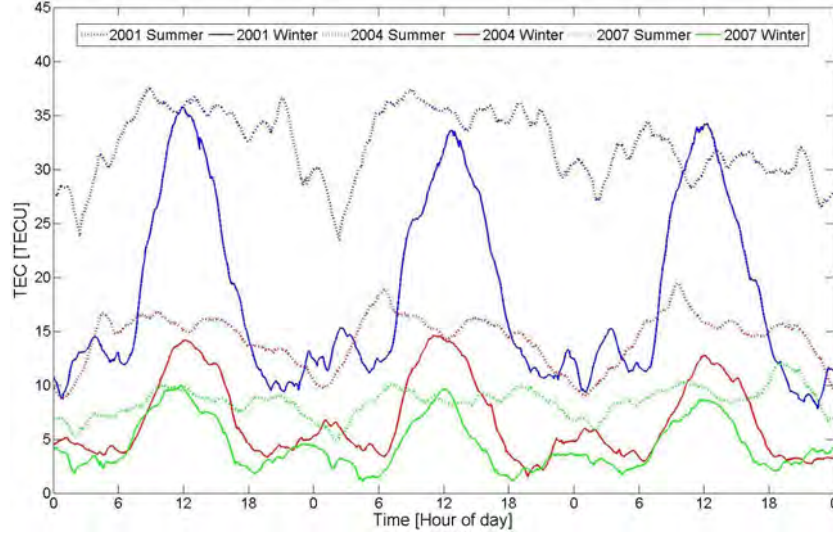


Figure 2.16: Example of the computed vertical TEC time series in UTC time for three summer days (Day of year 173-175) and three winter days (Day of year 11-13) in 2001, 2004, and 2007

The procedure for processing the time series of vertical TEC has been verified by comparing it to the final global ionospheric maps produced by the International GNSS service, see section 2.4.3. The momentary value from the vertical TEC time series are compared with a vertical TEC from each 2 hour map at the position of the considered center point for all of 2003. A linear interpolation between the four closest grid points and to the center point has been used.

A histogram of the residuals is illustrated in figure 2.17. It can be observed that they are normal distributed with an offset of 1.8 TECU and a standard deviation of 1.9 TECU. The correlation coefficient between the two time series is 0.96, which indicates good correlation between the model and the empirical data. Larger values than presented on the figure do exist, but they are associated with data gaps in the GNSS data. The values are higher during the reinitialisation of the kalman filter. There is no clear indication that they

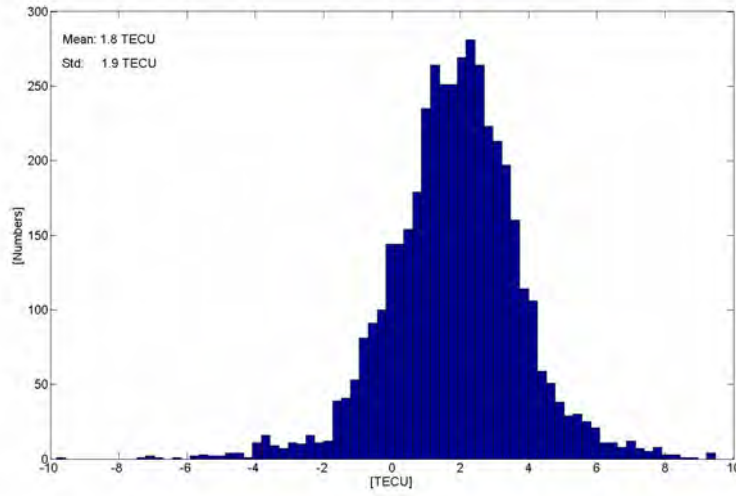


Figure 2.17: Histogram of residual data

are associated with geomagnetic storms.

The IGS maps are global and the long wavelength of the ionosphere is weighted higher, so an offset from a local momentary calculated value must be expected. This verification of the calculated time series is considered satisfactory in order to identify the local time varying characteristics of the ionosphere in the calculated time series.

## 2.6 Identify local time varying characteristics

### 2.6.1 Strength of the TEC signal

A Fourier analysis of the entire time series from 1999 - 2009 with spectral characteristics is shown in figure 2.18. There is a very strong daily signal with an amplitude of 6.6 TECU. This is a little lower than 7.4 TECU which was found in Jakobsen et al (2008). This analysis did not include the years 2008-09, and the last two years must therefore have a lower daily cycle. A yearly and a half yearly signal is also seen with amplitudes of 2.495 and 1.296 TECU, so these frequencies do not have the same power as the daily signal. In the side lobes of the daily signal a yearly modulation of the daily cycle is present.

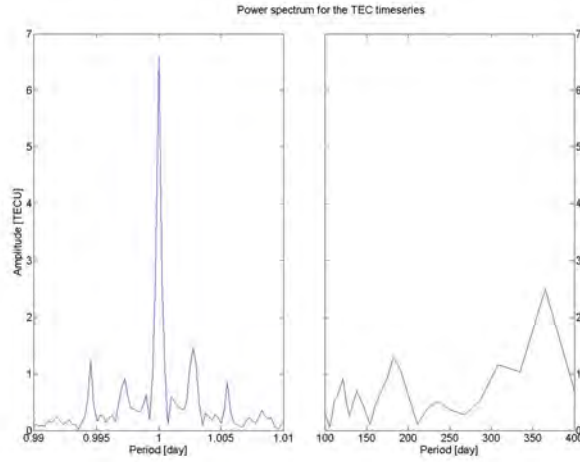


Figure 2.18: Power spectrum for the TEC time series from 1999 - 2009

Another way of showing the strength of the daily signal for the complete time series is illustrated in figure 2.19. Each graph represents one year and each value corresponds to the standard deviation of the time series of half a month. The graphs illustrate the variation of the TEC, which reveal two half year peaks. The spring peak is very close to the vernal equinox, but the autumn peak is shifted from the autumnal equinox. The half year peaks are present for all the years with high, medium and low solar activity years (1999 - 2007), but are vanished for the years with very low solar activity (2008 and 2009). The amplitude of the half year peaks show strong correlation to the solar cycle as the peaks are increasing from year 1999 to 2002 and decreasing in the following years. For the summer period there is still correlation to the solar activity, but the scale between the values are much smaller than for the half year peaks.

## 2.6.2 SVD

Singular Value Decomposition, SVD, is a technique for decomposing a matrix into a product of three factors. A plot of the elements will reveal recognizable patterns, when the dataset correspond to samples of continuous variables, as described by e.g. Preisendorfer and Mobley (1988). For the calculated TEC time series, this means, that it will be possible to identify and separate the

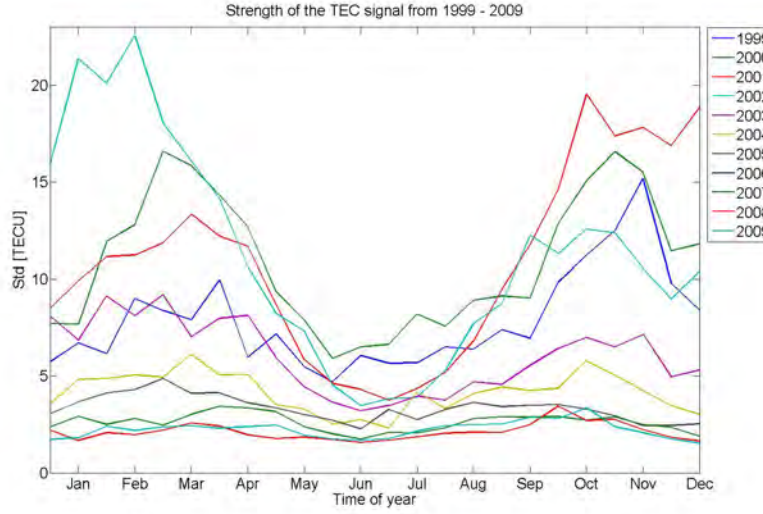


Figure 2.19: Strength of the TEC signal from 1999 - 2009, the std is taken over a time window of half a month.

daily and the yearly components.

This is accomplished by organising the complete time series of vertical TEC into 11 yearly  $96 \times 365$  matrixes. Each value of this matrix corresponds to the mean over 15 minutes. For a given  $m \times n, m \geq n$  real valued matrix  $\mathbf{A}$  the equation for SVD of  $\mathbf{A}$  can be written as in equation 2.16, see Parker (2004).

$$\mathbf{A} = \mathbf{U}\mathbf{S}\mathbf{V}^T \quad (2.16)$$

where  $\mathbf{U}$  is a  $m \times m$  matrix

$\mathbf{V}$  is a  $n \times n$  matrix

$\mathbf{S}$  is a diagonal matrix of size  $m \times n$ .

$\mathbf{U}$  and  $\mathbf{V}$  are both orthogonal matrices.  $\mathbf{S}$  is a diagonal matrix of nonnegative values, called the singular values of  $\mathbf{A}$ , and all other values are zero.

The  $\mathbf{A}$  matrix will correspond to one of the yearly matrixes, the  $\mathbf{U}$  matrix will correspond to the daily variation, the  $\mathbf{V}$  matrix will correspond to the yearly variation, and the  $\mathbf{S}$  holds the ratio between or significance of the singular values.

The procedure for calculating the SVD is normally done in two steps. In the

first step is the matrix reduced to a bidiagonal matrix and the second step is to compute the SVD of that matrix. This can only be done by an iterative method, thus the SVD is computed up to a certain precision. In this case the precision is considered sufficient. The calculation is performed using the LAPACK routine, see Anderson et al (1999).

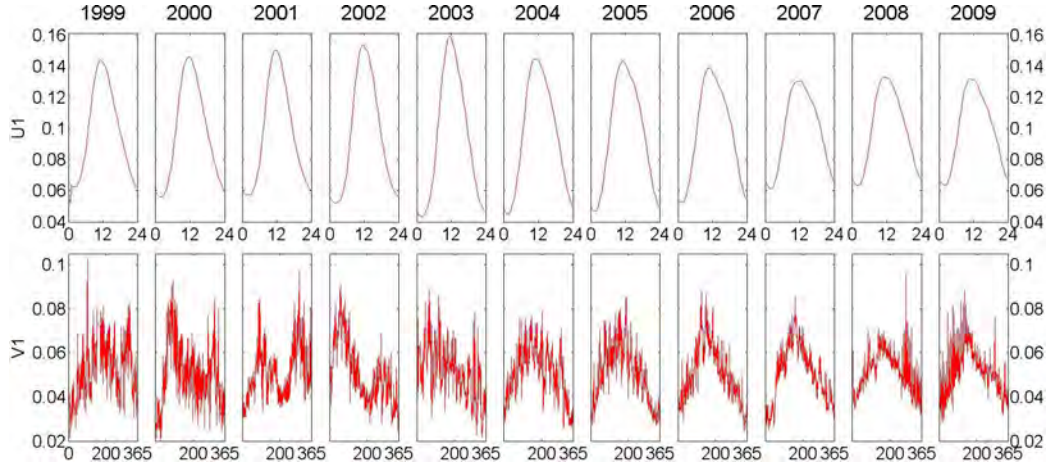


Figure 2.20: The  $\mathbf{U}$  and  $\mathbf{V}$  matrixes for the first singular value for 11 years. The graphs correspond to the first row of the matrices. The x-axis in the  $\mathbf{U}$  matrix is in hour of day in UTC time and in the  $\mathbf{V}$  matrix it is in day of year.

In figure 2.20 is the  $\mathbf{U}$  and  $\mathbf{V}$  matrix illustrated for the 11 years for the first singular value. A very clear daily signal of the total electron content is observed in the  $\mathbf{U}$  matrix. This is expected as the Kalman filter smoothes the data sequentially, epoch by epoch. The signal has approximately the same shape and magnitude for all 11 years. It is positive, meaning that it will always be present, and the peak is at approximately 12.00 hour in UTC-time, which deviates a little from normal. In the  $\mathbf{V}$  matrix it is observed how this daily signal varies through the year. The signal is noisy indicating that there is a very low correlation of the size of the daily signal from day to day. This is expected as the cyclic 27 day variation caused by the sun has little day to day correlation. The signal can be divided into two trends based on the years with high or with low ionospheric activity. From 1999-2003 the signal is higher during the equinoxes and from 2004-2009 is the daily signal peaking in the early summer. Furthermore is the signal becoming less noisy toward 2007-09. This can be interpreted as during solar max the influence from the solar wind is the dominating factor. This influence is semi annual as described by Rishbeth et al (2000). During more relaxed solar activity



Singular Value	1	2	3	4	5
Corr. Coef.	0.95	0.97	0.98	0.99	0.97

Table 2.4: Correlation coefficients for the singular values for each year and the yearly mean sunspot number

years the UV radiation becomes more dominating indicated by the reduced noise for 2004 and 2007 and the signal becomes annual. A noisy period can be observed during winter time from 2008 to 2009. Several of these sudden day to day variations are also present in the GIMs from IGS, but are more pronounced in this dataset. This can be interpreted as smaller geomagnetic storms during relaxed solar years, are more visible in the dataset, because of the general low level of TEC. The signal is still annual during these periods.

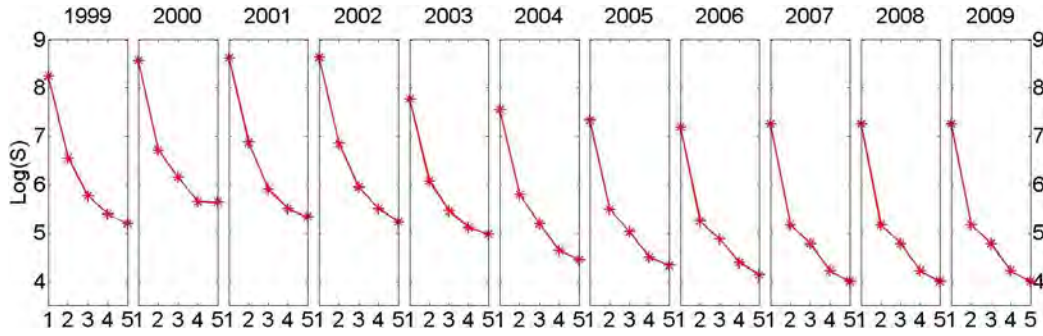


Figure 2.21: First five singular values in the **S matrix**

In figure 2.21 the first five singular values are illustrated for all the 11 years. The ratio between the first and the second is approximately 6 for all of them meaning, that the first singular value dominates the time series for the total electron content. The singular values for each year also show another behaviour. Each set of singular values 1-5 over the 11-year period has been correlated with the yearly mean sunspot number. The correlation coefficients for the first 5 singular values are listed in table 2.4, but the remaining singular values (up to 96) show similar behaviour. The correlation coefficients indicate a strong correlation of the size of the singular values with the sunspot number<sup>2</sup>, and is almost equivalent with what was found in Jakobsen et al (2010).

<sup>2</sup>The used Sunspot Number is the monthly mean number from the Space Weather

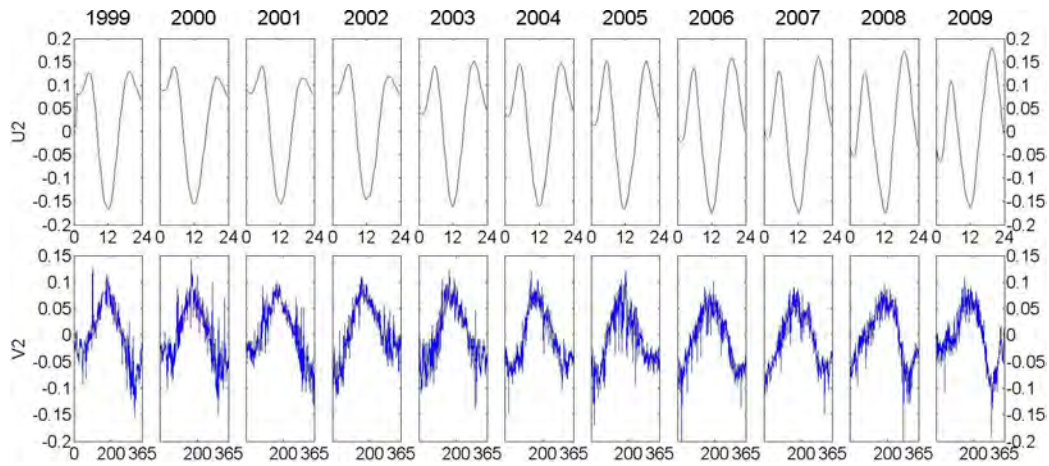


Figure 2.22: The  $\mathbf{U}$  and  $\mathbf{V}$  matrixes for the second singular value for 11 years. The graphs correspond to the second row of the matrices. The x-axis in the  $\mathbf{U}$  matrix is in hour of day in UTC time and in the  $\mathbf{V}$  matrix it is in day of year.

The  $\mathbf{U}$  and  $\mathbf{V}$  matrix for the second singular value is illustrated in figure 2.22. Another clear daily signal is observed in the  $\mathbf{U}$  matrix over the years. This signal is positive during the night time, in the morning and in the evening and negative during midday. Thus, this signal will determine the width of the daily peak as well as it will damp the daily cycle peak. The peak of the damping effect is slightly shifted from the daily cycle peak found for the first singular value. The yearly signal in the  $\mathbf{V}$  matrix also shows a clear annual trend over the years. It is highest in the summer and lowest in the winter. The signal has almost the same low noise for all the years and the day to day correlation is therefore better. This corresponds very well to the variation caused by the length of daylight in the midlatitude region, which is the same for all the years and varies over the year very smoothly.

In figure 2.23 is the third singular value illustrated for the  $\mathbf{U}$  and  $\mathbf{V}$  matrix. The daily signal in the  $\mathbf{U}$  matrix, shows two maxima. The second maximum is very clear for all the years while the first maximum is similar for the years 2003-2009. The signal is both positive and negative, meaning that it will correct the daily signal as shown for the first singular value. It will correct the afternoon depletion of the electron content, so the depletion will appear slower. When looking at the yearly trend, in the  $\mathbf{V}$  matrix, it can be observed that the depletion will be emphasized during the equinoxes, and that the day



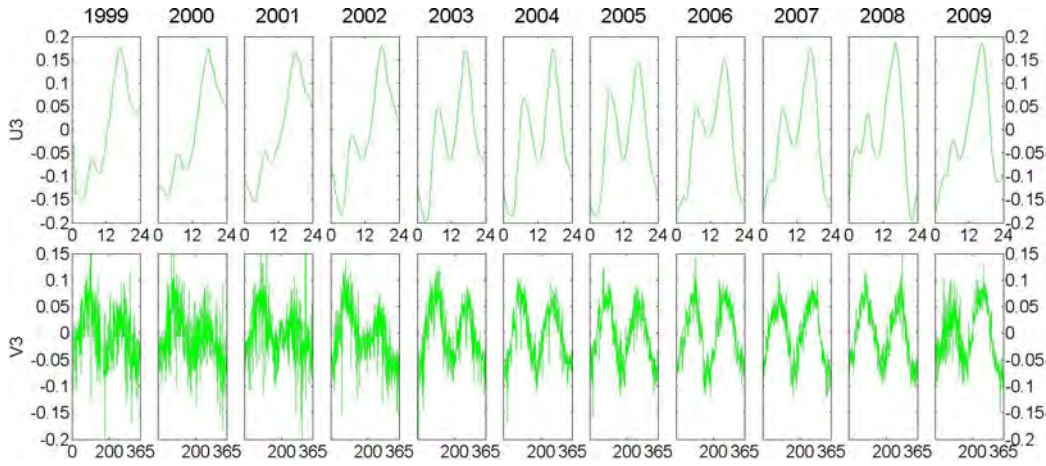


Figure 2.23: The  $\mathbf{U}$  and  $\mathbf{V}$  matrixes for the third singular value for 11 years. The graphs correspond to the third row of the matrices. The x-axis in the  $\mathbf{U}$  matrix is in hour of day in UTC time and in the  $\mathbf{V}$  matrix it is in day of year.

to day correlation for this trend is lower for the years with less ionospheric activity.

For the fourth and following singular values there are no recognizable patterns over the years in the daily and the yearly signals. They can therefore be considered as noise and will be discarded in the recomposition of the ionospheric models.

## 2.7 Use of models

### 2.7.1 Recomposition of yearly models

In the SVD analysis, see section 2.6.2 was the shape and daily variation of the TEC over the year identified. The first three singular values showed recognizable patterns and are therefore chosen for the recomposition of the yearly TEC models. The remaining singular values 4-96 are therefore considered as noise and are set to zero. Furthermore has the values in the  $\mathbf{V}$  matrix been smoothed in order to emphasize the yearly trend and suppress the day to day variation of the size of the daily signal. The result of this recomposition is showed in figure 2.24 for the years 2001, 2004 and 2007. The models illustrate the size and shape of the time varying characteristics. The effect caused by

the length of daylight is similar for the three models and the peaks around equinoxes are more significant during solar max. The effect from the second singular value, the damping of the daily cycle peak, are more visible during summer days and the effect from the 11-year period is shown with significant higher values in 2001, than for 2004 and 2007. The equinox variation of the strength of the TEC signal, shown in figure 2.19, can also be inferred from the models. Models of the variation in the latitudinal and longitudinal direction have been recomposed based on the same procedure as for the TEC. These have been used in the further data analysis as apriori information.

### 2.7.2 Correlation with geomagnetic measurements

The models show the local overall time varying characteristics. The contribution disregarded in the recomposition of the models show the day to day variations. Thus these can be used to detect variations from normal activity. This is accomplished by subtracting the original time series with the model, resulting in a residual matrix. Differentiating this matrix with respect to time will show the speed of change of TEC, thus large values will show sudden changes. These can be correlated with local geomagnetic observations of the magnetic field<sup>3</sup> (The Gaussian summation for the three directions) as is illustrated for two events in 2001 in figure 2.25.

The first is the evening/night between 11th and 12th of April and the second

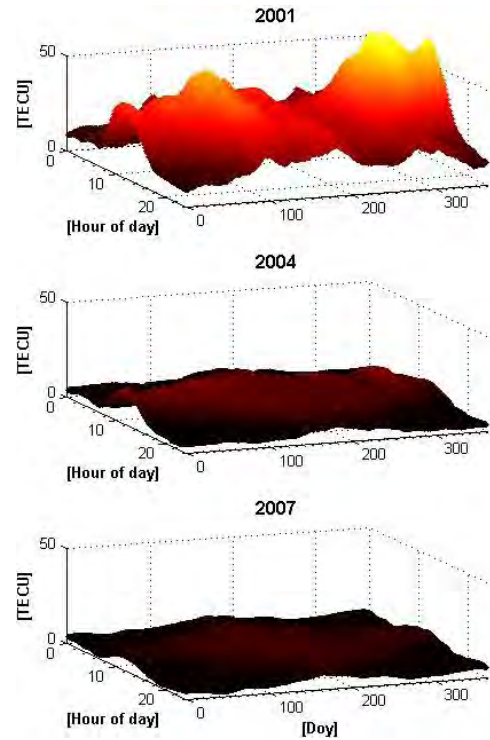


Figure 2.24: Recomposed ionospheric models for 2001, 2004 and 2007.

<sup>3</sup>Data is downloaded from the World Data Center for Geomagnetism, Edinburgh, for the observatory Brorfelde at latitude 55.625 and longitude 11.672, relatively close to the center point used in the TEC time series calculation.

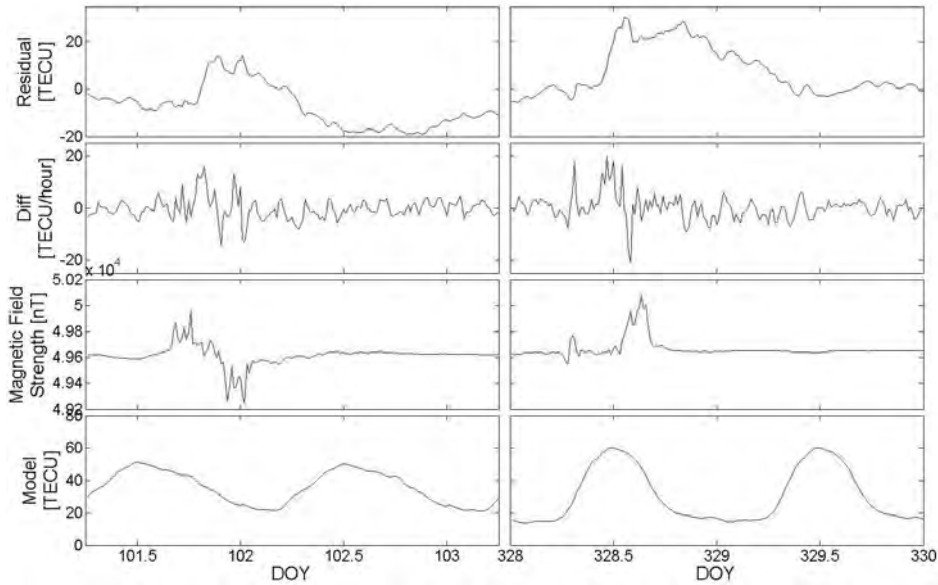


Figure 2.25: Two events in 2001. The *1st* row shows the residual signal, the *2nd* row shows the differentiation of the residual signal with respect to time, the *3rd* row shows the geomagnetic observation data, and the *4th* row shows the recomposed model.

is in the midday/afternoon the 24th of November. Both events are major storms with high Kp values and an impact of -270 nT and -220 nT in the Dst index<sup>4</sup>. For the April event an increase in the TEC from normal activity is observed in the evening, which decreases during the night and becomes negative until the middle of the next day. The differentiated residual signal shows, that the TECU values are fluctuating more in the evening, which are correlated with the local geomagnetic observations. The same correlation between fluctuating TEC and geomagnetic observations are observed for the November event.

These two events also show correlation with global indexes, but this is not consistent for all studied events. This indicates, that local storms in Denmark can be detected and using a combination of local TEC observations with local geomagnetic observations will give a more reliable estimation of the ionosphere variation, than when using global indices or models.

<sup>4</sup>The indexes used is from the World Data Center for geomagnetism, Kyoto, <http://wdc.kugi.kyoto-u.ac.jp/>

### 2.7.3 Implementations in the kalman filter calculation

In case of a space weather application providing real time information of the TEC it is important to implement routines for unexpected failures. These are bound to happen, for instance the data stream from the observation sites can be obstructed for any reason and cycle slips can occur. These failures will cause a reinitialisation of the considered satellites in the kalman filter. The initialisation time can be significantly long resulting in severe deviating TEC values. The reinitialisation is needed in order to set the correct value for the constant part of the L4 observation. The constant part includes the initial phases for the satellite and the rover, and the ambiguity term for each satellite observation, see Jakobsen et al (2008) for an explanation of the variables.

The improvements for the initialisation time are illustrated in figure 2.26. The red curve illustrates the time series for the general processing and it is considered the true value. The blue curve show the processing where zeros have been chosen as starting values and the green curve illustrates the case where starting values of the TEC and the variation of the TEC in latitudinal and longitudinal directions are based on a priori information from the recomposed TEC models.

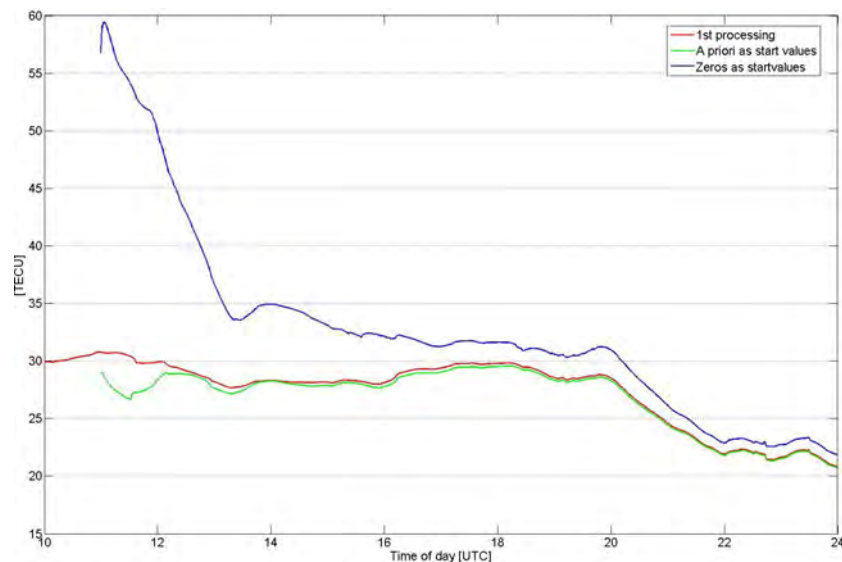


Figure 2.26: The initialisation time with and without using a priori information.

A significant reduction in the initialisation time can be seen. The time series using a priori information converges after approximate one and a half hour, while the time series without a priori information is still off by 1-2 TECU after 12 hours.

It has also been investigated to use a priori information in the kalman filter on an epoch by epoch basis under normal operation. In the implementation of the kalman filter it was unknown if the ionosphere was increasing or decreasing and it was therefore assumed that the ionosphere did not change from epoch to epoch. But by using the recomposed models an indication of an increase or decrease in the TEC could be assumed. This analysis concluded, that the RMS of the residuals is improved, but the improvement is practical non-existent. The sampling rate of 30 seconds is too high in order to reveal any major improvements in the optimisation of the kalman filter, see Jakobsen et al (2008) for further explanation.

## 2.8 Ionospheric model error in a NRTK service

Over the last several years the number of Network Real Time Kinematics (NRTK) services has increased. The advantages in high precision applications in using these services instead of using traditional single station Real Time Kinematic (RTK) systems have shown its great potential. The typical network service model comprises of three or more GNSS reference stations connected via data lines to a central processing facility. This facility estimates the distance dependent errors, ionospheric and tropospheric, across the extension of the network. Interpolation is performed inside the triangles of the reference stations and extrapolation is to some extent performed outside the reference station triangles. Corrections for the distance dependent errors are combined with raw observations and distributed via a data link to the users in the field. The user then applies these corrections and obtains centimetre level of accuracy. The interpolation of the ionospheric correction has great importance for obtaining fast initialisation times and for the level of accuracy primarily during periods with high sunspot activity.

### 2.8.1 Different NRTK solutions

Several competing solutions exist already in the market today, this include the MAC (Master Auxiliary Concept), VRS (Virtual Reference Station), PRS (Pseudo-reference station), i-MAX (individualised Master Auxiliary corrections) and FKP (Flächen-korrektur-parameter) methods.

The general steps involved in a NRTK solution is illustrated in figure 2.27 as well as the relation between the different solutions. It can be seen that the VRS, PRS, FKP and i-MAX solutions can all be realised from MAC data.

**MAC** data consist of the raw observations of the reference stations in the entire network where the nuisance parameters such as clock errors, and integer ambiguities are subtracted, H.-Euler et al (2001).

**FKP** data includes the non-dispersive and dispersive corrections and they are represented by coefficients to a polynomium surface referenced to a physical master station. The order of the polynomium can be chosen to fit the best physical characteristics of the ionosphere and troposphere. The FKP data (raw observations and polynomium coefficients) are sent to the rover, which apply optimal corrections at the rover location. The interpolation procedure is performed on the rover.

**In VRS** is non-physical observations generated where the position of a physical reference station is displaced to a virtual position, typically within few meters of the rover location. The virtual observations are sent to the rover as if it was a true reference stations.

**In PRS** is non-physical observations also generated with a displacement of the position of a physical reference station to a virtual position, but the virtual baseline in this procedure is typically several km.

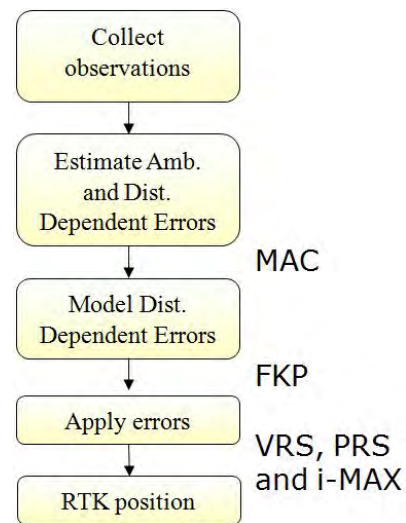


Figure 2.27: The general processes involved in NRTK services and the relation between the different solutions, Takac and Zelzer (2008).

In **i-max** is non-physical observations also generated, but individualised corrections for the location of the rover are applied to the observations of a master station before they are transmitted to the rover. The network can use higher order approximation functions in order to interpolate the corrections.

As can be seen is the VRS, PRS and i-MAX very similar, but the main difference between these and the MAC and FKP procedure is that the interpolation of the dispersive and non-dispersive corrections are performed by the network. For a further description of the 5 solutions and their relationship, the reader is referred to Takac and Zelzer (2008).

### 2.8.2 Model error of the ionospheric correction in a VRS NRTK

The precise implementation of the interpolation process of the corrections in a NRTK service is proprietary information and extraction of these corrections is not possible before they are calculated and sent to the user. The corrections must therefore be extracted using an alternative method, and using the received data stream from the NRTK service seems obvious. An illustration of this is shown in figure 2.28, where the general process shown in figure 2.27 is separated into two segments to show the process of a VRS solution.

The rover collects observations from the GNSS satellites and calculates a standard code based position and sends this information to the network service. The network service collects information from the same GNSS satellite and synchronise them. The service then processes these data for each satellite and for each station, in order to estimate the integer ambiguities and distance dependent errors. These estimates for each station are combined into a model for each satellite and new virtual phase observations are generated at the position send by the rover. The rover can then apply these corrections and calculate a RTK derived position.

It is possible to evaluate the NRTK service interpolation method of the dispersive corrections in the positioning domain, however using this approach many parameters are involved, which may or may not refer to the process in the rover. The rover equipment on the market today consists of receivers

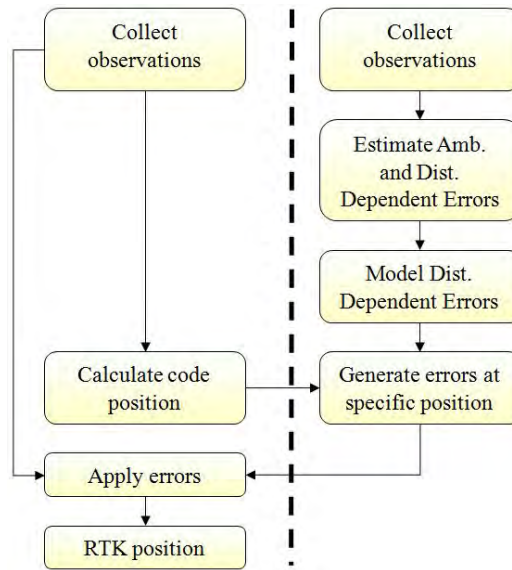


Figure 2.28: The procedure for calculating a position using the VRS approach separated into two segments. The rover tasks is illustrated on the left side while the network service is on the right, see Jakobsen (2009).

with different brands, different age, different firmware and different antennas, which all affect the positioning accuracy. Furthermore influence from the non-dispersive corrections from the network service can also affect the position accuracy. Thus evaluation of the NRTK service must be done in the observation domain rather than in the position domain.

The difference between the ionosphere correction calculated at the network provider and the true correction, referred to as the model error, is illustrated for a 1 dimensional case in figure 2.29.

Each reference station observes the true value of the ionospheric error and the NRTK service interpolates between them using a proprietary model. The true ionospheric error is varying between the two reference stations in an unknown manner and the inter-

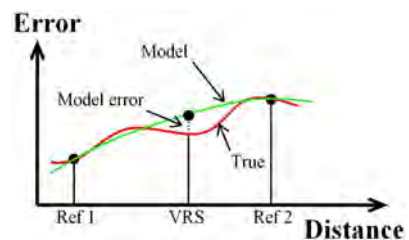


Figure 2.29: 1 dimensional illustration of the NRTK service ionospheric model error.



polation algorithm can estimate a correct value several km. away from the nearest reference station, while the contra dictionary could also happen, that an erroneous value are estimated close to the nearest reference station.

### 2.8.3 Extracting the variation of the model error

The variation of the true ionospheric error for a given reference station can be computed using the geometry-free L4 observation. The  $L1$  [m] and the  $L2$  [m] carrier phase observations to a given satellite  $s$  can be expressed as in equation 2.17 and 2.18 as described for instance by Feng (2008).

$$\begin{aligned} L1^s = & \rho^s + \delta_{orb}^s + c(\delta t^s - \delta t) + \delta_{I,1}^s + \delta_{trop} + \\ & \lambda_1 (N_1^s + \varphi_1 - \varphi_1^s) + \epsilon_1 \end{aligned} \quad (2.17)$$

$$\begin{aligned} L2^s = & \rho^s + \delta_{orb}^s + c(\delta t^s - \delta t) + \delta_{I,2}^s + \delta_{trop} + \\ & \lambda_2 (N_2^s + \varphi_2 - \varphi_2^s) + \epsilon_2 \end{aligned} \quad (2.18)$$

where  $\rho$  is the geometric distance

$\delta_{orb}$  is the orbital error

$c$  is the speed of radio waves in vacuum

$\delta t$  is the clock error for all components

$\delta_I$  is the ionospheric phase delay

$\delta_{trop}$  is the tropospheric propagation delay

$\lambda$  is the wavelength

$N$  is the integer ambiguity

$\varphi$  is the initial phase

$\epsilon$  is the receiver phase noise, incl. the phase multipath

subscript  $_1$  and  $_2$  refer to the  $L1$  and  $L2$  carriers.

The  $L4$  observation can then be expressed as in equation 2.19

$$L4 = L1 - L2 = I + \lambda_1 (N_1^s + \varphi_1 - \varphi_1^s) - \lambda_2 (N_2^s + \varphi_2 - \varphi_2^s) \quad (2.19)$$

where  $I$  refer to the total electron content in the ionosphere.

Assuming that no cycle slips occur and that the initial phases are constant over a short period of time, the only varying part is the variation of the TEC.

The NRTK service generates the distance dependent errors to the user as if it was a true reference station. Thus a VRS generated at the exact same location of a physical true reference station opens for the possibility to compare the observations. This means that by subtracting the two L4 observations, the model error can be analysed. The variation of this model error can then be expressed as in equation 2.20.

$$\sigma(I_{modelerror}) = \sigma(L4_{true}^s - L4_{VRS}^s) \quad (2.20)$$

where *true* refer to the true reference station

*VRS* refer to the virtually generated reference station.

#### 2.8.4 Real time data collection for the VRS

Since most end users apply the VRS generated by the NRTK service directly in real time, it is important to evaluate the real time data stream send by the NRTK service. The procedure used to accomplish this is illustrated in figure 2.30. This procedure can be used for the generation of a single VRS in the time period of the connection for a pre-defined location. It is possible to generate multiple VRS (at different locations) for the same time, but this requires multiple subscriptions/data connections to the NRTK service provider.

For establishing a connection and send a location to the NRTK service provider a modified version of the BKG NTRIP (Networked Transport of RTCM via In-

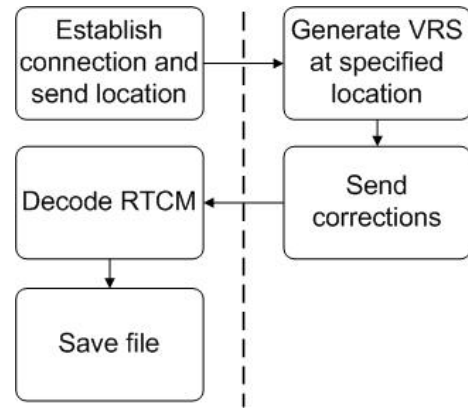


Figure 2.30: The procedure for collecting real time data from a NRTK service provider. The task on the left is performed by the client and the tasks on the right are performed by the NRTK service.

ternet Protocol) client<sup>5</sup> version 1.6.1 has been used. In the binary public version it is only possible to input the desired longitude and latitude for the VRS, the height information is hardcoded. The source code however is available and is easily altered, so the ellipsoidal height can be inputted as well. Using this client it is also possible to decode the received RTCM<sup>6</sup> data stream and save this to a file on a hard drive. The file is stored in the Rinex format version 2.11, but the client is also capable of storing in Rinex version 3. The NRTK service software acts by the request from the client as it was a normally connection coming from a subscriber. It generates a VRS at the location specified in the NMEA string and start sending corrections back to the client.

This method has only been used in order to verify the connection between the real time generated VRS and a post processed VRS, see section 2.8.6.

### 2.8.5 Post processed data collection for the VRS

In order to compare the model error variation for multiple VRS, it is important that the data are collected under the same ionospheric conditions. As the ionosphere is varying over time, this implies that the VRS's must be generated at the same time. In order to do this in real time multiple subscriptions to the NRTK service would be required. The considered NRTK service also offer post processed (PP) VRS by inputting the coordinates at the desired location via a homepage, and this procedure has been used to collect the VRS data used in the analysis.

A number of operational physical reference stations exist already today. These are operating independent of the NRTK service and cover the same area as the stations used by the NRTK service. They are all geodetic receivers, put up in environments to minimize the effect from multipath. In total 9 stations has been chosen based on the distance to the nearest NRTK reference station. The location of the selected stations and the NRTK service stations can be seen in figure 2.31. Post processed VRS for the selected

---

<sup>5</sup>Developed under GNU General Public License for Networked Transport of RTCM via Internet Protocol (NTRIP) to receive GNSS streaming data over the Internet. [http://igs.bkg.bund.de/index\\_ntrip.htm](http://igs.bkg.bund.de/index_ntrip.htm)

<sup>6</sup>The received data are sent in the RTCM format version 2.3



Figure 2.31: Location of the selected stations based on the distance to the nearest NRTK reference station.

stations have been generated in 24 hour Rinex files with a sampling rate of 30 seconds for the day of year 45 and 51 2009.

### 2.8.6 Verification of the method

Even though the exact location has been sent to the NRTK service, this does not imply that the VRS is actually generated at this precise location. In the specification of the Rinex format header files, it is possible to indicate an approximately position, but in the received data stream from the NRTK service this position is indicated as (0,0,0). However a position is given as a comment line specifying a NMEA latitude and longitude, but a height information is missing. It has been verified that the latitude and longitude of that position is equal to what was sent.

A test has been performed by gathering 30 minutes of VRS data with a sampling rate of 1 second at the exact location of a physical reference station

	Northing	Easting	Height
Dist [mm]	3.0	14.0	18.0
RMS [mm]	1.7	1.3	2.3

Table 2.5: The result of a PP baseline between a VRS and a physical reference station.

and then calculates a baseline between these two datasets. The result is shown in table 2.5

Ideally should the result of this baseline be zero, but a number of factors are different in the two data sets. These include:

- **Multipath:** This effect is not distance dependent and impossible to model by the NRTK service. The effect will therefore not be present in the VRS data set. The difference is however small because a choke ring antenna is used on the physical reference station.
- **Antenna models:** The phase center for the antenna is elevation dependent. For the physical station the correct antenna model can be applied in the processing, but the antenna specification for the VRS is handled as an unknown.
- **Cycle slips:** The VRS is generated without any cycle slips. But unreparable cycle slips in the physical station data set can be present.
- **Receiver noise:** This effect will be present in the physical station data set and removed by the NRTK service in generation of the VRS.
- **SNR:** The Signal to noise ratio values for each satellite link are not specified for the L1 and the L2 carrier observables in the VRS data set, thus this information cannot be used to weight the observations.

Therefore must a baseline of a small length be expected. The observed length is also very small. This eliminates the possibility that the difference between antenna phase center and antenna reference point are entered wrong. It is therefore concluded that the phase center of the VRS is at the same location as the phase center for the physical reference station.

The data analysis in this report is based on PP VRS via the homepage from the NRTK service. The procedure used by the service for generating the PP VRS might be different than the procedure used in the real time case. Two

data sets have therefore been generated with a VRS entered as the same coordinate. One VRS via the real time procedure and one VRS via the PP procedure. Ideally should each L1, L2, C1 etc. observation to each satellite be equal, but this has shown not to be the case. For a satellite pass of 15 minutes is the difference between the L1 observations for instance fluctuating in the interval of 7 cycles. But an analysis of the L4 observation for the same satellite pass show differences fluctuating in the interval of 1.5 mm. and the correlation coefficient between them is 1.0. This trend is also observed on the other satellites. Furthermore is the number of observations per satellite equal for all observed satellites in the two cases. It is therefore concluded that the interpolation procedure used in the real time case and in the PP case implemented in the NRTK service is equal and the results of the analysis made in this report can be extended to include the real time case as well.

### 2.8.7 Elevation angle dependency

The signal travels through a larger part of the medium at lower elevations. It is therefore expected that the model error is affected by this. An example of a representative satellite pass is shown on figure 2.32 (a). At low elevations, beginning and end of the graph, is the variation of the model error also larger.

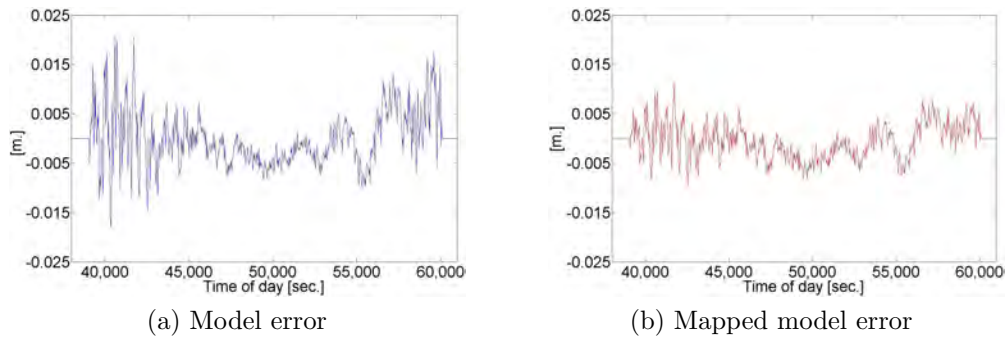


Figure 2.32: Example of a satellite pass

The different satellite passes for 24 hours have therefore been grouped into elevation bins of  $5^\circ$ . In figure 2.33 the standard deviation of these bins is plotted for two stations. There are more satellite passes for lower elevations and the thick red line is the mean value. This illustrates that the NRTK service generally models the ionospheric model error worse at lower elevations.

There is no significant difference whether the satellite is rising or falling. The shape is observed for all the stations, which means that this effect is present at all locations at all times and both in the interpolation and extrapolation area.

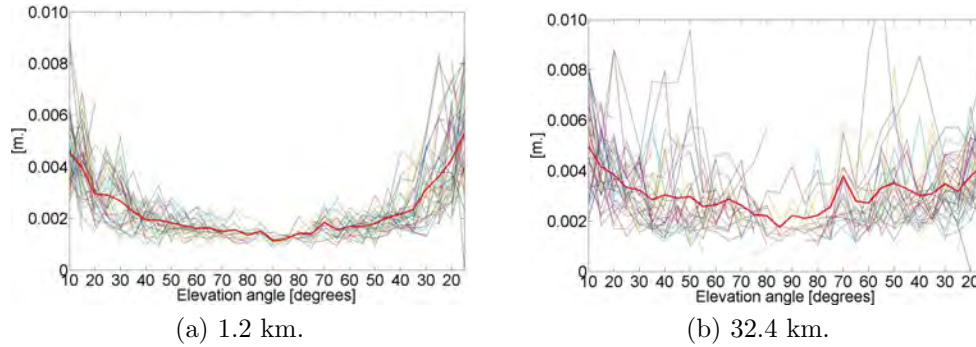


Figure 2.33: Standard deviation of the model error for two stations with different distance to nearest reference station.

The two stations have a distance to nearest reference station of 1.2 km. and 32.4 km. and it can be seen on the figure, that the standard deviation of the model error are varying more for greater distances, though the mean value is similar for the two stations.

In order to compare satellite passes it is needed to remove the elevation effect from the observations. In the further analysis, this is done by using the mapping function described in section 2.3.1. An illustration of the effect from using the mapping function is shown in figure 2.32 (b). This does however not remove all the effect, so an elevation mask of  $20^\circ$  has also been used in the further analysis.

Two days, day of year 51 and 45 in 2009, have been chosen to represent a day with low ionospheric activity and a day with higher ionospheric activity. The daily TEC cycle for the two days can be seen in figure 2.34. The level on day 51 is extremely low with a peak value at approximately 8 TECU. The peak value for day 45 is also low, but

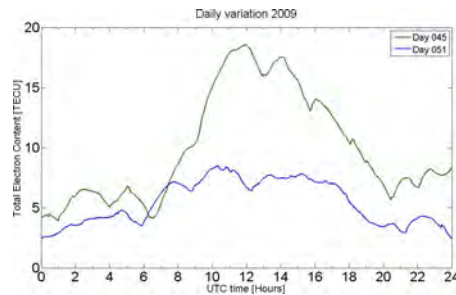


Figure 2.34: The daily TEC cycle for two days in 2009. The cycles have been taken from the calculated time series analysed in section 2.5

significantly higher than day 51. The main difference between the cycles is in the sunlight hours.

### 2.8.8 Day to day variation

All satellite passes for the two days has been mapped and truncated for elevations below  $20^\circ$ . The standard deviation of the ionospheric model error over 10 minutes has then been calculated and the mean value for visible satellites is then calculated. The difference for two days for the station at 39.7 km. from the nearest reference station is illustrated in figure 2.35.

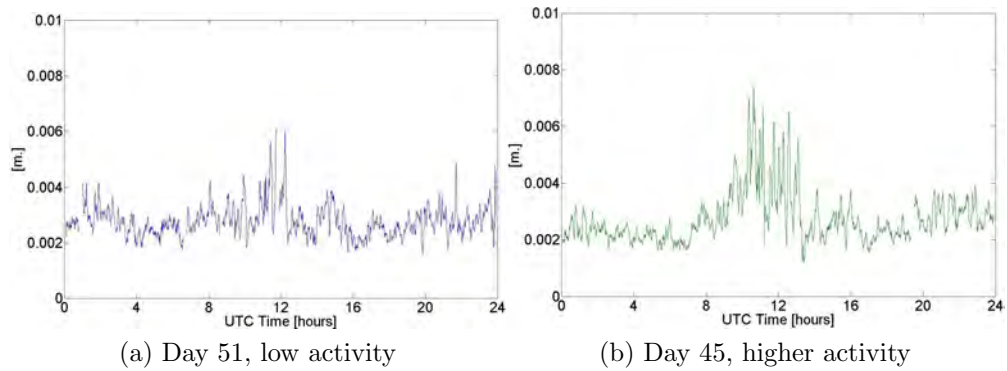


Figure 2.35: Mean standard deviation for visible satellites of the ionospheric model error for two days for the station 39.7 km. from the nearest reference station.

Even though the peak on the day 51 TEC cycle is very low a dependency of the daily cycle can be observed for the model error during midday. The level of the model error is low almost constant during the rest of the day 51. Day 45 shows the similar trend, but it is magnified, characterized by having a larger width and higher values for the midday peak. A dependency on the day to day variation of the ionospheric activity is therefore identified. This dependency is similar for all the stations, but is largest for the shown station.



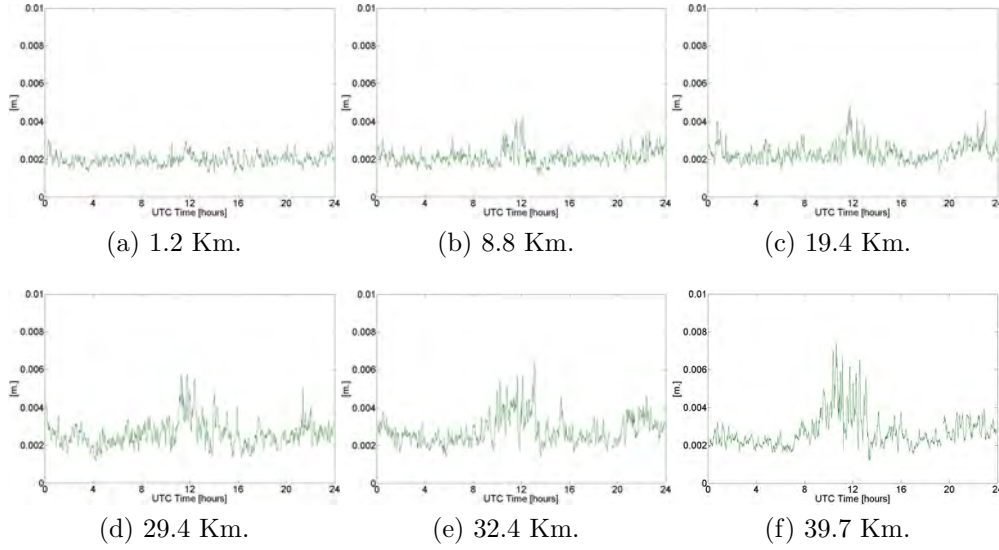


Figure 2.36: Mean standard deviation for visible satellites of the ionospheric model error for stations in the interpolation area. The length refers to the distance to nearest reference station.

### 2.8.9 Dependency on the distance to nearest reference station

In figure 2.36 (a) to (f) is listed the considered 6 stations for day 51 in order of increasing distance to nearest reference station. All the stations have the same low level during the night, but as the distance increase the effect from the ionosphere also increase. The effect correlates with the daily peak of the TEC, see figure 2.34. An increasing contribution as the distance increase in the evening/early night is observed though, which has a larger size than expected, based on the small increase in the TEC cycle. A possible explanation could be that constraints on the ionospheric activity exist in the NRTK processing during night time, which can have a higher model error as result.

In the extrapolation area there is not the same clear dependency on the distance to nearest reference station. In figure 2.37 (a) to (c), is the mean standard deviation for visible satellites of the ionospheric model error for stations in the extrapolation area illustrated. The figures are listed in increasing distance to the interpolation area. The daily cycle dependency is clearly vis-

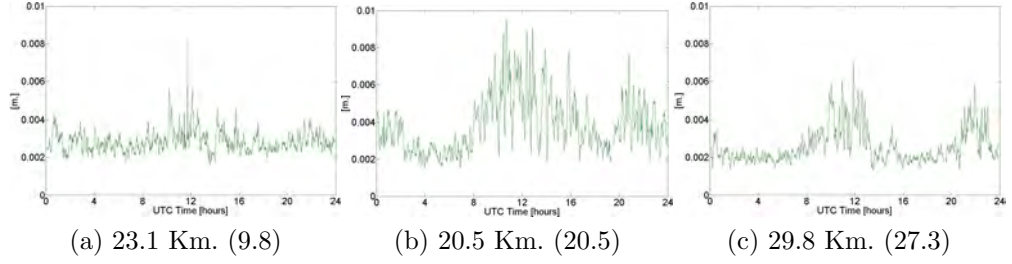


Figure 2.37: Mean standard deviation for visible satellites of the ionospheric model error for stations in the extrapolation area. The length refers to the distance to nearest reference station. Length in parentheses refers to distance to the interpolation area.

ible, but the closest station has the largest magnification. A dependency in the distance to the interpolation area is not visible either. Instead a dependency on the geometry of the NRTK system is visible. This can be verified by looking at the station location in figure 2.31. The station at 20.5 Km. from nearest reference station is located both north and east of the interpolation area. The station at 29.8 Km. from nearest reference station is located east of the interpolation area and the station at 23.1 Km. from nearest reference station is located south of the interpolation area. The effect is lowest for the station at 9.8 Km. from the interpolation area, so a dependency on the distance to the interpolation area exists, but this is smaller than the geometry dependency. Figure 2.37 also show, that the night time effect is magnified in the extrapolation area compared to the effect from stations in the interpolation area.

## 2.9 Conclusion on ionospheric variation effects

The ionosphere is in its nature varying over time and can have significant effect on satellite navigation signals. The variations show cyclic behaviour with daily, seasonal, and 11 year periods, but also short term variations are observed. The characteristics of the variations vary dependent on the latitude and on the vertical component. Different models exist describing the TEC on a global basis, but the resolution is not sufficient in order to analyse regional

or local variations.

In the following is the conclusions relating to the variations of the ionosphere found in this report summarized.

The daily, yearly, and 11 year cycles, present in the calculated TEC time series, can be separated using a svd analysis. The first singular value is very dominant corresponds to how the daily signal varies over the year. The second singular value corresponds to how the width of the daily signal varies over the year, and the third singular value shows a yearly variation of the daily signal with peaks around the equinoxes.

Using the generated TEC models can abnormal ionospheric activity be identified and it has been shown, that this can be correlated with local geomagnetic observations. This shows the potential of combining these two different types of local observations to provide a more reliable space weather service.

The initialisation time of the kalman filter, used in the calculation of the TEC time series, can be significantly improved, by using a priori information as starting values.

The ionospheric model error in a NRTK service is primarily dependent on the elevation angle with a standard deviation up to 10 mm. for low elevations.

With increasing distance to nearest reference station is the standard deviation for the ionospheric model error also increasing. This trend is magnified for days with higher ionospheric activity.

In the extrapolation area is the standard deviation of the ionospheric model error dependent on the geometry of the nearby interpolation area, but has the same elevation, distance, ionospheric dependencies as stations in the interpolation area.



# Chapter 3

## Characteristics of multipath

### 3.1 Effects on GNSS signals

The term multipath describes the situation where the signals from the GNSS satellites travel over multiple paths before they arrive at the antenna front end. In an indoor environment can multipath or multipath interference be described by different phenomena illustrated in figure 3.1.

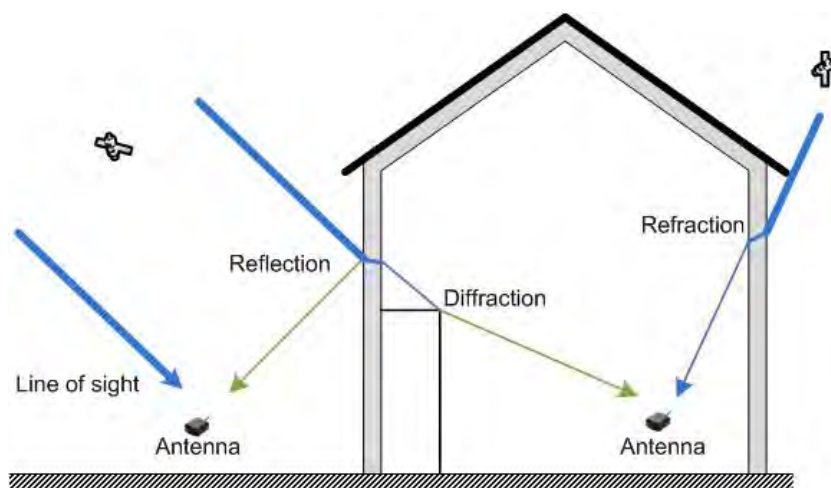


Figure 3.1: Indoor multipath environment.

Common to these phenomena is that, compared to a direct line of sight (LOS) signal, they all suffer from attenuated power. The impact can result

in partial to total loss of signal tracking and/or tracking errors, depending on the severity of the effect and the receiver tracking characteristics. These effects are evident in a receiver's measure of the carrier to noise ratio,  $C/N_0$ . That is an instantaneous measure of the ratio of carrier power present to noise power density measured per Hz bandwidth. The  $C/N_0$  is the best possible value in order to evaluate the signal quality present at the input to a GNSS receiver.

The reflected and diffracted signals both travel a longer distance before arriving at the antenna. This causes a pseudorange error, which again causes errors in the positioning domain. The extra length, called the multipath delay, depends on the geometry of the objects.

Refraction occurs when a radio wave travels from one medium to another which has different propagation velocity. For a medium, for instance a wall, inserted between the transmitter and the receiver, will the incidence angle equal the final refracted angle. When the signal has penetrated the medium it will be attenuated, part of the energy is lost due to refraction and energy absorption by the materials. In worst cases the signal will be totally blocked. Klukas et al (2004) has investigated the penetration effects of building materials at the GPS L1 frequency. Attenuations and effect on the pseudorange for the study are listed in table 3.1. The walls consisted of two 2.3 cm. thick plates separated by 14 cm. for the plywood and two 1.1 cm. plates separated by 14 cm. for the gyprock. The signal penetrated the walls directly, that is at approximately  $90^\circ$ , higher values must be expected at lower angles. It can be seen, that the effects from gyprock is less than plywood. The effect on the pseudorange for the cinder block could not be listed due to uncertainty of LOS signal existence.

Material	Attenuation [dB]	Effect on pseudorange [m]
Gyprock	0.5	$\approx 0$
Plywood	2.4	0.4
Cinder block	23.0	N/A

Table 3.1: Material effects on the GPS L1 LOS propagation measurement.

Reflection occurs when a propagating radio wave encounters the surface of another object, which has different electrical properties. The wave is partially reflected back, where the reflection angle equals the incident angle and

partially transmitted into the medium of the object. The energy of the reflected signal is therefore weaker than that of the incident signal. There are two kinds of reflections: **Specular** occurs when the surface of a reflector is smooth and **diffuse** occurs from an uneven/rough surface. The reflected signals may exist in all directions, because the angle incidence varies over the surface due to its roughness. Signals due to diffuse reflection carry less energy in a certain direction compared to specular reflection. The properties of the GPS signal have changed, compared to a LOS signal, when it arrives at the antenna. This includes the amplitude, phase, polarization, angle of arrival, and propagation path length.

Diffraction is the phenomena when an electromagnetic wave meets an obstruction in the propagation path, the wave is not totally blocked. Some of the energy is bent and spread into the area behind and often occurs due to edges or corners of the objects. Even though the path from satellite to antenna has a clear LOS, signal losses may occur. The signal losses can be avoided if approximately 56% of the first fresnel zone is clear of obstructions, see Parsons (2000).

For GPS signals, where the distance between the transmitter and the obstruction along the LOS is much larger than the distance between receiver and the obstruction along the LOS, the first fresnel zone radius,  $r$ , can be simplified as given in equation 3.1.

$$r = \sqrt{\lambda d} \quad (3.1)$$

where  $\lambda$  is the wavelength, 0.1903m for the GPS L1 signal.

$d$  is the distance between the receiver and the obstruction along the LOS path.

This means, that an obstacle 15m from the antenna along the LOS, will cause diffraction loss if it is within approximately 0.95m from the LOS signal path ( $r \cdot 0.56 \approx 0.95m$ ). The characteristics of diffracted signals differ greatly from one solution to another and are therefore difficult to model.

### 3.1.1 Pseudorange error

The longer travelled distance will have an influence on the correlation peak in the receiver tracking loop. In the ideal world will this peak be a pristine triangle, but when additional signals arrive shifted in time, they will contribute to secondary peaks, and the early and late correlator samples may not be centred on the true arrival time of the direct ray. In figure 3.2 is the carriers for a direct and two reflected rays shown. Constructive interference has the same angle as the direct, and the length is therefore added. In contrast to the destructive interference, where the angle is  $180^\circ$ , and so will have a shorter length than the direct ray. In general will the phase of the reflection vary and assume all possible angles relative to the direct.

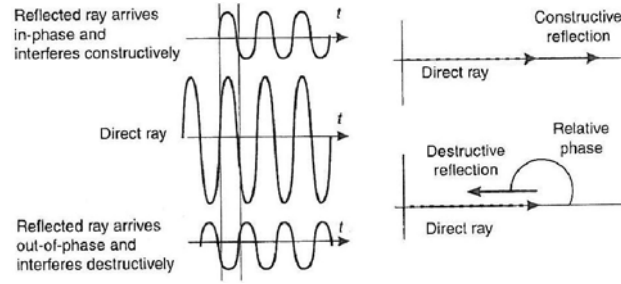


Figure 3.2: In-phase and out-of-phase reflected carrier relative to the direct ray, Misra and Enge (2006).

Delayed rays will always create a delayed correlation peak, this is illustrated in figure 3.3.

The ratio of the direct peak amplitude to the delayed peak amplitude is given by  $\sqrt{C/P_M}$ , where  $C$  and  $P_M$  is the power in the direct and delayed signal respectively. If the interference is constructive, then the late peak will be added to the earlier peak, and if the interference is destructive will it be subtracted. The late peak will also be shifted in time. If this relative time delay is long, that is the rising edge of the delayed peak, do not touch the late correlator sample, will the multipath interference not cause any pseudorange error. This condition is dependent on the spacing of the correlator. If a wide correlator is used, then will the pseudorange errors not exceed 450m. while using a narrow correlator will the error not exceed 315m. These numbers refer to a chip width of  $1 \mu s$  approximately 300m (the GPS C/A code).



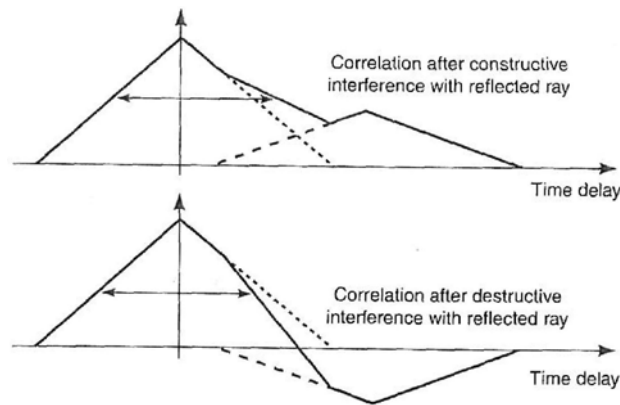


Figure 3.3: Correlation peak in the presence of constructive and destructive interference, see Misra and Enge (2006).

If the time delay is short will the correlator pairs move with pseudorange errors as the result. For constructive interference will the correlator pairs be moved slightly to the right, hence the measured pseudorange is longer, while destructive interference will move the correlation pair to the left. This means that even though the signal is delayed, will destructive interference cause the pseudorange to be measured short.

In figure 3.4 is the pseudorange error bounds for the C/A code illustrated for different correlator spacing,  $d$ . As the relative phase varies between  $0^\circ$  and  $180^\circ$ , will the multipath error vary between the upper and lower bounds, constructive and destructive interference respectively.

If the direct signal is blocked and not received at the antenna front end, can the pseudorange error extends to unlimited size, depending on the delay caused by the surrounding environment.

## 3.2 HS GNSS

High Sensitivity (HS) GNSS receivers and methods have been developed to enhance conventional GNSS receivers. With these new techniques it is possible to use GNSS receivers in various signal degraded environments. It has been shown by Hu (2006), that HS GNSS receivers can track signals,

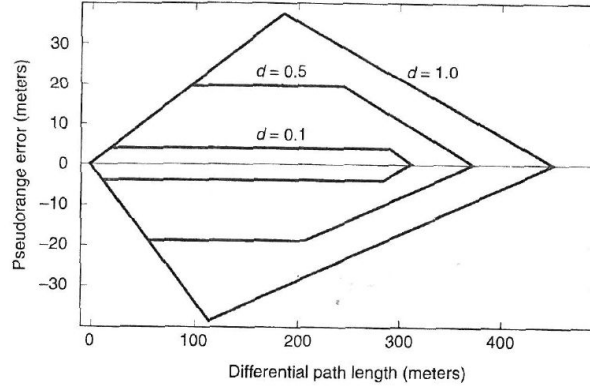


Figure 3.4: Bounds on the C/A code pseudorange error due to multipath for different correlator spacing.  $d=1$  means a wide correlator and  $d=0.1$  means a narrow correlator. The amplitude of the multipath is 12 dB below the amplitude of the direct ray, see Misra and Enge (2006).

which are 13-15 dB lower than with a standard GNSS receiver and 25 dB lower than the power of an undegraded signal.

The processing task for obtaining measurements from weak signals depends on the context. The signal acquisition phase is difficult while maintaining the signal tracking is relatively easy. Weak signals are acquired and tracked using long signal integration time. For the C/A code the length of the code sequence is 1 ms. With  $N$  ms of coherent integration will the signal power increase by  $N$  and the noise power increase by  $\sqrt{N}$ , which result in a gain of  $\sqrt{N}$  in terms of  $C/N_0$ . This is illustrated for  $N = 3$  in figure 3.5.

After 20 ms there is a possible navigation bit transition, which can change the phase of the correlation peak. Unless the navigation bits are known, this limits the coherent integration of the GPS signal. The integration period is also limited by residual frequency errors due to the receiver motion. Furthermore, will the receiver oscillator error induce an additional reduction in the  $C/N_0$ , that increases with increased integration time, see Watson et al (2006).

Non-coherent integration, obtained by applying a non-linear function to the correlator outputs for removing the impact of data bits, can be much longer

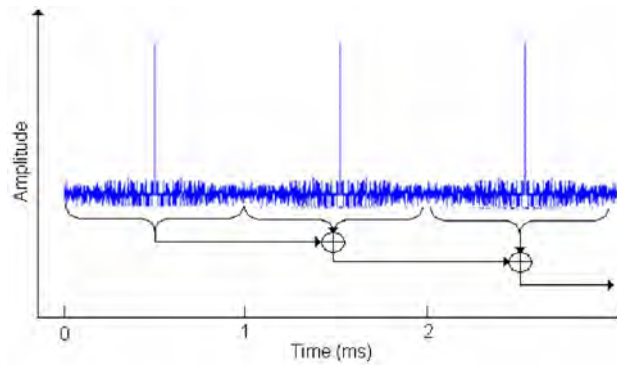


Figure 3.5: Sequential coherent integration, see MacGougan (2003).

than coherent integration, see for instance Borio and Lachapelle (2009). However since this procedure involves squaring or other non-linear operations, it also implies squaring losses relative to pure coherent integration of the same net duration.

Another technique has been developed for searching for weak signals and is called massive parallel correlation. It is based on simultaneous evaluation of GPS signal correlation over the entire range of possible code delays/carrier frequencies as described by van Diggelen (2001). In signal degraded environments with significant signal attenuation, a receiver experience frequent loss of lock, but by computing all possible correlation simultaneously ensures that the correlation peak will be detected. Thus, by providing more coverage over the probable noise/dynamics influenced code/carrier space, the limits of the tracking threshold can be enhanced.

### 3.3 Controlled kinematic behaviour

Previous test of multipath characteristics has been done in the static case. In order to characterise the multipath interference under kinematic conditions a test platform is needed. A solution for such a platform is described in the following.

In the static domain a well-known procedure for making tests of GNSS equipment is to setup the GNSS antenna fixed on a tripod. The main function of

the tripod is to maintain the antenna at this exact location in an Earth Centred Earth Fixed (ECEF) coordinate system throughout the test period. The reference point is important to locate in an absolute sense, since it reveals any systematic errors in the testing equipment and not just relative errors. Using a tripod has also other advantages in the static domain, these include

- Portable
- Multiple
- Flexible
- Statistical

The portability gives the user the opportunity to bring the tripod in different kind of GNSS environments to perform tests. This can be indoor or outdoor, as well as various urban and countryside scenarios. Multiple tripods can be set up with different equipment at the same time, whether this is for tests under the same or deliberate different conditions. Since the tripod is static will repeated measurements make a good foundation to calculate statistical parameters, whether the test is performed in the observation or the positioning domain. Making the transition from the static domain into the kinematic domain, and at the same time sustain the advantages from the tripod, makes the testing procedure more difficult. The reference point becomes a reference geometry and the position is no longer constant, but becomes a function of time. The demands for controlling the kinematic movement become very important.

In the following section it is described how this has been accomplished by designing, producing and verify a slot car track with the kinematics of the test equipment controlled by a computer.

### 3.3.1 The design of the slot car track

The overall design of the slot car track consists of the following components, which are also illustrated in figure 3.6.

- The track
- The car
- The position detector sensors

- The motor control
- The microcontroller
- The control panel
- Power supply and DC-DC converter
- The external GNSS receiver
- Logging software

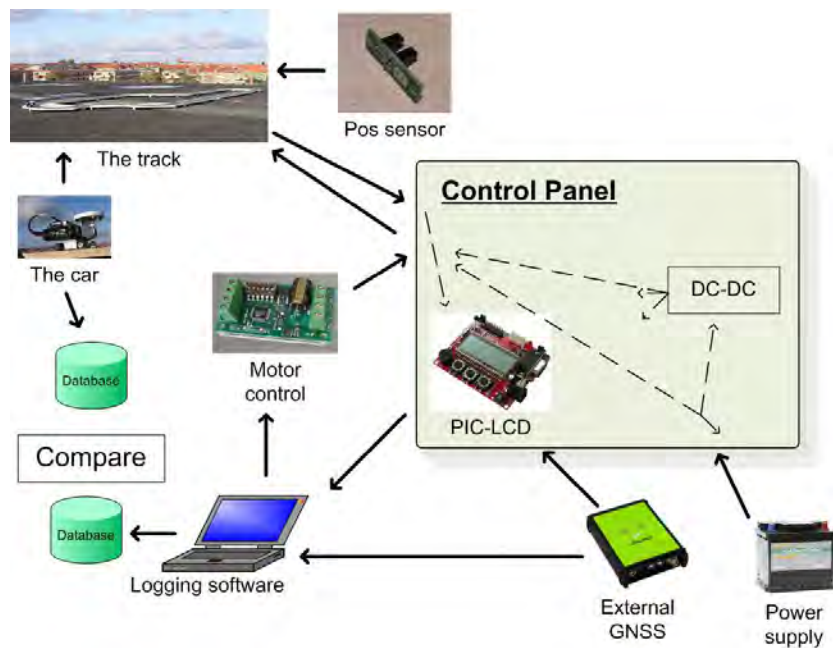


Figure 3.6: Overall system design of the slot car track.

The function and implementation of these are described in the following sections.

#### 3.3.1.1 The track

The main function of the track is to fix the reference geometry and hold it steady in an ECEF coordinate system throughout the test period. The track consists of a various number of different plates, which can be assembled in various ways to setup different routes. This sustains the flexibility property of the track. The plates have been made by cutting standard 244x122 cm. of 16 mm. chip/particle boards with melamine on each side into pieces and consist in total of:

- 2 pcs. of  $180^\circ$  turn
- 4 pcs. of  $90^\circ$  turn
- 6 pcs. of  $45^\circ$  turn
- 19 straight pcs.

On figure 3.7 is the top and bottom of a plate illustrated. For all routing is a Computerized Numerically Controlled (CNC) machine used, see BENI (2009) for details. The CNC has been chosen because the automation and precision are required so each plate type is produced equal. On the top side two slots 10.0 mm. apart have been routed. Copper tape has been fastened along each side of the slot to provide power to the car, and along the tape has the plates been painted with an extra hard paint to make the surface rough. This provides the possibility for higher acceleration and it minimise the probability that the car slide in the turns. On the bottom side of the plate, routing has been made to hold all the wiring apart from each other. Small holes (not visible on the figure) have been routed to fit the designed position sensors.

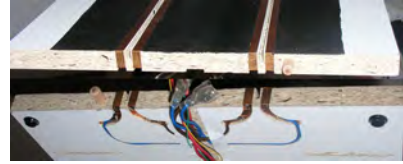


Figure 3.7: Top and bottom side of a plate.

The plates are assembled using two dowels to ensure that the slots are aligned correctly both horizontal and vertical and a clip is used to fasten the plates together in a firm inelastic way. This assembly ensures that the complete assembled track can be considered as one rigid system, see section 3.3.6 for the verification procedure.

All turn plates have been routed in a special way and by the same principle, see figure 3.8 for an example of the routed  $90^\circ$  turn plate. Along the curve, whether it is the inside or the outside, three different radiuses are used in order to make the entry and exit of the turn smooth and more coherent with the way actual roads are built. The green dots on the figure show the location of the position sensors.

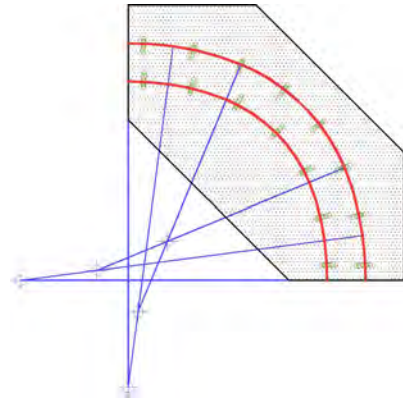


Figure 3.8: Schematic illustration of the entry and exit radiuses for the  $90^\circ$  turn plate.

### 3.3.1.2 The car

The main function of the car is to move the testing equipment around fixed to the reference geometry. The used car is a standard Ready-to-Run (RTR), slot car, see Parma PSE (2009) for details on the mechanics. Different motors, motor pinions and gearing can be adjusted in order to make the driving capabilities as desired for the test. For instance if the weight of the test equipment is high, can the gears be set so the car runs slower, but with a higher torque. On the other hand if the test equipment is lighter can the gearing and motor be adjusted to make the acceleration higher or to have a higher overall speed. An example of a fully equipped slot car is shown in figure 3.9.



Figure 3.9: The RTR slot car fully equipped with GNSS testing equipment.

The tap in the front of the car is sliding in the slot and the car can rotate around this point while moving along the track. The point will remain well known no matter how the car is rotating and is therefore defined as the horizontal reference point for the car. The standard chassis is slightly modified so a special produced mount can be fastened to it. The mount shall be constructed in such a way, that the GNSS antenna phase center are fixed above the horizontal reference point and thereby securing the vertical reference point.

There is no communication between the track and the car, nor can the power to the motor be used by the testing equipment. All components for the test equipment shall be fastened to the mount on the car including receiver, antenna, cables, storing capability and power supply.

The kinematic properties have been tested for a RTR car and are summarized in table 3.2. This has been done to indicate the influence of the total weight of the test equipment, and it can be seen that the values drop significantly for increasing weight. However these numbers are very dependent on the skills of the driver and the assembly of the tested geometry and would be very different for a car with adjusted gearing. A max. total weight of the car and testing equipment with the current available motors and gearing is

	Average [m/s]	Max. [m/s]
RTR car setup	2.9	6.8
Total weight of 800 g.	0.5	2.1

Table 3.2: Average and max. velocities of the car for two setups.

approximately 1.5 kg. The weight of a RTR car is 104 g.

### 3.3.1.3 The position sensors

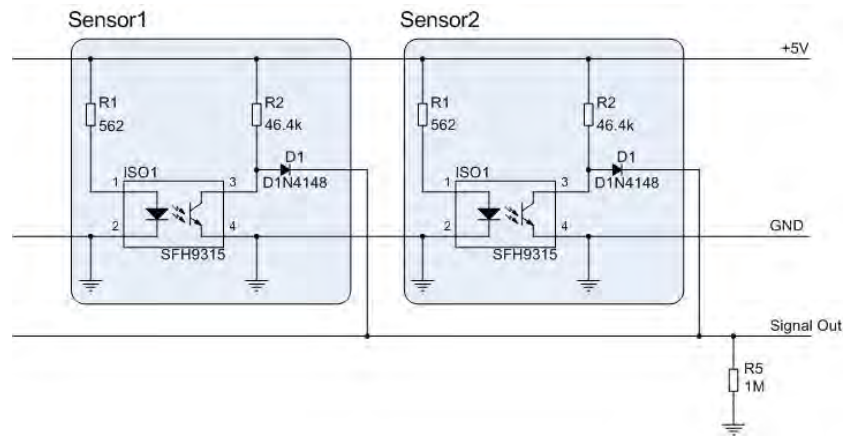


Figure 3.10: Electrical diagram of the position sensors implementation.

The main function of the position sensors is to send a signal to the microcontroller when a car passes it. A print of a position sensor is shown in figure 3.11 and these have been placed on each plate at known coordinates. The car detection principle is based on an opto coupler (the black unit on the board) which emits an infrared light beam between the two slides. When this beam is broken (when the tap on the car passes by) can it be detected.

The technical diagram of the implementation of two sensors are shown in figure 3.10, but the



Figure 3.11: Print of position sensor.



total number of sensors on a signal line can be numerous. Each sensor has three lines connected in serial, two for the power supply and one for the signal out. When the light from the diode in the opto coupler (SFH9315) reach the transistor the signal line will be low. When the light beam is broken the transistor pull the signal line up. The D1 diode is present to prevent the signals from other sensors to enter the sensor, but this also makes the null reference of the signal line to float and be sensitive to electromagnetic noise. The R5 resistor is therefore present to hold the null reference equal to the system null reference. In practice is the R5 placed in the microcontroller box.

2 types of signals (based on the same print) are used for each lane, resulting in 4 signal lines from the track to the control panel. These are a round signal and a pulse signal, and are used to distribute the logged time to the correct sensors, see section 3.3.3. There are several sensors, depending on the track assembly, on the pulse signal line, while there is only one sensor on the round signal line.

Sensors are placed with a separation of 20 cm. on straight plates and between 10 - 14 cm. on turn plates. For a car running with a velocity of 1 m/s, this results in a position sensor logging frequency of minimum 5 Hz.

#### **3.3.1.4 The motor control**

The function of the motor control is computerized control of the speed of the motor on the car. On a normal slot car track is the speed controlled manually with a hand speeder. The principle in that solution is a variable power resistor to consume all the effect, because a lot of current is needed for the motor operation. A digital potentiometer (same function as the power resistor) would be able to control the car from a serial link, but that would not be able to consume the effect. Digital motor controls, normally used in the robotic industry, would be able to control the car and consume the effect, but the output from this type of controllers is a Pulse Width Modulated (PWM) signal. This cannot be used on a slot car track with the current design as the pulses cause noise on the signal lines from the sensors. Instead a voltage regulated motor controller has been developed and implemented in the slot car track system. The electrical diagram is shown in figure 3.12.

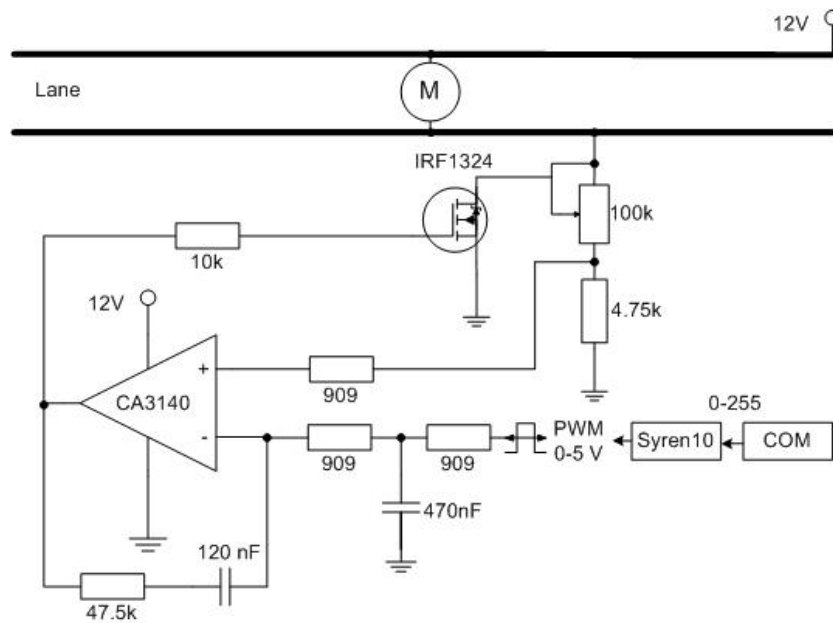


Figure 3.12: Electrical diagram of the motor control implementation.

The principle is to establish a serial connection to a Syren10<sup>1</sup>, which is capable of transforming a number between 0 and 255 to a PWM voltage between 0 and 5 V. This voltage is then low pass filtered and fed into an operation amplifier (OpAmp), the used type is CA3140. This open/close the current flow in the IRF1324 MOSFET until the voltage level of the + and - in the OpAmp is similar. When the PWM voltage is zero, will the MOSFET opens and the car will run fast and vice versa. The voltage regulator can be adjusted with the 100k $\Omega$  potentiometer to fit the linear level in the MOSFET. The speed can therefore be controlled from a serial communication port on a computer by adjusting a number between 0 and 255.

The actual implementation of the communication between the motor control and the logging software is performed on a wireless link using a set of telemetry modules, see Active Robots (2009) for detailed explanation of the product. The modules have been modified so the input power is 5 V. to make it fit into the overall system design. The modules have a maximum range of

<sup>1</sup>The syren10 is a regenerative motor driver controlled by a serial line, but is used with a low current in this implementation, see SyRen (2010) for specifications

250 m. and the communication is performed seamlessly, so the communication can be set up as if it was a normal RS232 cabled communication line.

### 3.3.1.5 The microcontroller

The functions of the microcontroller are to register the signals coming from the sensors and the external GNSS receiver and send information to the logging software for time synchronisation, see section 3.3.2. The microcontroller used is a PIC18F8490 from Microchip placed on a development board called PIC-LCD, see Olimex (2009) for further details. The microcontroller is fastened inside a box, shown in figure 3.13, which can be plugged into the control panel. The 4 signal lines from the position sensors and the PPS line from the external GNSS receiver are connected to 5 different ports in the microcontroller. The PPS line uses shielded wires, so this line is noise free. In order to detect the PPS pulses on this line the microcontroller interrupt routines are used. The internal oscillator in the microcontroller is used to time the incoming pulses and it has a time resolution of 0.03 ms. corresponding to 32768 oscillations per second. This resolution is considered to be sufficient. Each time a PPS from the external GNSS receiver is detected is the internal oscillator reset. When a signal is detected on one of the signal lines, the fractional part of a second can be stored and outputted to the logging software.

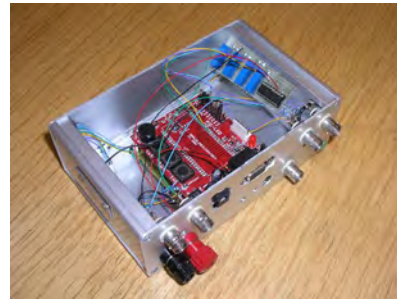


Figure 3.13: The microcontroller box.

Each signal line is held to ground by a resistor, see figure 3.10. Furthermore is each signal line connected to a voltage divider and an operational amplifier configured as a voltage follower in order to fit the required voltage level for the microcontroller and to keep the impedance low. The voltage divider is configurable by a potentiometer, because the level of the signal lines varies dependent on the length of the assembled track.

The detection of a signal has shown to be difficult as there is a lot of noise on the signal lines. The noise is present because of the implementation of the signal lines. They can be considered as a huge antenna picking up all kind

of electromagnetic noise. That is noise from the motor on the car, from the changing current flowing in the power supply to the car or as noise external to the system, for instance 50 Hz. noise. All this noise is different in shape, size and width. On figure 3.14 is a capture for a signal line illustrated. Between the pulses from the position sensors spikes can be observed. The magnitude can be greater than the pulse magnitude. False detections, leading to wrong identified position sensor, is critical to the slot car system performance, as a wrong distribution of timestamps to the sensors would lead to wrong coordinates of the car.

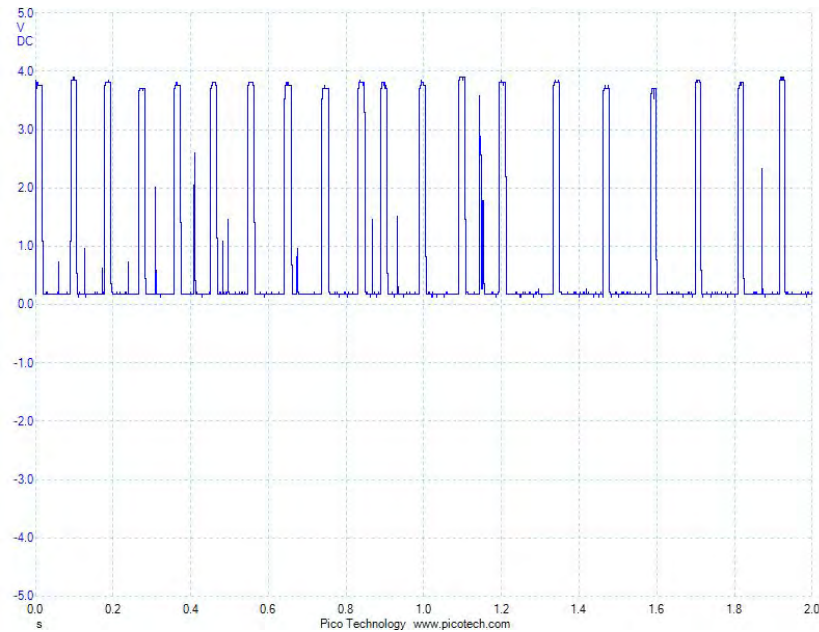


Figure 3.14: Illustration of noise spikes on a signal line.

To filter out the noise a hardware solution using a pulse shaper was implemented, see Jakobsen and Pedersen (2009), but this procedure was not optimal. Instead a software solution has been chosen. The 10 bit Analog to Digital Converter (ADC) on the microcontroller is multiplexing on the four signal lines with a speed corresponding to 10-15 samples per signal line for a 2 ms. pulse length. The length of a pulse with a car running with 10 m/s. These samples are analysed in real time to filter out the spikes and only detect the correct pulses. The varying number of samples is due to varying CPU processing time to send information to the logging software and time to process the PPS from the external GNSS receiver.

### 3.3.1.6 The control panel

The function of the control panel is to have one central place to switch on/off the different components as well as a central place to plug in the different external equipment. An illustration of the control panel is shown in figure 3.15. There are three sections: Two to control the inner and the outer lane and one for general components control. It is possible to switch on/off the external GNSS receiver, the microcontroller, each of the sensors on the 4 signal lines and the power supply for each of the lanes. Amperemeters are present to display the current flow on each lane as well as the overall current used by the sensors. In the bottom left side of the control panel is it possible to plug in the laptop running the logging software and the PPS from the external GNSS receiver. In the front bottom in the middle is the input power from the car battery. Fuses are placed inside on this line for safety reasons. It is also possible to divert the car direction on each lane separately, in order to have two cars going in the opposite direction if needed. The connection for all the wiring to the track is in the front middle of the panel, not visible on the figure.



Figure 3.15: The control panel.

Inside the panel is the motor control, the DC-DC converter and the microcontroller fastened as well as the different wiring between the track, the plug-ins and the components.

### 3.3.1.7 Power supply and DC-DC converter

The main function of these components is to ensure a stable and correct power supply for all the components in the system. A car battery has been chosen as the main power supply in order to sustain the portability property of the track, so it can be set up in environments without external power supply. Furthermore would it require an expensive 220 V based power supply as the operation of the car use a lot of current. The input voltage is thus 12 V. and it supplies all components directly or via the 12V - 5V DC-DC converter. The

components have been chosen so they run on either 12 or 5 V. The system has been designed to a maximum of 10 A at 12 V on each wire and a fuse has been placed at the incoming power supply for safety reasons.

#### **3.3.1.8 The external GNSS receiver**

The function of the external GNSS receiver is to send a Pulse Per Second (PPS) in the GPS time frame to the microcontroller and send the time information to the logging software. A Delta TRE.G3T Javad receiver with PPS output and an antenna placed with clear view to the sky has been chosen for this task. The phase jitter of the PPS is specified at 10 ns and even if the time was off by 1  $\mu s$ , this would correspond to 10  $\mu m$  travelled distance for a car running at 10 m/s. The synchronisation accuracy of the PPS to the GPS time frame is therefore considered sufficient for this task.

#### **3.3.1.9 Logging software**

The logging software has many functions listed below.

- Perform the time synchronisation of the signals from the position sensors to GPS time
- Continuously verify the time synchronisation
- Registration of time to each sensor pass
- Perform a check on correct number of sensors for each round pass
- Control the speed of each car
- Calculate local track coordinates for each sensor based on assembled plates
- Export the logged data for further analysis

The implementation of these functions is explained in the coming sections. In order to give the operator a better overview and control during the logging session have other features also been implemented. These include

- Display warnings to the user. For instance that the time synchronisation has failed or too many pulses have been detected per round

- Display of the current location of the car on a map in real time, so operation can be performed without looking at the track
- Display of real time velocity of each car
- Display a map of the current location of the position sensor, so it can be verified visually that it correspond to the assembled track.
- Blinking window, when a position sensor is triggered a window is blinking once. This is used to locate the exact location of the position sensor. For instance to place the car on the track in order to perform static measurements at the position coordinate.
- Simulation of input, this is used for debug and demonstration purposes. A PPS, a GGA NMEA string, and sensor pulses can be simulated.

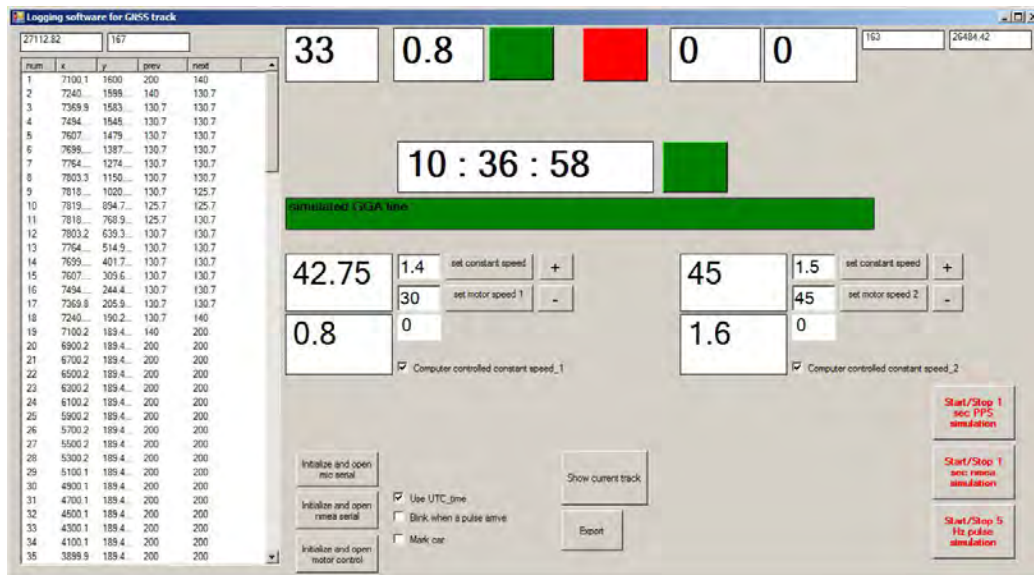


Figure 3.16: Main window for the logging software.

The software has been programmed in c# using the Object Oriented Analysis and Design (OOAD) approach and is available on request to the author. This implementation means for instance, that different tracks, lanes, plates, and position sensors are handled as objects. The result is an easy change of track assembly and the following local coordinate calculation of each position sensor is performed automatically during this procedure. An example of the main logging session window is illustrated in figure 3.16.

### 3.3.2 Time synchronization

The actual time synchronisation to the GPS time frame is performed in the logging software. The procedure is illustrated in figure 3.17. The input needed for this task is coming from the external GNSS receiver as well as the microcontroller. One input line from the microcontroller to the logging software consists of an ID and a number. The ID can have 5 different values:

- A PPS
- A pulse on lane 1
- A round on lane 1
- A pulse on lane 2
- A round on lane 3

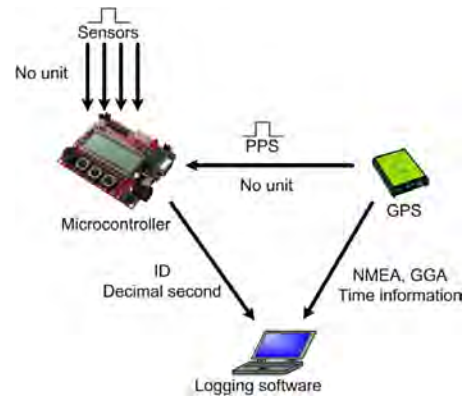


Figure 3.17: The time synchronisation procedure.

The numbers holds the integer value of the microcontroller oscillations. This fractional part of a second is transformed into decimal seconds by dividing it with 32768. For the PPS ID the number will be zero.

One input line from the external GNSS receiver to the logging software consists of a GGA line in the NMEA 0183 format outputted each second, see NMEA (2008) for a description of the format. This GGA line holds information of the GPS time, position, and fix and is always outputted after the PPS.

By using the incoming information can the integer second from the GGA line be assigned to each PPS from the microcontroller line. The decimal second can then be summed and the time synchronisation is complete.

Quality Control procedures have been implemented in the logging software to verify the GGA string, before the synchronisation. This includes, that the number of satellites are at least 6 and the quality indicator must show a fix. This is continuously verified by the logging software and an alarm is issued if the synchronisation for some reason fails.



### 3.3.3 Registration of time to a sensor

The individual pulse sensor cannot be identified when a pulse is detected in the microcontroller. All the pulse sensors are connected in serial, so the implementation can be considered as a giant OR gate. The round detector line with only one position sensor connected is used to keep track of the pulse sensors. The principle is illustrated in figure

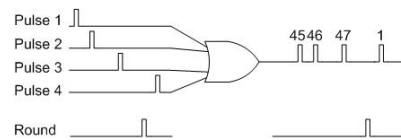


Figure 3.18: Round detection principle.

3.18. When a round is detected a counter is started to hold the number of pulse sensors and when the next round is detected the counter can be compared to the known number of pulse sensors, calculated by the logging software.

After a success the time information can be distributed to each pulse sensor and in case of a fail a warning is issued to the operator.

### 3.3.4 Computer controlled speed

A test can be designed in such a way, that the speed of each car need to be constant or varying by a certain specified manner for each round. The logging software is capable of controlling the car speed by adjusting the motor control. It is also capable of calculating the current speed of the car, because the time and distance between the last two passed sensors are tracked. An algorithm has been implemented in the logging software, currently working to hold a constant speed, by comparing the calculated speed with the wanted speed. Three intervals have been setup for the difference between those, that is if the difference is large, medium or little the motor control is adjusted accordingly, whether it is increasing or decreasing the speed. With this implementation is the speed of the car controlled within an interval of  $\pm 0.2$  m/s for a given constant speed in the interval of 0.6 to 1.8 m/s.

### 3.3.5 Exported data

The data from the logging software is exported in a comma separated file, where each line holds the following information:

- Lane identifier
- Sensor number
- Length to previous sensor [mm]
- Length to next sensor [mm]
- Passing time in the reference time frame
- Average speed for the last two sensors [m/s]
- x coordinate in the local track coordinate system
- y coordinate in the local track coordinate system

That is the data from both lanes are exported in the same file. Furthermore ensures the quality control procedures that rounds with incorrect number of sensors are filtered out. The exported information can be used in the further data analysis to resample the car coordinate, so the coordinate of the car can be calculated in any given instance of time during the entire test period.

### 3.3.6 Verification

The position sensors on each plate are placed at very precise plate coordinates. When the plates are assembled can the coordinate be calculated in a local track coordinate system if the track is considered as one big rigid system. This is in the ideal world not considering any small production errors or misalignment in the direction when two plates are assembled. A verification of this has been performed in Jakobsen and Pedersen (2009), where 15 sensors spread out on a 16.7 m. long track have been surveyed using a forward intersection method. A 5 parameter helmert transformation was performed to transform the surveyed coordinates into the local coordinates calculated by the logging software. The result was an average standard deviation of 1.14 mm. on horizontal coordinates and a scaling factor of 0.999672. It was therefore concluded, that the track can be considered as a rigid system no matter how the plates are assembled.

The output from the logging software is a timestamp for each sensor. In order to estimate the position of the car to any given instance of time must an interpolation between the sensors be performed. A verification of the interpolation procedure is illustrated in figure 3.19. The coordinate at any given length is connected mathematically, since the trajectory is known. Therefore can the interpolation be performed in the 1 dimensional length domain. A running window of 5 sequential timestamps is used, where the third observation is excluded and compared to an interpolated value based on the other 4

observations. The result of this analysis showed a standard deviation of 13.5 ms. The car was controlled manually at approximately 0.5 m/s during the verification, so this correspond to approximately 6.85 mm. This verification is performed on a length twice as big as the interpolation will be performed in the final test setup, and the accuracy of the interpolation will therefore be significant better. It is assumed, that the accuracy of the interpolation procedure will be better than 5 mm. in the final setup, when the speed is held constant. The interpolation routine is also very dependent on the acceleration/deceleration of the car and as the car was controlled manually, this had an impact on the interpolation results as well.

The overall functionality of the slot car track has also been verified in Jakobsen and Pedersen (2009). This was done by setting up the track on the roof of the National Survey and Cadastre in Denmark, where there was a clear view of the sky. A geodetic receiver was assembled on one car collecting data at a sampling rate of 10 Hz. A Precise Point Positioning (PPP)<sup>2</sup> solution and a Post Processed (PP)<sup>3</sup> kinematic solution to a nearby reference station was performed and compared to data collected from the logging software. The result showed, that systematic errors can be detected and that the design and implementation of all procedures of the slot car track was functioning.

It can therefore be concluded that the produced slot car track can be considered as an extension of the static domain (point) into the kinematic domain (reference geometry). The advantages from the tripod are sustained that is:

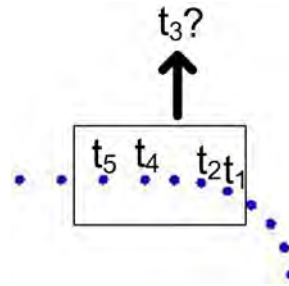


Figure 3.19: The procedure used for verification of the interpolation.

<sup>2</sup>PPP using GAPS ver. 3.4, Leandro and Langley (2007)

<sup>3</sup>PP using Trimble Total Control, ver. 2.73

- **Portability:** The track can be transported and set up in various scenarios, both indoor and outdoor
- **Multiplicity:** Two cars can be operated independent of each other at the same time
- **Flexibility:** The track can be assembled in various ways and each car can drive in both directions
- **Statistically:** The well known reference geometry makes a good foundation for statistics by repeating rounds

The kinematics of the car can be controlled, so the car is running with a constant velocity.

### 3.4 Tests and methodology

Tests have been performed in order to characterize the indoor multipath interference both under static and under kinematic conditions. These are described in the following sections.

#### 3.4.1 Scenario



(a) Looking South East



(b) Looking North East

Figure 3.20: Building used for the tests

The building chosen for the track setup is shown in the figures 3.20 (a) and (b). The approximate location of the reference station is indicated by the

red dot. The building is a wooden building with windows on the South and North side. The roof is based on a wood construction with roofing felt on top. Trees are present in the surroundings, which for some satellite passes also has an effect on the receiver signal power. The location of the reference station is chosen as the point with the best clear view of the sky near the building. A Delta TRE\_G3T Javad receiver, with a 5 Hz logging option, and a Novatel 702-GG antenna has been used for this task.

### 3.4.2 Testing equipment

Two evaluation kits (EVK-5T) from u-blox with a HS-GNSS receiver (LEA-5T) with firmware ver. 6.02 are used, see U-blox (2009) for a product description. This receiver is capable of outputting raw (L1 phase, C1 pseudorange, D1 Doppler, and S1 carrier to noise ratio) measurement with a sampling rate of 5 Hz.<sup>4</sup> The evaluation kit standard GNSS antenna is used, see U-blox (2003) for specifications.

The evaluation kit does not provide storage possibilities, so a wireless solution has been chosen to store the data on a laptop. This is based on the serial to wifi matchport module from lantronix, see Lantronix (2007) for the data sheet.

The different components have been modified in order to fit the mount on the car. The assembly for one of the cars is shown in figure 3.21. In front is the GNSS antenna placed, in the middle are the receiver and the battery and in the back is the wireless link.

### 3.4.3 Assembled track and surveying

The location of the assembled track in the chosen building, the reference station, and the points used in the survey procedure of the track, can be seen in figure 3.22 (a). The points Ref and 20 has been measured twice using an RTK rover with 2 hours in between in order to have independent measurements. The mean 3D coordinates have been stored in UTM zone

---

<sup>4</sup>The max. specified sampling rate is 2 Hz., but by eliminating several NMEA output sentences and disabling SBAS opens for 5 Hz. possibility.

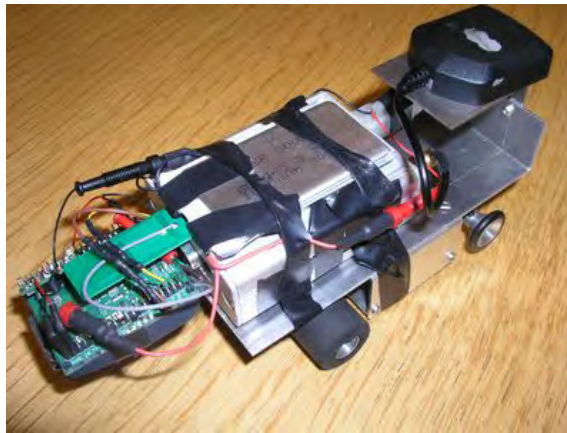


Figure 3.21: The assembled car.

33 WGS84 using the ellipsoidal height. All angles and distances between the points Ref, 20, and 30 have been measured with a total station and the horizontal distances have been reduced with the UTM scale factor. The coordinate of point 30 are then over determined. Distances and angles from point Ref and 30 to 5 selected sensors around the slot car track have then been measured, so their coordinates are over determined. These 5 points local track coordinates have then been used to calculate a 7 parameters Helmert transformation. And these parameters have then been used to transform any given local track coordinate to UTM 33 WGS84. The transformation to ECEF coordinates is performed using standard geodetic transformation routines, see for instance Wasmeier (2010).

Calculating a distance using the RTK surveyed coordinates for point Ref and 20 and comparing this to the measured distances with the total station would indicate an error in the RTK survey. The result was 1 mm. As the 5 chosen sensor coordinates close within 1 mm. and the helmert transformation showed a deviation of max. 5 mm. can it be concluded that the track is well oriented in the ECEF coordinate system with accuracy below 1 cm. The absolute coordinate of the car can then be determined for any given instance of time better than 1.5 cm., which is considered sufficient for the desired test.

The complete assembled track inside the building can be seen in figure 3.23 (a). The track is lifted up from the ground and placed on a set of tables in order to provide an environment corresponding to a person walking around

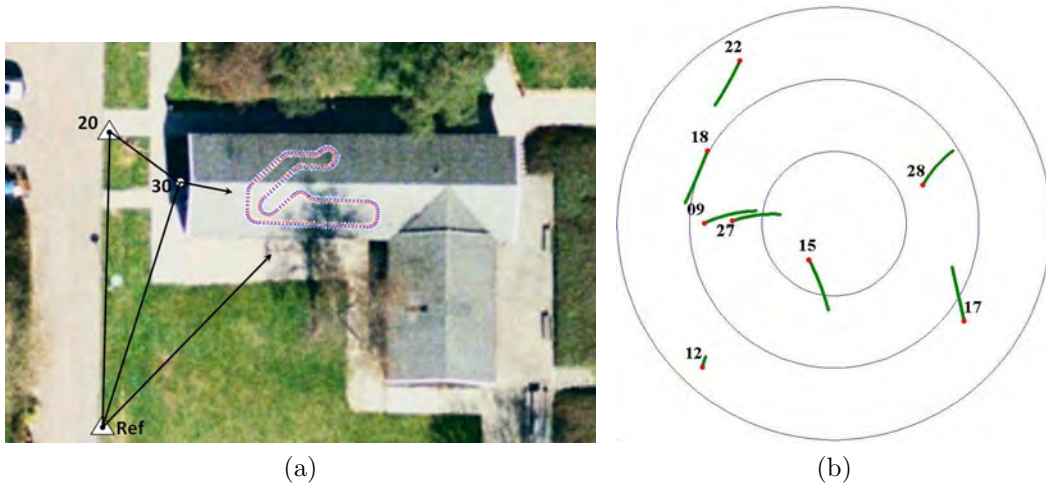


Figure 3.22: (a) The location of the assembled track, the reference station, and the survey points. (b) Skyplot for the visible considered satellites during the test period. The red dot indicates first visible location.

with a receiver, as well as to increase the reflections from the ground. The trajectory has been chosen to represent a curve with different turns and straight sections close to the windows as well as in the center of the room. The length of the complete assembled track is 27.112 m. for the outer lane and 26.484 m. for the inner. The integer meter values are indicated in figure 3.23 (b).

#### 3.4.4 Data collection flow and methodology

An illustration of the data flow during the collection phase is illustrated in figure 3.24.

Data are collected from three types of equipment. The slot car track data are saved in real time via the logging software to a csv-file. This file is afterwards post processed in matlab with an ECEF coordinate for every 5 Hz. in the GPS time domain as the result. The interpolation of the slot car data are performed using a linear method along the length of the trajectory. This is considered sufficient as the speed is almost constant around the track.

The testing equipment (HS u-blox receiver) data are logged wireless via the U-center software and saved in the u-blox raw format. The reference equip-

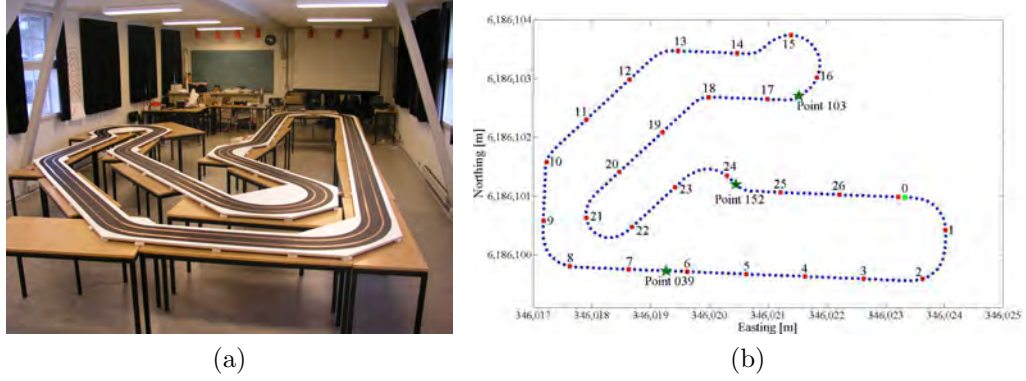


Figure 3.23: The assembled track inside the building, length [m] for the outer lane indicated by the red dots, and location of the static points indicated by the green stars.

ment data are stored in the javad raw format on the receiver. The GPS raw data are translated to the Rinex format using the TEQC program, see UNAVCO (2010), and afterwards to a csv-file using the GPSTk software, see Tolman et al (2004). The three types of csv-files have then been analysed using matlab.

Two similar sets of test equipment, one in each lane, have been used simultaneously. The cars have been controlled with constant speeds for 4-8 rounds. Starting with 0.6 m/s and ending with 1.8 m/s in intervals of 0.2 m/s. Furthermore has three points been selected around the track and used for static measurements for approximately 7-8 minutes per point. The location of these points is shown in figure 3.23 (b).

The logged  $C/N_0$  values at the reference station correspond to a LOS signal. Subtracting this value from the  $C/N_0$  logged indoor will then correspond to the overall attenuated power level caused by the surroundings and the building. That is both the shadowing effects caused by refraction and the constructive and destructive interference mentioned in section 3.1.1. The fading,  $F$ , can then be defined as in equation 3.2.

$$F = C/N_0^{Ref} - C/N_0^{rover} \quad (3.2)$$

In general is the fading expected to be positive because the signal strength observed under a clear view to the sky should be no less than signals in



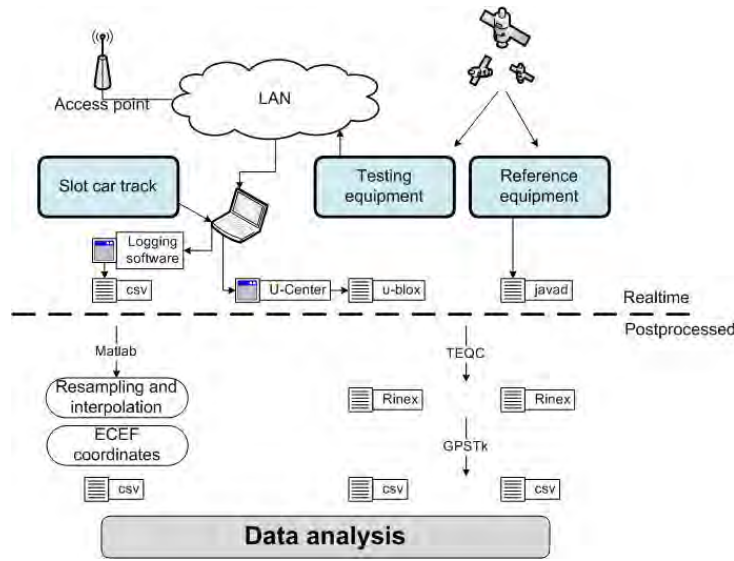


Figure 3.24: The data flow during the collection phase.

degraded environments. However, if the signal of one satellite has destructive multipath interference at the reference receiver while the signal of the same satellite has constructive multipath interference and a little shadowing effect at the rover, the observed  $C/N_0$  at the rover may be larger than observed at the reference station. The result is a negative fading and is, when observed, mainly for low elevation satellites.

The  $C/N_0$  measurement is dependent on the processing technique of the receiver, which means that the fading in an absolute sense requires the same receiver types and antennas with similar antenna gain patterns at the reference point as well as the rover. However, as this is not the case for this experiment, will the fading values also include the difference between the receiver and antenna used for the reference and rover. The values of the fading differenced with respect to time will, however, not be influenced.

An analysis of the accuracy in the positioning domain is also performed. The software package GPSTk has been used for this, see Tolman et al (2004). The algorithm used is an autonomous pseudorange solution based on an epoch by epoch Weighted Least Square algorithm. The output is not affected by any Kalman filtering and is therefore suitable for comparing the difference in positions from epoch to epoch caused by the changing multipath interference.

This is primarily obtained as specific unique satellites are used for each epoch.

## 3.5 Results

### 3.5.1 Static characteristics

The characteristics of the static measurements under indoor conditions have been investigated using three selected points at different locations in the room. These are illustrated in figure 3.23 (b). The influence of multipath for the point 103 is illustrated in the figures 3.25, 3.26, and 3.27. These graphs are produced by filtering the dataset to only include 7 specific SVs per position calculation. This way will the change in DOP values be neglectable from one epoch to another as illustrated in figure 3.25 (a). The change from one epoch to the next will therefore show the effect from the changing multipath rather than change in satellites used in the position solution. The latter can have significant impact on the position solution, especially when a lot of multipath delay is present.

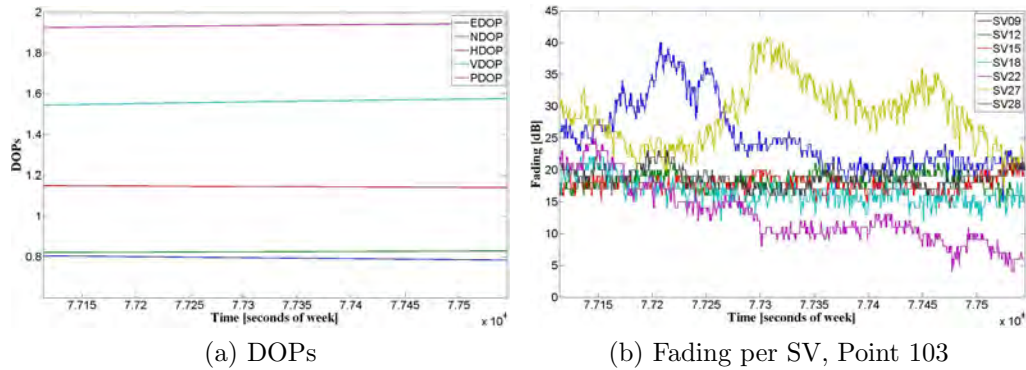


Figure 3.25: The DOPs and fading values per SV in a time window of 7 minutes and 10 seconds.

The fading effects on the SVs through the measurements period show similar characteristics, see figure 3.25 (b). The curves are very smooth with changes of fading values per SV in the order of 0-2 dB in general and the size of the fadings is in general 15-20 dB. SV 22, which is a low elevation satellite penetrating through a wall with windows, shows the smallest values. SV 09

and SV 27 show large fading values reaching up to 40 dB at certain times during the time window. These two satellites, at app.  $55^\circ$  and  $65^\circ$  elevation, see figure 3.22 (b), are penetrating the roof and is expected to have larger fading values. SV 15 and 28 are also penetrating the roof, but are not faded in the same manner, a difference that must be explained by the roof pitch.

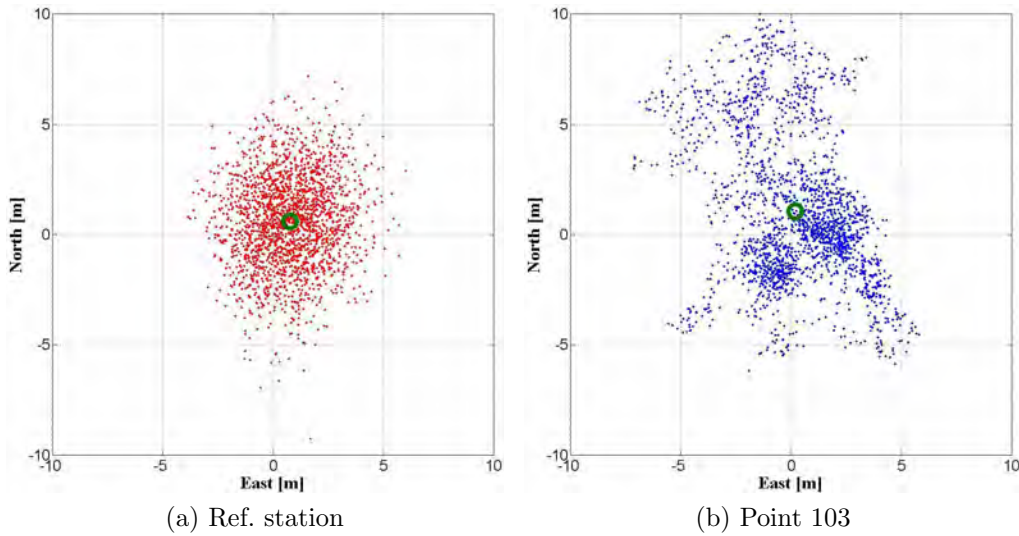


Figure 3.26: Static influence of multipath, shown as horizontal position differences, in a time window of 7 minutes and 10 seconds. The green circle refers to the mean value and zero refers to the true value.

In figure 3.26 (a) and (b) is the position solution illustrated and show the difference in the positions caused by the change in environment. The change in positions for the reference station is high frequent and show normal distribution characteristics. The positions for the indoor point tend to congregate and the change from one epoch to the other is small. In table 3.3 is the standard deviation for the two cases listed. The standard deviation for the indoor point is app. 1.5 times larger than outside, but the mean value for the two datasets are almost the same and within 1 m. from the true coordinate.

The height difference between the two points, illustrated in figure 3.27 (a) and (b), show almost the same characteristics. The calculated heights for the reference station is high frequent, while the heights for the indoor point are more moderate in variation. But the mean value is significant lower for the indoor point, which can be interpreted as the effect from multipath is absorbed in the horizontal plane, the satellites are distributed more evenly

	Ref. station		Point 103		Point 039		Point 152	
	Offset	Std.	Offset	Std.	Offset	Std.	Offset	Std.
North	0.59	2.05	1.05	3.41	1.05	3.42	-29.91	20.01
East	0.76	1.58	0.18	2.32	0.23	2.14	-2.37	7.85
Hor.	0.96	2.59	1.06	4.12	1.08	4.03	30.00	21.50
Height	1.25	2.81	-4.69	5.11	-0.10	5.68	-73.22	50.62

Table 3.3: Offsets and standard deviations (mean value) for the four points in the static analysis. All units are in [m].

on a skyplot. While a longer distance on each pseudorange will contribute to a lower value in the height domain. The change in height for the indoor point is not correlated with the change in fading values for the considered satellites. For instance do the low values for the height at approximately 77380 seconds show no similar fading effects.

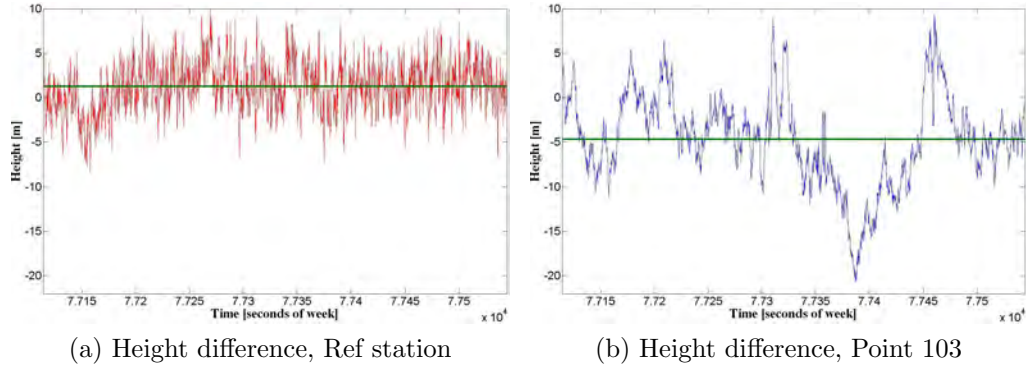
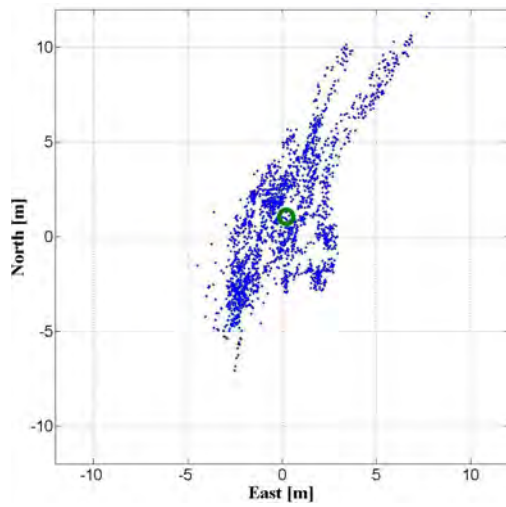
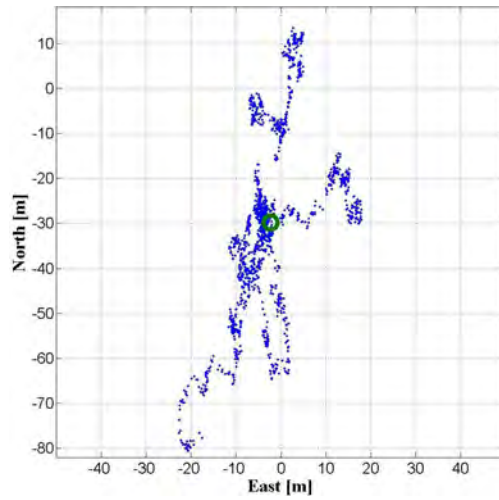


Figure 3.27: Static influence of multipath in a time window of 7 minutes and 10 seconds. The green graphs refer to the mean value and zero refers to the true value.

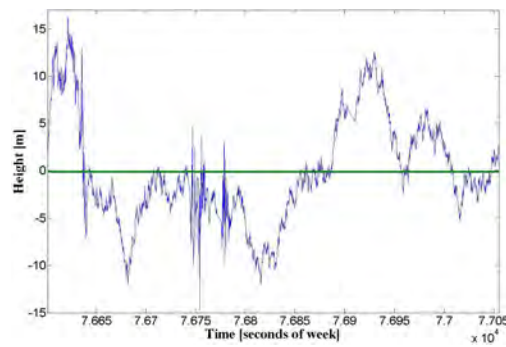
In figure 3.28 (a) to (f) is the position solution for the point 039 and 152 along with the corresponding fading effects for the considered satellites illustrated. The positions for point 039 are based on 6 satellites, while the positions for point 152 are based on 5 satellites, and the corresponding statistics is listed in table 3.3. The specific SVs are chosen, so the SVs with most observations for the test period are chosen. The data collection for the two datasets is not performed on exactly the same time, but based on two 7-8 minutes following periods. The used equipment for the two datasets is the same.



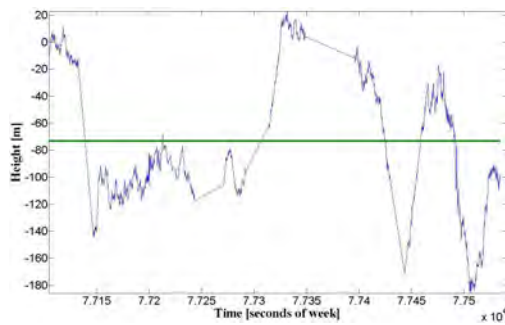
(a) Horizontal position difference, point 039



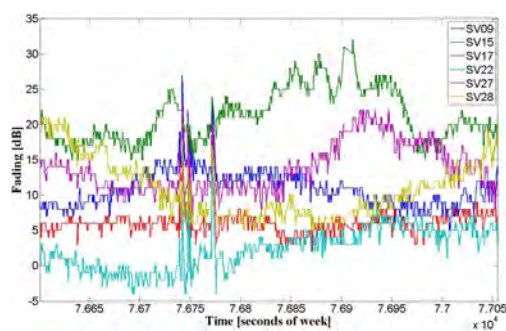
(b) Horizontal position difference, point 152



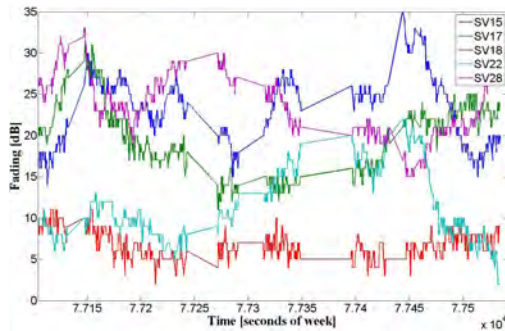
(c) Height difference, point 039



(d) Height difference, point 152



(e) Fading per SV, point 039



(f) Fading per SV, point 152

Figure 3.28: Static influence of multipath in point 039 and 152. The time window for point 039 is 7 minutes and 34 seconds and the number of satellites is 6, while the time window is 7 minutes and 10 seconds with 5 included satellites for point 152. The green graphs in figure (a) to (d) refer to the mean value and zero refers to the true value.

For the point 039 are the standard deviations and offsets very similar to the values obtained in point 103 except for the height component. This can be explained as the pseudorange error for the high elevation satellites are penetrating the roof differently for the point 039 in the southern part of the room, than for the point placed in the northern part of the room. The large fading values observed at time at approximately 76750 seconds, with corresponding effects on the height measurements. These variations must refer to receiver specific conditions and not related to the environments as they are observed for all the considered satellites at the same time.

The number of satellites included in the positioning solution can have significant influence on the accuracy, especially in a high multipath interference environment. In many real time situations it is not possible to acquire more than 4-5 satellites if possible at all. The dataset for point 152, placed in the middle of the building, includes 5 satellites, and is a good example of this. The remaining satellites have been omitted for this analysis, but they have been tracked by the receiver. Epochs where one or more of the considered satellites are not tracked has been filtered out. The standard deviation for the north-south component is approximately 2.5 times larger than the east-west component, which deviates from the trend observed for the other two points. It shall be mentioned that the offset is relatively close to zero for the east west component, while it is at -29.91m. for the south-north direction and at -73.22 for the height component. This is probably caused by the satellite constellation, as there are no satellites for low elevations from the south. The large positive pseudorange errors, assumed to be present for the considered satellites, will be weighted higher for a limited number of satellites.

### 3.5.2 Kinematic characteristics

The kinematic characteristics under indoor conditions have been investigated using the slot car track. In figure 3.29 (a) to (d) is the fading for two satellites illustrated both as function of length and distribution in the horizontal plane. The two considered satellites is a low elevation, penetrating through the windows and the wall (number 22), and a high elevation, penetrating through the roof (number 15), see figure 3.22 (b). In total 7 rounds within 117.8 seconds was driven with an average speed of 1.6 m/s.



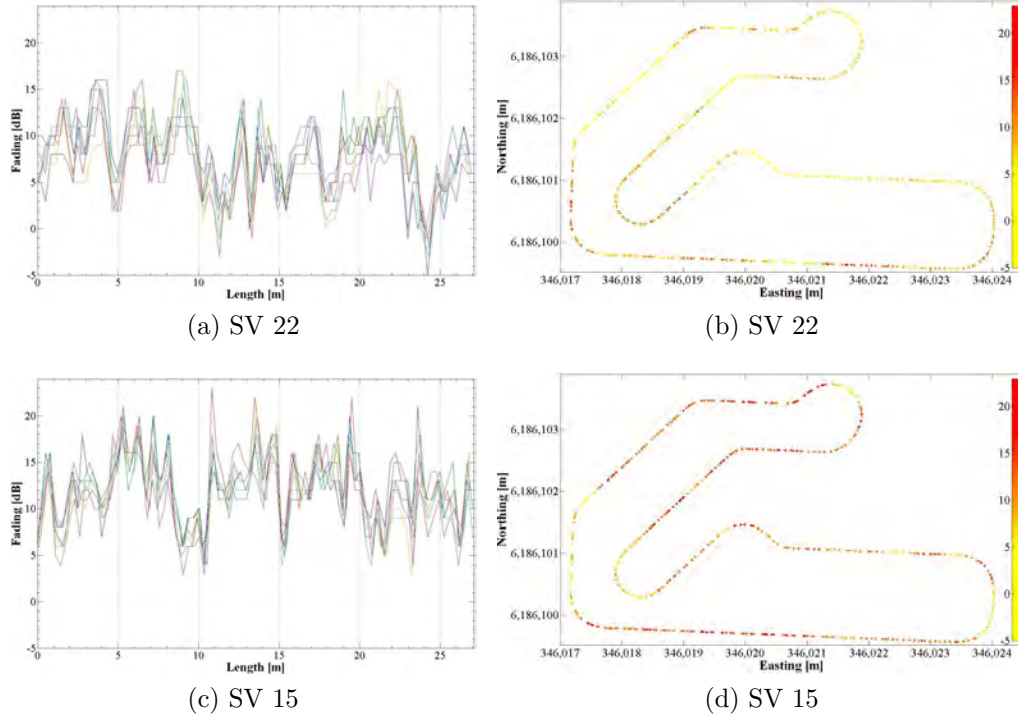


Figure 3.29: Length and horizontal distribution of fading [dB] for two selected SV for 7 rounds at speed 1.6 m/s for the outer lane.

The curve for the two considered satellites shows similar behaviour. The fluctuations of the fading are significant higher than in the static case, which is caused by the rapid change in the multipath interference as the car drives around in the building. The fading pattern for each round show large correlation that is the fluctuations happen at the same positions for each round. This means, that the multipath interference is similar for repeating rounds with the same kinematic behaviour within a limited period of time.

The pattern and the sizes of the fading are not similar for the two satellites as expected. SV 22 has in general the smallest fading values, as these signals are penetrating through the windows and the relatively thin walls. However there is no clear indication, that signals with a LOS through the windows are faded less than the walls. The large sections with small values are after 11 and 24 m, which is in the north east part and in the middle of the room, see figure 3.23 (b). If this should be correlated with the windows, then should the values be lower going in a south-east direction. In fact there is no clear indication

of effects correlated with the direction of the LOS. A cyclic behaviour can be observed from 2-8 m, which is the 6m straight line in the south of the room.

For SV 15 is a slightly more cyclic behaviour observed, especially at the 6m straight line in the south of the room. This can be explained with the change in materials as rafters are present as part of the building construction. But this behaviour cannot be clearly observed other places on the route. Significant and very correlated changes in the fading values are observed along the track. For instance after 10.5m, see figure 3.23 (b), where the fading is going from the lowest level at 8 dB to the highest level at 22 dB for one of the rounds, but also at 15 m, where the values are suddenly low. The latter is at a location with general high values. There are no visible materials in the LOS direction that can explain this behaviour.

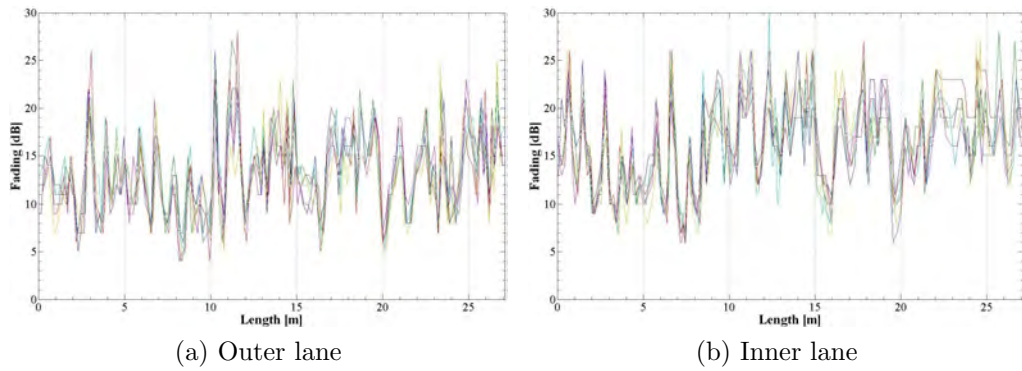


Figure 3.30: Fading for SV 15 for two lanes for 6 rounds with speed at 1.0 m/s. The length for the inner lane has been scaled to fit the length of the outer lane.

In figure 3.30 is the fading illustrated for SV 15 for both lanes as function of the length and in figure 3.31 is the same fading shown in the horizontal plane. 6 rounds have been driven for each lane with an average speed of 1.0 m/s. Each lane show the same correlation between rounds as was found previous, but the two lanes do not correlate all over the track. On the straight section in the south of the room, there is clear correlation with cyclic fading effects along the track. The steep high fading effect after 10.5m is also present for the outer lane as was the case for the previous figure, but is non existent for the inner lane. And the curve at 15-16.6m, show little fading for the outer lane as was also the case in the previous figure, while part of the curve is significantly faded for the inner lane. The multipath interference is therefore



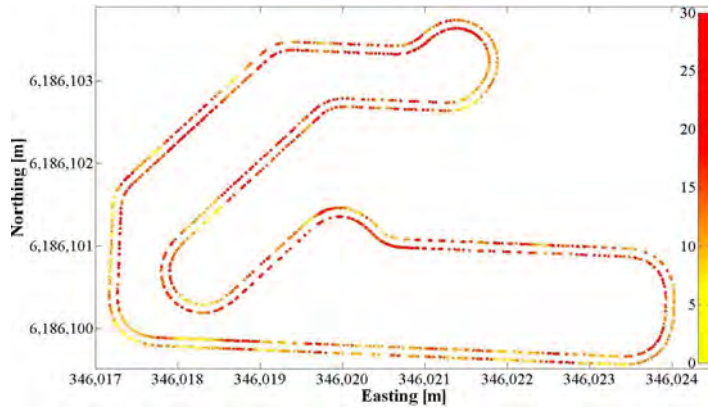


Figure 3.31: Horizontal distribution of fading for SV 15 for two lanes for 6 rounds with speed at 1.0 m/s.

very dependent on the location while even a similar curve only 10 cm. away shows decorrelation various places.

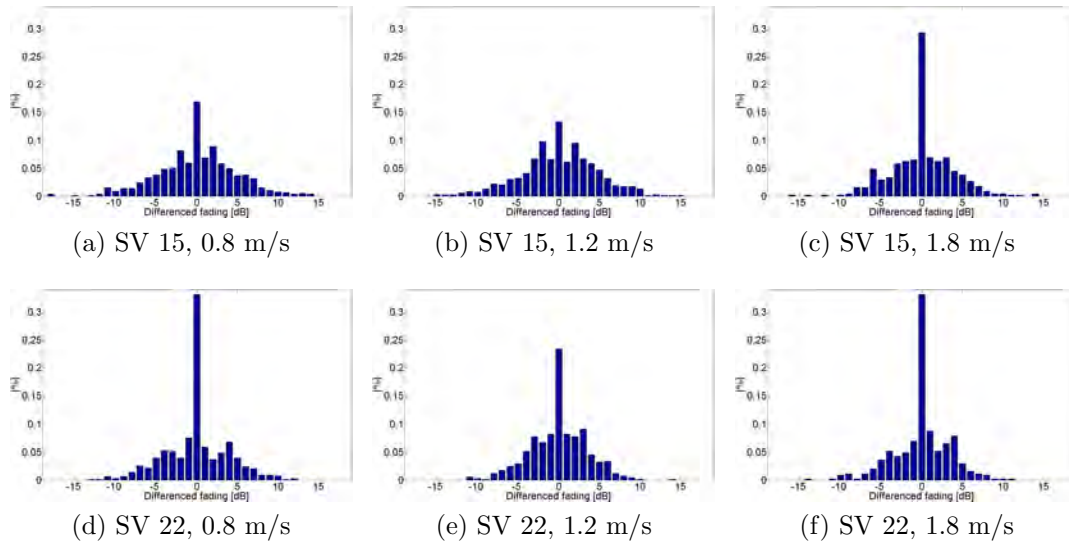


Figure 3.32: Histogram of differenced fading values for two selected satellites and three selected speeds.

In figure 3.32 (a) to (f) is histograms for fading values differenced with respect to time illustrated for satellite 15 and 22 for the speeds 0.8, 1.2, and 1.8 m/s. It can be seen, that the high elevation SV 15 in general has higher differenced values than the low elevation SV 22. A dependency on the speed can also be observed. Low and high speed has many following epochs, where the fading

values do not change, and at the same time are the largest differenced values for these two speeds.

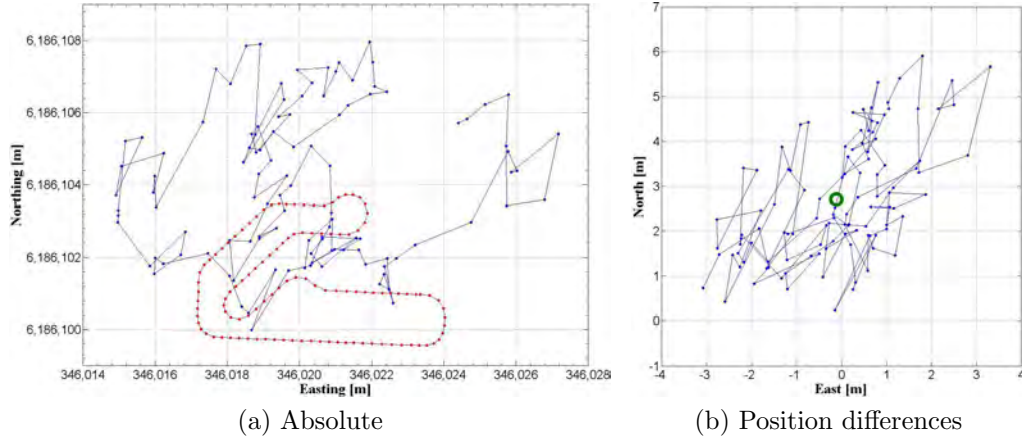


Figure 3.33: Example of horizontal distribution of positions for the outer lane for round number 4 for speed 1.2 m/s. The red dots correspond to the true values.

In figure 3.33 is an example of the horizontal distribution of positions for the outer lane for round number 4 with speed of 1.2 m/s illustrated. All the positions are based on the same 6 satellites as was used for the static point 039 in order to show the effect of the multipath interference under kinematic conditions along the track. On the absolute plot is the trajectory for the round presented, and it can be seen, that the shape of the positions deviates from the shape of the true trajectory. On the position difference plot is shown the same dataset, but with the true position subtracted for each epoch. The positions show a high variation from one epoch to another, compared to the static case. This is expected, as the multipath interference observed for the fadings for each satellite also is high frequent. The tendency, where the positions group for the static case, is non existent in the kinematic domain. Even though there is correlation between the fadings for each round and for each satellite, there is no correlation between rounds in the positioning domain. Different shapes of the trajectory are present for repeated rounds.

In figure 3.34 is the corresponding height differences plotted. A spike can be observed at approximately 75439 seconds that last one second. These spikes are frequently observed in the height domain and can reach up to 30m, where the same 6 satellites are sustained. There is also no correlation

Speed [m/s]		0.6	0.8	1.0	1.2	1.4	1.6	1.8
Offset [m]	East	-0.61	0.25	0.21	-0.44	-0.51	-0.53	-1.28
	North	5.64	2.91	2.73	2.17	1.83	0.89	0.64
	Hor.	5.67	2.92	2.74	2.21	1.90	1.04	1.43
	Height	4.63	1.18	1.30	0.51	0.45	-0.48	-0.96
Std [m]	East	2.55	1.59	1.21	1.28	1.23	1.21	2.39
	North	4.90	3.28	2.35	1.82	1.91	1.82	3.20
	Hor.	5.52	3.64	2.64	2.23	2.27	2.18	3.99
	Height	5.45	4.85	4.11	3.03	2.94	3.82	5.58

Table 3.4: Offsets and standard deviations (mean value) for the position differences. The dataset is for the outer lane.

between rounds in the height domain, nor is there any correlation for the spikes.

In table 3.4 is the offsets and standard deviations for the position differences listed. The dataset include all rounds at each speed. The offsets for the east component show practically no dependency on the speed, while the north and height component show a decreasing tendency for higher speed. The standard deviations for the east component is a little higher for speed 0.6 and 1.8 m/s and the north component show also a decreasing value for higher speeds.

An exception is the 1.8 m/s, where the values increase. The same pattern is seen for the height component, but the increase is observed already at 1.6 m/s.

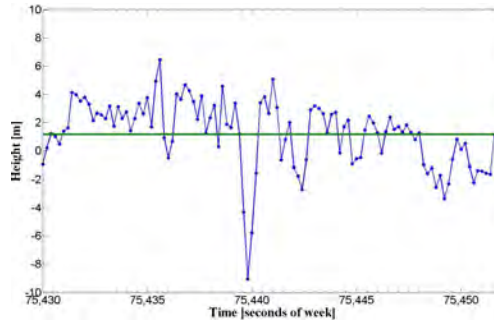


Figure 3.34: Example of height measurement for the dataset in figure 3.33.

The size of the standard deviation values are in many cases smaller than for the indoor static points, but the data set for the static case cover a longer time period.

### 3.6 Conclusion on characteristics of multipath

The characteristics of indoor multipath are very difficult to model. The majority of satellite signals arriving at the antenna front end rarely follow a LOS path and suffer from attenuated power as well as a time delay that affect the correlation peak in the GNSS receiver.

A wooden building with windows on the north and south side has been used to characterise the fading and positioning effects caused by the building and surroundings both using a static receiver, but also under controlled kinematic behaviour. Data has been collected at a sampling rate of 5 Hz with a HS GNSS receiver.

In order to control the kinematics of the receiver has a slot car track been built and the functionality been verified. The track sustains the properties from static measurements. It is flexible, it can be assembled in various ways to form a desired reference geometry. It is portable, it can be set up in various environments both indoor and outdoor. Multiple use, two cars can be used at the same time, and the Statistical property is sustained by repeating rounds.

Furthermore can the slot car track system control the speed of the car and an algorithm has been implemented to keep the speed constant. This can be achieved in the interval of 0.6 - 1.8 m/s within the interval of  $\pm 0.2$  m/s. The position of the car is given to any given instance of time with an absolute accuracy less than 10 mm.

The characteristics under static conditions show that the change of the fading values from one epoch to the other are in the order of 0-2 dB, but the difference between high and low values within 7 minutes of tracking can be as high as 20-25 dB. Overall are the fading values at 15-20 dB. Higher fading values are seen for a high elevation satellite penetrating through the roof, than for a low elevation satellite penetrating through the wall and windows.

Indoor positions compared to positions calculated in a clear view of the sky environment show a tendency to congregate and the standard deviations is 1.5 time larger in the horizontal plane. The height component can be more affected than the horizontal positions when more than 6 SVs is used in the position calculation. The number of satellites has a significant influence in the

positioning domain, especially for 5 SVs or less. Even though the DOP values are low have large position errors been observed with standard deviations of 21.50 m. and 50.62 m. in the horizontal plane and height component respectively.

The fading values under kinematic conditions differ a lot compared to the static case as they fluctuate more. Approximately 90% of the differenced values are in the interval of 0-5 dB and differenced values of up to 19 dB are observed. A tendency show, that the percentage of epochs with 0 dB change is higher for speeds at 0.8 and 1.8 m/s than for 1.2 m/s. This is consisting for all observed satellites for all speeds at both lanes.

The fading values for each satellite show a high correlation for each round for all considered speeds and for both lanes. Correlation between two lanes separated by 10 cm. show clear correlation at some locations in the building, and clear decorrelation other places. In general the fading pattern along the track cannot be clearly related to the building materials.

The trajectory for the calculated positions is uncorrelated for each round, even though the multipath interference observed in the fading values show clear correlation. The trajectories geometry follows in general not the true geometry, which can be seen in the position differences. These are high frequent, as the environment change frequent along the track.

A trend with decreasing standard deviations is observed for increasing speeds from 0.6 - 1.6 m/s. from 5.52m to 2.18m in the horizontal plane with a standard deviation of 3.99m for the speed 1.8 m/s.



## Chapter 4

# Conclusion and perspectives

The variation of the ionosphere has a great impact on many GNSS related applications. For single frequency code users will the impact be largest when the activity starts to rise in the coming years towards the next solar maximum. Better understanding of the time varying parameters will lead to better estimation or prediction into future epochs. Implementing the method for extracting the TEC by using GNSS receivers into a real time space weather service and at the same time combine it with geomagnetic observation also open for a better estimation or detection of abnormalities in the TEC variation.

The observed variation of the ionospheric modelling error in a NRTK service can be of importance. The end user may use the knowledge to better optimise the measurements campaign. For instance can he/she in some cases raise the elevation mask. The increased elevation mask will in general give higher DOP values, but it will also remove the increased noise on the pseudorange. In case of tasks, where the best possible accuracy is needed, the end user shall perform his/her measurements during the evening or early morning. The end user can also use the information to have a better foundation to choose which NRTK service he/she fits his/her needs.

The NRTK service provider can use this information when designing or redesigning existing NRTK services. The station separation shall be considered and carefully optimized in order not to degrade the position accuracy too much. Not only the overall station separation, but the data lines in the system might fail causing a station to fall out for a limited period of time.

The station separation will in these cases be much larger, and warnings can be sent to the end users in case of expected performance problems. In cases where the fall out station is a boundary station the modelling error may increase significantly as certain areas of the NRTK service coverage area will now be in the extrapolation area.

In order to better understand the performance of the NRTK service ionospheric modelling, more campaigns are needed. These shall consist of 24 hour data files performed on different times of the year. But campaigns are also needed on a yearly basis, at least up to the next solar maximum. Special interest will be the influence when significant more ionosphere activity is present. The new NRTK service evaluation method provides the possibility for this. It also provides the possibility to look at other observations in order to evaluate other areas of the NRTK performance. This could for instance be the troposphere modelling, but the possibility to evaluate the assumed less cycle slips could be interesting.

The developed slot car track opens for a variety of other tests than determining the characteristics of multipath under kinematic conditions. In general all known GNSS tests or methods, where the position of the antenna shall be known with an absolute accuracy of less than a cm, can be extended and tested in the kinematic domain as the slot car track provides the absolute position for any given instance in time. The tests are not limited to the use of GNSS receivers though. In fact any test, where the location of the car at any given instance of time is needed, could be performed. This could be different kind of mapping data along a track for instance how temperature change inside a room when the sun rise and starts warming up the air.

The multipath characteristics found in this thesis do not cover the complete subject. Further tests are needed in order to fully understand the multipath interference under kinematic conditions. But the tests have revealed new possibilities or focus areas to gain more knowledge of the multipath interference under kinematic conditions. This includes tests performed over long time interval in order to track complete satellite passes and determine any elevation dependencies, tests performed with different kind of accelerations, and tests performed in a predetermined environment setup. Furthermore would an extension of the existing analysis to also include estimated pseudorange errors be valuable.



# Bibliography

- Active Robots (2009) RF telemetry data module. <http://www.active-robots.com/products/radio-solutions/miniature-radio.shtml>
- Anderson E, Bai Z, Bischof C, Blackford S, Demmel J, Dongarra J, Croz JD, Greenbaum A, Hammarling S, A McKenney DS (1999) LAPACK Users Guide, 3rd edn. Society for Industrial and Applied Mathematics
- Basu S, MacKenzie E, Basu S (1988) Ionospheric constraints on vhf/uhf communications links during solar maximum and minimum periods. *Radio Sci* 23(3):363–378, URL <http://dx.doi.org/10.1029/RS023i003p00363>
- BENI (2009) CNC router details, BENI furniture and design. <http://www.beni.dk/Eng/mask0.html>
- Bidaine B, Warnant R (2010) Assessment of the nequick model at mid-latitudes using gnss tec and ionosonde data. *Advances in Space Research* 45(9):1122 – 1128, DOI DOI:10.1016/j.asr.2009.10.010, URL <http://www.sciencedirect.com/science/article/B6V3S-4XH5MP7-2/2/996f05413632a606bd9ddc0e7a6884a5>, special Issue: Recent Advances in Space Weather Monitoring, Modelling, and Forecasting
- Borio D, Lachapelle G (2009) A non-coherent architecture for gnss digital tracking loops. *Annals of Telecommunications* 64:601–614, URL <http://dx.doi.org/10.1007/s12243-009-0114-1>, 10.1007/s12243-009-0114-1
- Budden KG (1985) The propagation of radio waves : The theory of radio waves of low power in the ionosphere and magnetosphere. Cambridge (Cambridgeshire); New York : Cambridge University Press, DOI ISBN0-521-25461-2

- Conker RS, El-Hrini MB, Hegarty CJ, Hsiao TY (2000) Modeling the effects of ionospheric scintillation on gps/sbas availability. MITRE, Center for Advanced Aviation System Development
- Conker RS, El-Hrini MB, Hegarty CJ, Hsiao T (2003) Modeling the effects of ionospheric scintillation on gps/satellite-based augmentation system availability. *Radio Science* 38(1), DOI 10.1029/2000RS002604
- van Diggelen DF (2001) Global locate indoor GPS chipset and services. Institute of Navigation, ION GPS pp 1515–1521
- Feng Y (2008) Gnss three carrier ambiguity resolution using ionosphere-reduced virtual signals. *Journal of Geodesy* 82:847–862
- H-Euler, Keenan CR, Zebhauser BE, Wbbena G (2001) Study of a simplified approach in utilizing information from permanent reference station arrays. Proceedings of the 14th International Technical Meeting of the Satellite Division of The Institute of Navigation ION GPS, Salt Lake City, Utah pp 379–391
- Hartmann G, Leitinger R (1984) Range errors due to ionospheric and tropospheric effects for signal frequencies above 100 mhz. *Journal of Geodesy* 58(2):109–136, URL <http://dx.doi.org/10.1007/BF02520897>
- Hathaway DH (2010) The national aeronautics and space administration. Website, [http://solarscience.msfc.nasa.gov/images/Zurich\\_Color\\_Small.jpg](http://solarscience.msfc.nasa.gov/images/Zurich_Color_Small.jpg)
- Hegarty CJ (1997) Analytical derivation of maximum tolerable in-band interference levels for aviation applications of gnss. *Navigation* 44
- Hu T (2006) Controlled indoor GPS signal simulation. PhD thesis, Department of Geomatics Engineering, Schulich School of Engineering, University of Calgary, UCGE Report no. 20235
- Huang CS, Kelley MC (1996a) Nonlinear evolution of equatorial spread f 1. on the role of plasma instabilities and spatial resonance associated with gravity wave seeding. *J Geophys Res* 101(A1):283–292, URL <http://dx.doi.org/10.1029/95JA02211>

- Huang CS, Kelley MC (1996b) Nonlinear evolution of equatorial spread f 2. gravity wave seeding of rayleigh-taylor instability. *J Geophys Res* 101(A1):293–302, URL <http://dx.doi.org/10.1029/95JA02210>
- Jakobsen J (2009) A new method for evaluation of the ionospheric modeling error in a vrs based network rtk service. Proceedings of the 22nd International Technical Meeting of The Satellite Division of the Institute of Navigation (ION GNSS 2009) pp 2689–2695
- Jakobsen J, Pedersen SM (2009) Design of a GNSS kinematic slot car test track. Proceedings of the 13th IAIN World Congress in Stockholm Published by the Nordic Institute of Navigation
- Jakobsen J, Knudsen P, Jensen A (2008) Principle component analysis on absolute tec values and its impact on kalman filtering when using a priori information. Proceedings of the 2008 National Technical Meeting of The Institute of Navigation (7):884–892
- Jakobsen J, Knudsen P, Jensen A (2010) Analysis of local ionospheric time varying characteristics with singular value decomposition. *Journal of Geodesy* 84(7):449–456, URL <http://dx.doi.org/10.1007/s00190-010-0378-2>
- Jensen ABO (2002) Numerical Weather Predictions for Network RTK, 4, vol 10. National Survey and Cadastre, Denmark
- Johnson FS (1961) *Satellite Environment Handbook*. Stanford University Press
- Kaplan ED, Hegarty CJ (2006) *Understanding GPS, Principles and Applications*, 2nd edn. Artech House, 685 Canton Street, Norwood, MA 02062
- Klobuchar JA (1987) Ionospheric time-delay algorithm for single-frequency gps users. *IEEE Trans Aerospace and Electronic Systems* AES-23:325–331
- Klobuchar JA (1996) *Ionospheric Effects on GPS*. Published in B. W. Parkinson and J. J. Spilker. *Global Positioning System: Theory and Applications* Vol. 1-2. American Institute of Aeronautics and Astronautics
- Klukas R, Julien O, Dong L, Cannon E, Lachapelle G (2004) Effects of building materials on uhf ranging signals. *GPS Solutions* 8:1–8, URL

<http://dx.doi.org/10.1007/s10291-003-0080-4>, 10.1007/s10291-003-0080-4

Knight M, Finn A (1998) The effects of ionospheric scintillations on gps. Proceedings of the Institute of Navigation GPS, Nashville, TN pp 673–685

Komjathy A (1997a) Global Ionosphere Total Electron Content Mapping Using the Global Positioning System. Technical Report no. 188, Department of Geodesy and Geomatics Engineering, University of New Brunswick

Komjathy A (1997b) Global ionospheric total electron content mapping using global positioning system. PhD thesis, Department of Geodesy and Geomatics Engineering, University of New Brunswick, Fredericton, New Brunswick

Lachapelle G, Kuusniemi H, Dao DTH, Macgougan G, Cannon ME (2004) HSGPS signal analysis and performance under various indoor conditions. Navigation: Journal of The Institute of Navigation 51(1):29–43

Lantronix (2007) Matchport data sheet. <http://www.farnell.com/datasheets/72169.pdf>

Leandro RF, Langley RB (2007) The gps analysis and positioning software - a brief overview. Proceedings of ION GNSS 2007, Forth Worth, TX

MacGougan GD (2003) High sensitivity GPS performance analysis in degraded signal environments. PhD thesis, Department of Geomatics Engineering, Schulich School of Engineering, University of Calgary, UCGE Report no. 20176

Memarzadeh Y (2009) Ionospheric modeling for precise gnss applications. PhD thesis, Netherlands Geodetic Commission

Misra P, Enge P (2006) Global Positioning System, Signals, Measurements and Performance, 2nd edn. Ganga-Jamuna Press, P.O. Box 692, Lincoln Massachusetts 01773

Nava B, Radicella SM, Leitinger R, Coisson P (2006) A near-real-time model-assisted ionosphere electron density retrieval method. Radio Science 41:8 pp

- Nava B, Cosson P, Radicella SM (2008) A new version of the nequick ionosphere electron density model. *Journal of Atmospheric and Solar-Terrestrial Physics* 70(15):1856 – 1862, DOI DOI:10.1016/j.jastp.2008.01.015, URL <http://www.sciencedirect.com/science/article/B6VHB-4RS43S1-3/2/320a56907e808eb73ce5d56b8d6c19ed>, ionospheric Effects and Telecommunications, EGU 2007, Vienna, Austria, 15 - 20 April 2007 ; IRI/COST 296 Workshop Ionosphere - Modelling, Forcing and Telecommunications. Prague, Czech Republic, 10-14 July 2007; Asia Oceania Geosciences Society: AOGS 2007. Bangkok, Thailand, 30 July - 4 August 2007
- Nishioka M, Saito A, Tsugawa T (2008) Occurrence characteristics of plasma bubble derived from global ground-based gps receiver networks. *J Geophys Res* 113(A5):A05,301–, URL <http://dx.doi.org/10.1029/2007JA012605>
- NMEA (2008) NMEA 0183 v. 4.0 format from The National Marine and Electronic Association. <http://www.nmea.org/>
- Olimex (2009) PIC-LCD development board details. <http://www.olimex.com/dev/pdf/PIC/PIC-LCD.pdf>
- Papon J, Cohen M, Cotts B, Haque N (2010) Ionospheric morphology. Website, [http://nova.stanford.edu/~vlf/IHY\\_Test/Tutorials/TheIonosphere/IonosphericMorphology.pdf](http://nova.stanford.edu/~vlf/IHY_Test/Tutorials/TheIonosphere/IonosphericMorphology.pdf)
- Parker RL (2004) *Geophysical Inverse Theory*. Princeton University Press, Princeton, New Jersey
- Parma PSE (2009) RTR car description. [http://www.shopatron.com/products/productdetail/1/32+Womp-Womp+Steel+Chassis/part\\_number=572/137.0.1.1.6083.36166.36168.36328.0?](http://www.shopatron.com/products/productdetail/1/32+Womp-Womp+Steel+Chassis/part_number=572/137.0.1.1.6083.36166.36168.36328.0?)
- Parsons JD (2000) *Mobile Radio Propagation Channel*, 2nd edn. John Wiley & Sons
- Preisendorfer R, Mobley CD (1988) *Principal Component Analysis in meteorology and oceanography*. Elsevier Science Publishing Company, Amsterdam

- Rishbeth H, Mller-Wodarg ICF, Zou L, Fuller-Rowell TJ, Millward GH, Moffett RJ, Idenden DW, Aylward AD (2000) Annual and semianual variations in the ionospheric f2-layer: Ii. physical discussion. *Annales Geophysicae* 18(8):945–956, URL <http://dx.doi.org/10.1007/s00585-000-0945-6>
- Schaer S, GBeutler, LMervart, Rothacher M, UWild (1995) Regional ionosphere models using the gps double difference observable. *Proceedings of the IGS Workshop on Special Topics and New Directions*, Potsdam Germany, pp 77–92
- Schaer S, Beutler G, Rothacker M, Springer TA (1996) Daily global ionosphere maps based on gps carrier phase data routinely produced by the code analysis center. *Proceedings of the IGS AC Workshop*, Silver Spring, MD, USA, pp 181 – 192
- Seeber G (2003) *Satellite Geodesy*, 2nd edn. Walter de Gruyter, GmbH, Berlin
- Skone S (2007) Lecture notes, ENGO 633. University of Calgary
- SyRen (2010) SyRen10 regenerative motor driver product details. <http://www.active-robots.com/products/motorcon/syren10-details.shtml>
- Takac F, Zelzer O (2008) The relationship between network rtk solutions mac, vrs, prs, fkp and i-max. *ION GNSS 21st International Technical Meeting of the Satellite Division*, 16-19, Savannah, GA
- Tolman B, Harris RB, Gaussiran T, Munton D, Little J, Mach R, Nelsen S, Renfro B (2004) The GPS Toolkit: Open Source GPS Software. In: *Proceedings of the 16th International Technical Meeting of the Satellite Division of the Institute of Navigation*, Long Beach, California
- Tsunoda RT (1981) Time evolution and dynamics of equatorial backscatter plumes, 1. growth phase. *J Geophys Res* 86(A1):139–149, URL <http://dx.doi.org/10.1029/JA086iA01p00139>
- Tsunoda RT (1985) Control of the seasonal and longitudinal occurrence of equatorial scintillations by the longitudinal gradient in integrated e region pedersen conductivity. *J Geophys Res* 90 (A1)(A1):447–456

- U-blox (2003) U-blox ANN Antenne data sheet. [http://www.microem.ru/pages/u\\_blox/GPS-AntennaALPS/GPS-X-02021.pdf](http://www.microem.ru/pages/u_blox/GPS-AntennaALPS/GPS-X-02021.pdf)
- U-blox (2009) LEA-5T product description. [http://www.u-blox.com/images/downloads/Product\\_Docs/LEA-5T\\_Prod\\_Summary%28GPS.G5-MS5-07105%29.pdf](http://www.u-blox.com/images/downloads/Product_Docs/LEA-5T_Prod_Summary%28GPS.G5-MS5-07105%29.pdf)
- UNAVCO (2010) TEQC - The Toolkit for GPS/GLONASS/Galileo/SBAS Data. <http://facility.unavco.org/software/teqc/teqc.html>
- Wasmeier P (2010) Geodetic transformations. <http://www.mathworks.com/matlabcentral/fileexchange/9696-geodetic-transformations>
- Watson R, Lachpelle G, Klukas R, Turunen S, Pietila S, Halivaara I (2006) Investigating GPS signals indoors with extreme high-sensitivity detection techniques. *Navigation: Journal of The Institute of Navigation* 52(4):199–213
- Zalesak ST, Ossakow SL, Chaturvedi PK (1982) Nonlinear equatorial spread f: The effect of neutral winds and background pedersen conductivity. *J Geophys Res* 87(A1):151–166, URL <http://dx.doi.org/10.1029/JA087iA01p00151>





# Appendix A

Jakobsen J, Knudsen P, Jensen A (2008) Principle component analysis on absolute TEC values and its impact on Kalman filtering when using a priori information. *Proceedings of the 2008 National Technical Meeting of The Institute of Navigation*. (7):884-892, July 2008.

# Principle component analysis on absolute TEC values and its impact on Kalman filtering when using a priori information

J. Jakobsen, *The Danish National Space Center*

P. Knudsen, *The Danish National Space Center*

A. B. O. Jensen, *AJ Geomatics*

## BIOGRAPHY

Jakob Jakobsen holds a M.Sc. in civil engineering from the Technical University of Denmark and is currently enrolled in a PhD study on kinematic GNSS. He has three years of experience as an administrator for a nationwide RTK-network and three years of experience in the field of Geographic Information Systems.

Per Knudsen, Head of Department of Geodesy, PhD, is responsible for R&D activities related to GPS/GNSS at the Danish National Space Center as well as for the operation of permanent GPS reference stations in Greenland.

Anna B. O. Jensen holds a M. Sc. and Ph. D. and has worked with research, development and teaching related to GNSS for 15 years. Main areas of interest are high accuracy applications and modeling of atmospheric effects. She is a board member of the Nordic Institute of Navigation.

## ABSTRACT

In this work time series from 1999 – 2007 of absolute TECU for an area midpoint as well as a latitudinal and longitudinal variation of the electron density has been calculated using a Kalman filter. Dual frequency data from three reference stations in Denmark (56°N latitude) with a station separation of approximately 130-207 km. has been used.

For each year a Singular Value Decomposition (SVD) has been performed on the three variables in order to determine the daily, yearly and 11 year characteristic of the ionosphere.

The SVD analysis has shown a very dominant first eigenvalue (approximately 6 times larger than the second eigenvalue) and this eigenvalue correspond clearly to how the daily variation vary over the year. The second

eigenvalue correspond to how the width of the daily peak varies over the year and the third eigenvalue show a clear yearly variation of the daily signal with peaks around the equinoxes. For the latitudinal and longitudinal variations the first eigenvalue is less dominant (2-3 times larger than the second eigenvalue), but shows the same characteristic.

The eigenvalues for each year show a clear correlation with the sunspot number with a correlation coefficient of approximately 0.95.

A power spectrum for the entire time series has been processed and shows a yearly signal as well as a very clear daily signal with amplitude of approximately 7.4 TECU.

An a priori model of the ionosphere for the three variables is generated from the signals identified in the SVD analysis using the first three eigenvalues. This model is used to optimize the Kalman filter processing. When using the a priori model the standard deviation on the residuals are reduced especially during years with high ionospheric activity. Furthermore the initialization time of the Kalman filter are reduced significantly using the a priori models as starting values.

## INTRODUCTION

The ionosphere is in its nature varying over time. The main time characteristics include the 24 hour periodicity with a peak at 14.00 local time and low during nighttime, a yearly trend with peaks around equinoxes and a low, but longer peak during summertime, and a 11 year time period correlated with the sunspot number as described in e.g. Misra and Enge (2006).

The characteristics of the variation of the Total Electron Content (TEC) in the ionosphere are very different from latitude to latitude and thus an important factor for obtaining an accurate model is to use data from local GNSS reference stations, as described in Hargreaves

(1992). For instance in Denmark at approximately 56°N latitude the daily length vary considerable, compared to lower latitudes, making the daily variation of the ionosphere more different over the year.

Ionospheric modeling may improve the accuracy of the positioning of single-frequency receivers, because the largest error source in GNSS is the ionospheric delay. Furthermore precise ionospheric modeling is also important for other space based observation systems as well as communication systems and space weather studies. The observed rapid evolution of the ionosphere currently defies sufficient modeling to allow its prediction to future time epochs and therefore studies of its behavior are needed.

In the case of a near real time service providing information of the current status of the ionosphere it is important to have a good local a priori knowledge of the time varying ionosphere in order to reinitialize the Kalman filter, make a more robust processing, and to predict the status into future epochs in time. The a priori information can be generated by looking at local time series of the varying ionosphere.

## DATA AND LOCATION

For the test and verification, described in this paper, dual frequency data from three permanent reference stations in Denmark are used. The data are stored in the RINEX format with a sampling rate of 30 seconds. The stations form a triangle, as shown in Figure 2, with a station separation of approximately 130-207 km. A better estimate of the ionosphere is obtained when using three stations.



**Figure 2: Reference stations in Denmark used in the data processing.**

The center mark of the triangle is at approximately 56°N latitude, just below the auroral oval. The stations are maintained and operated by the National Survey and Cadastre.

## CALCULATION OF TIME SERIES

Three time series are calculated using a Kalman filter. The principle for the observation model, simplified to include one receiver, is shown in Figure 2. A single layer model, where the ionosphere is compressed into an infinitesimal shell at a given height is used. In this calculation it has been set to 400 km. The Ionospheric Pierce Point, IP, is the intersection of the shell and a direct line from the satellite (SV) to the GNSS receiver U1.

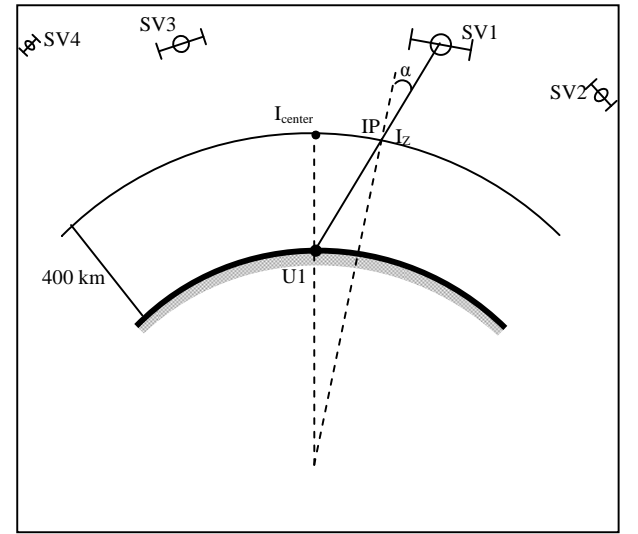


**Figure 1: Illustration of the observation model for one receiver**

By taking the difference of the L1 and L2 carrier observables, the geometry free solution L4 at a given time  $t$  for satellite  $s$  and receiver  $u$  can be written as,

$$L4_u^s(t) = L1_u^s - L2_u^s = \text{map}(\alpha_u^s)(I_z + \frac{\partial I_z}{\partial \beta}(\beta_u^s - \beta_{center}) + \frac{\partial I_z}{\partial \lambda}(\lambda_u^s - \lambda_{center})) + c_u^s$$

where

$center$  refer to the coordinates of the center of the triangle  
 $\beta$  and  $\lambda$  is the latitude and longitude in geomagnetic coordinates of the shell

$c$  is a constant for the given combination of  $u$  and  $s$ .

$I_z$  is the slant TEC at the IP

$\alpha$  is the zenith angle at the IP

This observation consists mainly of the delay in the ionosphere. This delay is converted to total electron

content (TEC), and split into three parts in order to represent the electron density at the center point, the absolute TEC at the pierce point and a variation of the electron density along the latitude and longitude. These three variables are all slant delays and are mapped to a vertical value. This mapping is a function of the elevation angle, which is a function of the Earth mean radius and of the ionospheric height of the shell. In this context the mapping function  $\frac{1}{\cos \alpha}$  is used, as described by for instance Seeber (2003).

Another part of the observation is the constant,  $c$ , consisting of the differential code biases for the satellites and GNSS-receivers and the integer ambiguity.

Assuming that no cycle slips occur and that it is only the three ionospheric parts, which change over time, the number of observations and the number of unknowns can be written as,

Observations	Unknowns
$n \cdot m$	$n + 3m$

where  $n$  is number of visible satellites at each epoch  $m$ .

The unknowns can over time be estimated using a Kalman filter. The Kalman filter is a dynamic filter that essentially can be described by 5 equations given in equations ( 1) - ( 5). Welch and Bishop (2006),

$$K_k = P_k^- H_k^T (H_k P_k^- H_k^T + R_k)^{-1} \quad (1)$$

$$\hat{x}_k = \hat{x}_k^- + K(z_k - H_k \hat{x}_k^-) \quad (2)$$

$$P_k = (I - K H_k) P_k^- \quad (3)$$

$$\hat{x}_{k+1}^- = A_k \hat{x}_k + B_k u_k \quad (4)$$

$$P_{k+1}^- = A_k P_k A_k^T + Q_k \quad (5)$$

In this processing the term  $B_k u_k$  in equation ( 4) is set to zero, because there is no input from observations outside the system and the  $A$  matrix equals the identity matrix. For an explanation of the remaining variables the reader are referred to Welch and Bishop (2006).

The observation model and the Kalman filter were implemented in Matlab and nine full years of data from the GNSS reference stations described above were processed to obtain vertical TEC values as well as latitude and longitude electron density variations for the center point every 30 seconds through the nine years.

During the processing of the three time series data gaps in the RINEX files were observed. Values originating from initialization of the Kalman filter after the data gaps, have been removed. The calculated time series from the entire

period 1999 – 2007 can be freely downloaded from <http://www.heisesgade.dk>.

## SVD ANALYSIS ON THE TIME SERIES

The Singular Value Decomposition (SVD) is a technique for decomposing a matrix into a product of three factors.

When the data set correspond to samplings of continuous variables a plot of the elements reveal recognizable patterns, see Parker (1994).

For a given  $m \times n$  real valued matrix  $X$  the equation for SVD of  $X$  is, see Parker (1994),

$$X = USV^T \quad (6)$$

where  $U$  is a  $m \times m$  matrix

$V$  is a  $n \times n$  matrix

And  $S$  is a diagonal matrix of size  $m \times n$ .

$U$  and  $V$  are both orthogonal matrices and  $S$  is a diagonal of nonnegative values and are called the singular values of  $X$ . SVD is closely related to Principle Component Analysis and to eigenvalue computation.

The time series generated with the Kalman filter has been organized into 9 yearly  $96 \times 365$  matrices, where each value is the mean over 15 minutes. Each yearly matrix corresponds to the  $X$  matrix in equation 6. The  $U$  matrix will correspond to the daily variation and the  $V$  matrix will correspond to the yearly variation. The SVD is performed using the LAPACK routine, described by Anderson, E (1999).

The result of the SVD for the first eigenvalue can be seen in Figure 3. A very clear daily signal of the total electron content is observed in the  $U$  matrix. This signal has approximately the same shape and magnitude for all nine years. It should be noted, that the signal never reach zero values, meaning that the daily variation of the vertical electron content will always be present. In the  $V$  matrix it is observed how this daily signal varies through the year. The signal is noisy, meaning that there is no correlation of the total electron content for the daily variation from day to day. A trend can be seen for the years with decreasing ionospheric activity (2004 - 2007) where the yearly variation appears to be somewhat similar.

The first 5 eigenvalues are illustrated in the middle row. The ratio between the first and the second is approximately 1/6 meaning, that the first eigenvalue dominate the time serie for the total electron content. The eigenvalues during the 9 years also show a variation similar to the sunspot number.

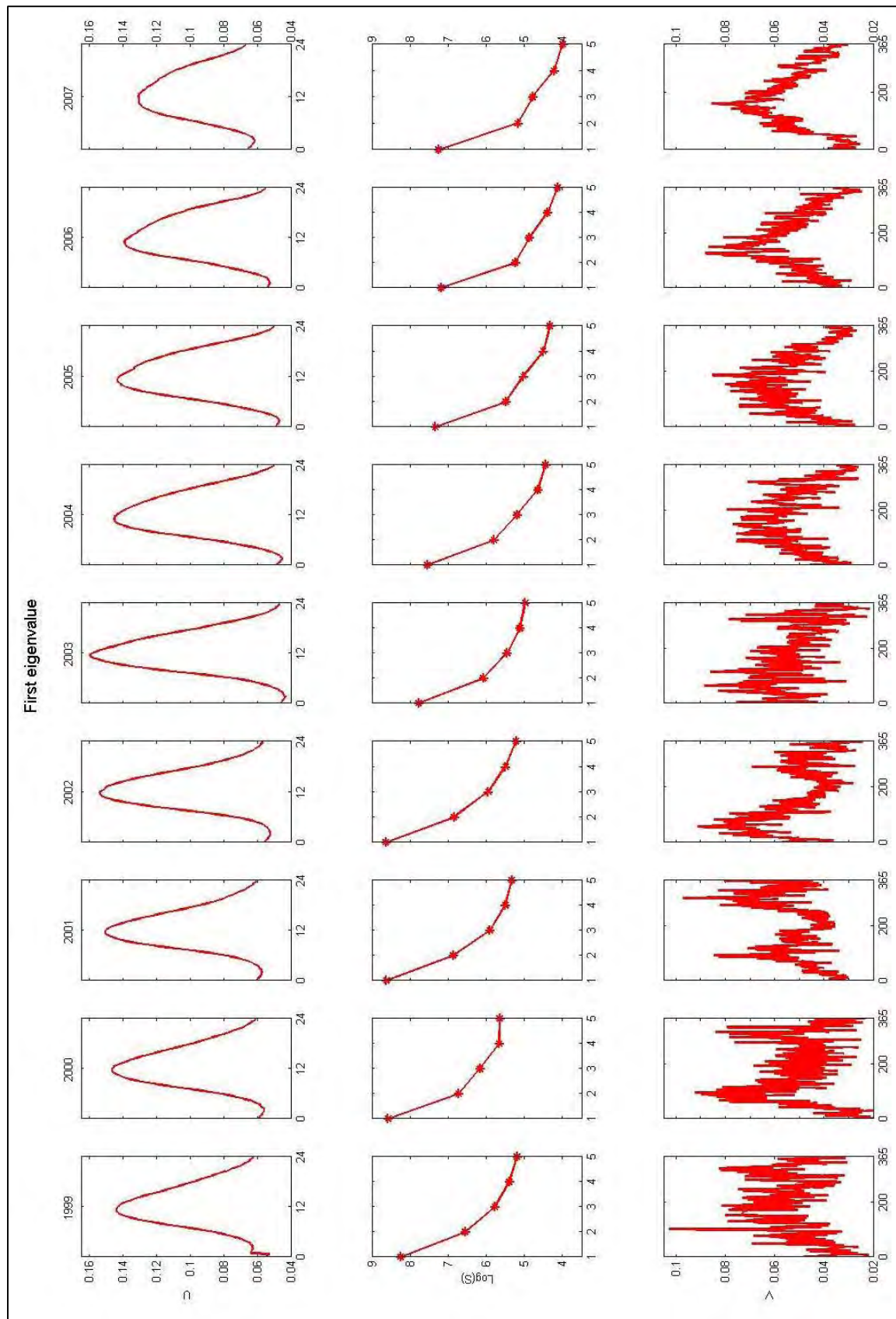
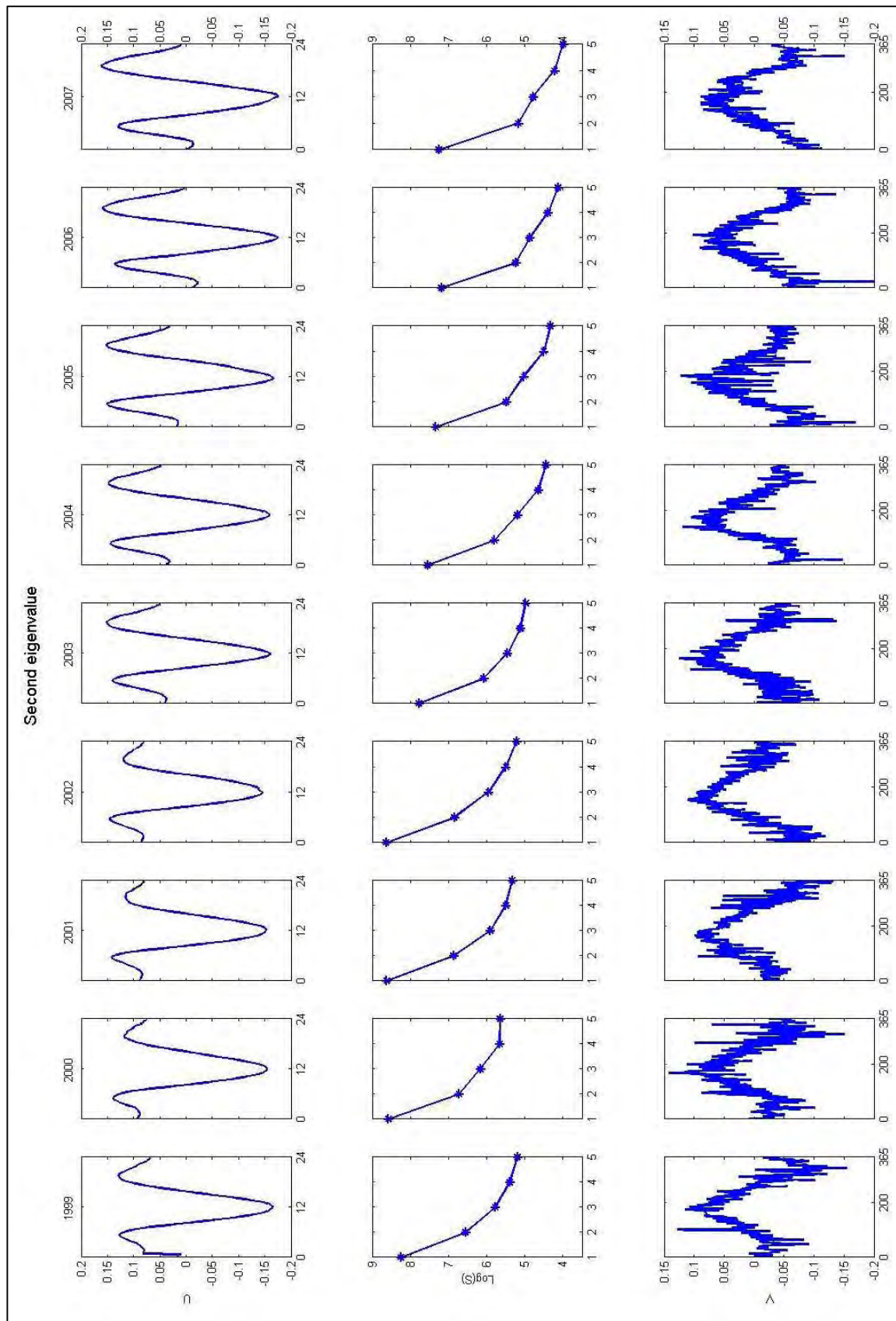


Figure 3: U, S, and V matrices for the first eigenvalue





**Figure 4: U, S, V and matrices for the second eigenvalue.**

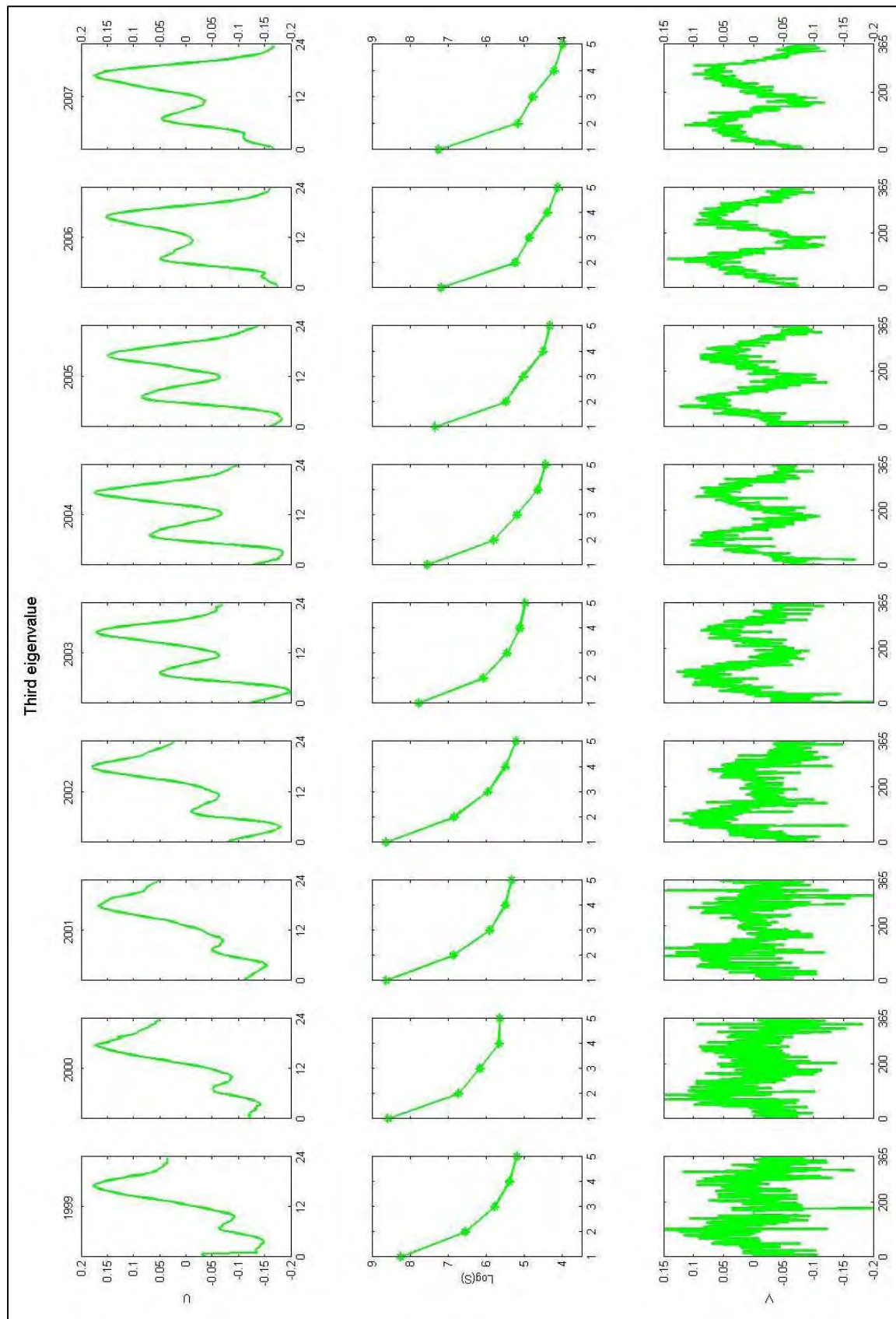


Figure 5: U, S, and V matrices for the third eigenvalue.

Each set of eigenvalues 1-5 over the 9-year period has been correlated with the sunspot number. The correlation coefficient lies between 0.93 and 0.97, indicating a strong correlation of the total electron content with the sunspot number. The used Sunspot Number is the monthly mean number from the Space Weather Prediction Center (<http://www.swpc.noaa.gov/ftpd/weekly/RecentIndices.txt>).

For the second eigenvalue, see Figure 4, another clear daily signal is observed over the years. Since the values of  $U$  both are positive and negative, this signal determines the width and height variations of the signal of the first eigenvalue. A more clear repeating yearly signal can be observed, which correspond to the variation of the length of day in Denmark.

For the third eigenvalue, see Figure 5, a yearly trend is very clear, which clearly shows a variation of the daily signal to be emphasized at the equinoxes. For the fourth and following eigenvalues there is no recognizable pattern over the years in the daily and the yearly signal. Therefore will the contribution from these eigenvalues not be used in the generated ionospheric model.

The same analysis has been performed on the time series for the latitudinal and longitudinal variation of the electron density with the same characteristics.

## POWER SPECTRUM OF THE TIME SERIES

The TECU time series is shown for the 283 – 288 day of year 1999 in Figure 6 to the left. The daily period, observed in the power spectrum to the right can be verified. The amplitude of the daily signal is 7.4 TECU. In the side lobes of the daily signal a yearly modulation of the daily cycle can be observed.

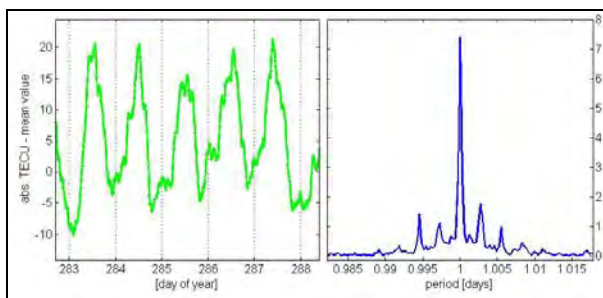


**Figure 6: Power spectrum for the TECU time serie.**

A period of exactly 365 has also been identified, but it not shown in the paper. The amplitude of that signal is 2.6 TECU. The power spectrum for the longitudinal variation shows similar conclusion of the periods, but the power spectrum of the latitudinal variation also shows a half-year period with the same amplitude as the yearly period.

In all three power spectra a strong contribution from the 11 year period is also identified.

## GENERATION OF AN A PRIORI MODEL

Based on the power spectrum, where a clear daily signal and a yearly signal was identified and based on the SVD analysis, where the shape and daily variation over the year was identified for the first three eigenvalues a model of the time varying ionosphere each year is generated. This is done for all the three variables, which was estimated in the Kalman filter. The result for the TECU from year 2004 is illustrated in Figure 7. The daily signal from day to day has been smoothed in order to obtain a yearly trend and suppress the fact that there is no correlation from day to day. The models from 2004 -2007 show approximately the same shape, because they have similar  $U$  and  $V$  matrices, but the magnitude is different as the eigenvalues are different every year.

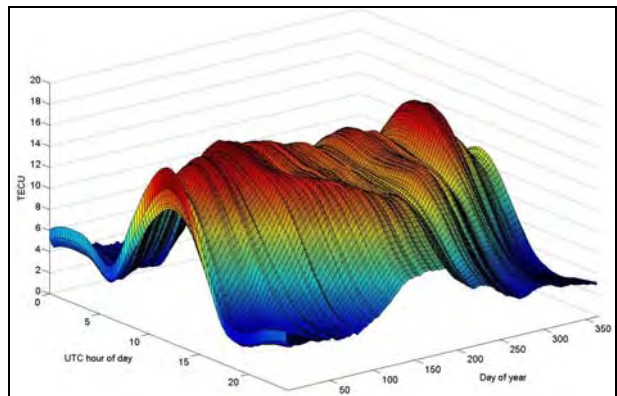


**Figure 7: Generated ionosphere model for 2004.**

## IMPACT ON KALMAN FILTERING

The three time series (the TECU and the latitudinal and longitudinal variation of the electron density) were generated in a first processing of the data without using any a priori knowledge. The generated ionosphere model based on empirical data is now implemented in the Kalman filter in the prediction step for the three variables. At each epoch a change from the last epoch to the current is calculated and inserted in the  $u$  vector in the prediction step in equation 4.

An analysis on the variance of the three variables (the diagonal elements of the  $P$  matrix equations (1) to (5)), has been performed in order to see if a trend could be identified, so the  $Q$  matrix could be time varying as well. The conclusion of this analysis is, that the variance was mainly correlated with the repetition time of the satellite constellation (23 hours and 56 minutes). The DOP value is thus more dominating than the variance of TECU. So the  $Q$  matrix is kept constant through the second processing, as was the case in the first processing.



The impact on the Kalman filtering has been divided into two cases

- Effect of time series with no data gaps
- Effect on initialization time of the Kalman filter

In Figure 5 an example plot of the residuals for day of year 192 in 2002 with and without using a priori information is illustrated. The RMS of the residuals is reduced, but the improvement is practically non existent as the two curves basically overlap each other. The sampling rate of 30 second is simply too high in order to reveal major improvement in the optimization of the Kalman filter.

A tendency of a reduction on the peaks of the residuals can be identified, which is a general trend looking at the larger time serie. The effect is largest during years with high ionospheric activity as illustrated in the figure.

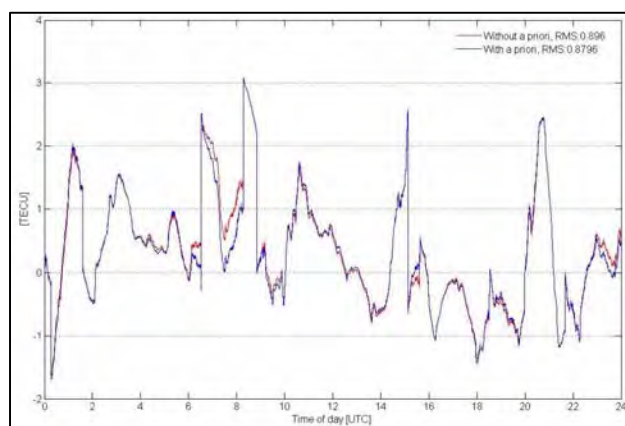


**Figure 8: Residuals with and without using a priori information for day of year 192 in 2002.**

In Figure 9 the effect of using a priori knowledge in the initialization of the Kalman filter is illustrated for day of year 189 in 2001. The blue curve is generated using zeros as starting values for the three variables as well as the constants. The red curve is the generated using a priori information for the three variables and zeros for the constants. It can be seen that the initialization time is reduced significantly.

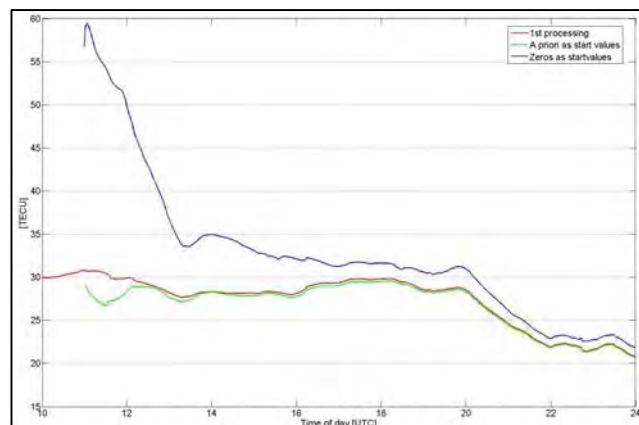


**Figure 9: Illustration of initialization time with and without using a priori information.**

## CONCLUSION

The Singular Value Decomposition analysis has shown a very dominant first eigenvalue (approximately 6 times larger than the second eigenvalue) and this eigenvalue correspond clearly to how the daily variation vary over the year. The second eigenvalue correspond to how the width of the daily peak varies over the year and the third eigenvalue show a clear yearly variation of the daily signal with peaks around the equinoxes. For the latitudinal and longitudinal variations the first eigenvalue is less dominant (2-3 times larger than the second eigenvalue), but shows the same characteristic.

The eigenvalues for each year show a clear correlation with the sunspot number with a correlation coefficient of approximately 0.95.

The power spectrum for the three time series show a yearly signal as well as a very clear daily signal with an amplitude of approximately 7.4 TECU.

The impact on the Kalman filtering when using a priori has shown that the standard deviation on the residuals are reduced especially during years with high ionospheric activity, but no major optimization of the filter was identified. Furthermore the initialization time of the Kalman filter are greatly reduced using a priori information.

## ACKNOWLEDGMENTS

C. C. Tscherning, University of Copenhagen, is acknowledge for his contribution in the SVD analysis and for his comments through the work. P. Jarlemark, SP, Sweeden is acknowledged for giving access to his expert knowledge of the Kalman filter.

## REFERENCES

Anderson, E., et al. (1999). LAPACK user guide, third edition, *Society for Industrial and Applied Mathematics*,

Hargreaves, J.K. (1992), The Solar-Terrestrial Environment. *Cambridge University Press*.

Hofmann-Wellenhof, B., Lichtenegger, H. and Collins, J., (2001), GPS - Theory and Practice, Fifth edition, *Springer, Wien - New York*.

Jensen, A. B. O., Ovstedal, O., Grinde, G. Development of a Regional Ionosphere Model for Norway, *ION GNSS 2007*.

Misra, P., Enge, P. (2006). Global Positioning System, Signals, Measurements, and Performance. *Ganga-Jamuna Press*.

Parker, R. L. (1994). Geophysical Inverse Theory, *Princeton University Press*.

Seeber, G (2003). Satellite Geodesy, second edition, *Walter De Gruyter GMBH*.

Schaer, S., Beutler, G., Mervart, L., Rothacker, M., Wild, U. (1995). Global and Regional Ionosphere Models using the GPS Double Difference Phase Observable, *Proceedings of the IGS Workshop on Special Topics and New Directions, Potsdam Germany*.

Schaer, S., Beutler, G., Rothacker, M., (1998). Mapping and Predicting the Ionosphere. *Proceedings of the IGS AC Workshop, Darmstadt, Germany*.

Welch, G and Bishop, G. (2006). An introduction to the Kalman Filter, *Department of Computer Science, University of North Carolina*.

# Appendix B

Jakobsen J (2009) A new method for evaluation of the ionospheric modeling error in a VRS based network RTK service. *Proceedings of the 22nd International Technical Meeting of The Satellite Division of the Institute of Navigation (ION GNSS 2009)*, pages 2689-2695, September 2009.

# A New Method for Evaluation of the Ionospheric Modeling Error in a VRS based Network RTK Service

Jakob Jakobsen, Technical University of Denmark, National Space Institute

## BIOGRAPHY

Jakob Jakobsen holds a M.Sc. in civil engineering from the Technical University of Denmark and is currently enrolled in a PhD study on kinematic GNSS. He has three years of experience as an administrator for a nationwide RTK-network and three years of experience in the field of Geographic Information Systems.

## ABSTRACT

The overall goal of any Network Real Time Kinematic (NRTK) service is to provide the best position accuracy. However evaluating the NRTK service in the positioning domain does not give a full insight in how well the NRTK service is performing as this also includes errors from the rover.

The new method presented in this paper provides a possibility to evaluate a NRTK service, based on the Virtual Reference Station (VRS) technique independent of the rover. This is done by comparing observations from a VRS generated at the exact same location as a true reference station. This paper focus on the ionospheric modeling error in the NRTK service, and therefore the geometry free observation is used. The ionospheric modeling error in the NRTK service is extracted and analyzed.

Nine true GNSS stations with observations from a day with low and a day with higher ionospheric activity has been chosen to identify dependencies based on satellite elevation, distance to nearest reference station in the interpolation area, distance to nearest reference station in the extrapolation area, and the dependency on the daily ionospheric activity.

The results show that the elevation angle dependency is the largest contribution to the modeling error with a standard deviation just above 0.5 cm for low elevation angles, and decreasing to the mm level for high elevation angles. When the distance to the nearest reference station in the network is increased, the elevation modeling error is also increasing.

The results also shown that with increased distance to nearest reference station in the interpolation area, a trend referring to the daily ionospheric cycle can be seen. This trend is magnified for the day with higher ionospheric activity.

The ionospheric influence on the model error has shown, that with the current (February 2009) level of ionospheric activity, the station separation can be rather large, before a significant degradation of the accuracy will occur. With the increasing level of ionospheric activity over the next years, a magnified model error can be expected. The station separation can thereby become a limiting factor for the modeling of the ionosphere in a NRTK.

## INTRODUCTION

The number of Network Real Time Kinematic, NRTK, services has increased over the last several years. The advantages of modeling the different error sources present in the GNSS position processing over a large geometric area have shown its great potential.

The overall goal of any RTK solution, whether it is based on the single station or on the network approach, is to optimize the quality of the calculated rover position. The process of calculating a position involves several steps, which involves different segments. There are several ways of placing the processes for calculating a position at the NRTK service control center or performing the tasks on the rover equipment, see for instance (Takac 2008).

In Figure 1 is the general process of calculating a position using a NRTK service based on the Virtual Reference Station (VRS) concept, split into three segments.

- The GNSS system
- The NRTK service
- The rover

Optimizing the process for one segment will in the end improve the overall position accuracy.

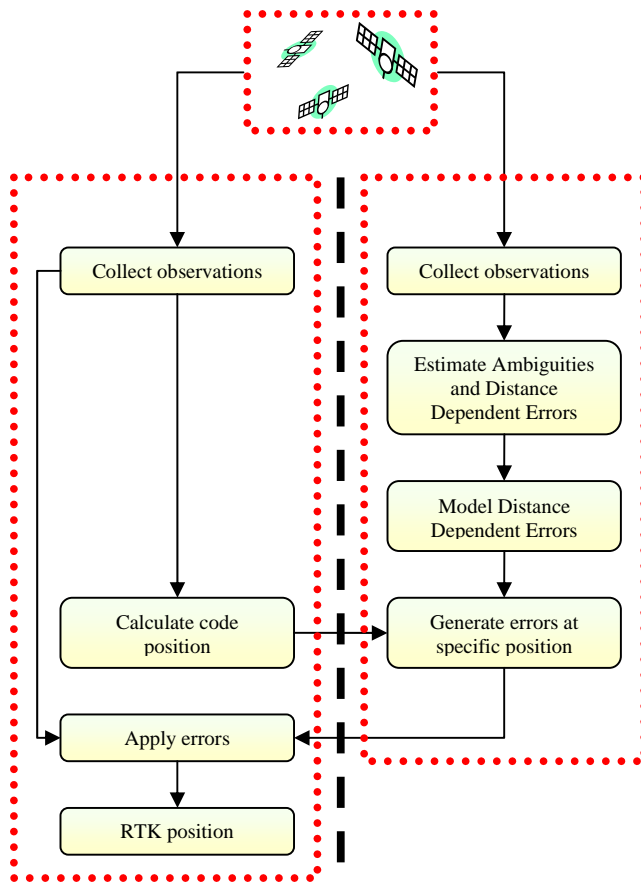


**Figure 1: The three segments, indicated by the red dotted lines, involved in the general process of calculating a position in a NRTK service using the VRS concept.**

The process for the NRTK service segment consists of collecting and synchronizing phase observations from the GNSS satellites to a number of physical reference stations. Then process these data for each satellite and for each station, to estimate the integer ambiguities and distance dependent errors. The distance dependent errors include the contribution from the ionosphere, the troposphere and to a certain degree the error of the positions of the SV. Then combine the distance dependent errors for each station into a model for each satellite in order to distribute new phase observations at any given position within the NRTK service coverage area as if it was a true reference station.

The processes for the rover segment consists of collecting code and phase observations, calculate and send a code position to the network. Then apply the received errors to the collected phase observations and in the end calculate a RTK position.

With the increasing number of NRTK services, also NRTK services sharing coverage areas, the end user needs parameters in order to evaluate or to compare NRTK services in order to choose the most appropriate service to fit his needs. This is mostly done by looking at the position accuracy. However an evaluation of the NRTK service or a comparison of NRTK services in the positioning domain involves many parameters which may or may not refer to the process in the rover.

The rover equipment on the market today consists of receivers with different brands, different age, different firmware versions and different antennas which all affect the position accuracy.

This means, to fully evaluate a NRTK service in the positioning domain, the service needs to be tested with all these rover equipment in a huge mix and match setup. Furthermore this huge setup of receivers and antennas should be performed at the exactly same time where the satellite geometry, the ionospheric and tropospheric conditions are the same.

Therefore, an evaluation of a NRTK service independent of the rover is needed.

### THE NEW METHOD

This new method overcomes the problem where the evaluation of a NRTK service is dependent on the performance of the rover.

The basic idea is to look at the data interfacing the NRTK service and the rover, rather than look at the position accuracy. This interface basically consists of a Virtual Reference Station, VRS, sent to the rover as if it was a true reference station. Comparing this VRS with true observations would give an indication of how well the VRS has been generated and how well the distance dependent errors in the NRTK service have been modeled.

This can be accomplished by generating a VRS at the exact same location where a real reference station is already present and then compare observations between the virtually and the real station.

This paper is focusing on the ionospheric modeling error in a NRTK service. A 1 dimensional illustration of this is presented in Figure 2. Each reference station observes the true value of the ionosphere error and the NRTK service interpolates between them using a model. The discrepancy between the model and the true ionosphere at the VRS position is described by the modeling error. Normally this will be a function of distance between the nearest reference station and the VRS, but situations where the model is correct at larger distances and incorrect at shorter distances may happen.

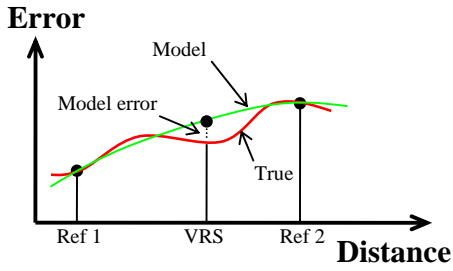


**Figure 2: 1 dimensional illustration of the NRTK service ionospheric modeling error**

The error of the ionosphere for a given reference station can be computed using the geometry free L4 observation. This observation can be written as in the following equation described for instance by (Feng 2008).

$$L4^s = L1^s - L2^s =$$

$$I + \lambda_1(N_1^s + \phi_1 - \phi_1^s) - \lambda_2(N_2^s + \phi_2 - \phi_2^s)$$

Where  $\lambda$  is the wavelength of the carrier

subscript 1 and 2 refer to the L1 and L2 carrier

s refer to the satellite number

I refer to the total electron content in the ionosphere

$\phi$  is the initial phase

and N is the integer ambiguity

Assuming that no cycle slips occur and that the initial phases are constant over a short period of time, the only varying part is the variation of the ionosphere.

The variation of the model error in the NRTK service can then be expressed as in the following equation

$$\sigma(I_{model\ error}) = \sigma(L4_{true}^s - L4_{VRS}^s)$$

Where *true* refer to the true reference station

VRS refer to the virtually generated reference station

### STATION AND DATA SELECTION

It is assumed that the ionospheric modeling error is dependent on the following four conditions

- Elevation angle of the considered satellite
- The general ionospheric activity
- Distance to nearest reference station in the interpolation area
- Distance to nearest reference station in the extrapolation area

Therefore for this work 9 real reference stations have been selected independent of the NRTK service based on these assumptions. The location of the selected 9 real reference stations can be seen in Figure 3. They are all

geodetic receivers put up in environments to minimize multipath. In Table 1 is the exact distance listed as well and for the stations in the extrapolation area the distance to the interpolation area is also listed.

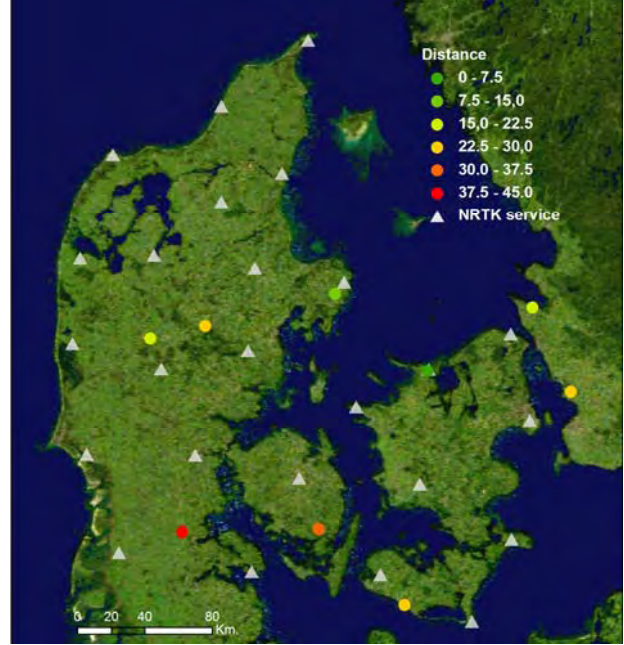


**Figure 3: Position of selected stations based on distance to the nearest NRTK reference station in the interpolation and extrapolation area.**

The NRTK service used for this test is based on the VRS principle and consists of 26 GNSS reference stations with a station separation of approximately 60-80 km. It is not known which model the network is using for the interpolation of the ionospheric error.

	Name	Dist. to nearest ref. station [km.]	Distance to inter. area. [km.]
Inter. area	Nysj	1.2	-
	Tru1	8.8	-
	Hern	19.4	-
	Silk	29.4	-
	Svnd	32.4	-
	Rode	39.7	-
Extra. area	Rod1	23.1	9.8
	0Jon	20.5	20.5
	0Jod	29.8	27.3

**Table 1: Distance to nearest NRTK reference station for selected real stations, and additionally distance to the interpolation area from the three selected real stations located in the extrapolation area.**

24 hour Rinex files with a sampling rate of 30 seconds have been generated for each location of the true reference station using the NRTK service post-processing feature. Analysis has been performed on real-time VRS

vs. post-processed VRS and has shown 100 % correlation between these on the L4 observable, though the L1 and L2 observation correlation considered separately was lower.

Two days, day 45 and 51 in 2009, have been selected to represent a day with low and a day with higher ionospheric activity. The daily ionospheric cycle for the chosen days can be seen in Figure 4. The general cycle consists of an ionospheric activity low almost constant during night, rising at sunrise to a maximum at approximately 1400 hours local time, and then slowly decaying in the afternoon. The daily cycle varies in size and shape over the year as well as over the 11 year solar cycle.

The cycles have been calculated from three GNSS reference stations (independent of the NRTK service and the 9 selected real stations) using a Kalman filter approach, see Jakobsen et al. (2008) for further information on the procedure used.

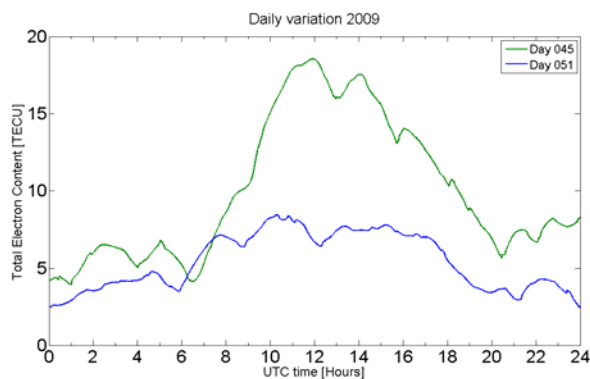


**Figure 4: The daily Total Electron Content cycle for the two considered days.**

The stations are located in the midlatitude region at app. 56 degrees latitude just below the auroral oval.

### ELEVATION ANGLE DEPENDENCE

In Figure 5 is the standard deviation of the model error grouped into 5 degrees bins for the satellite elevation angle illustrated for the station Nysj situated 1.2 Km. from the nearest NRTK service reference station. The red line indicates the mean value based on all the satellite passes.

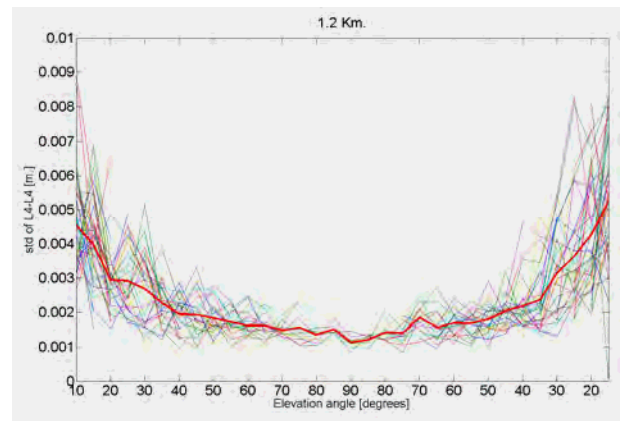


**Figure 5: The  $\sigma$  of the model error grouped into bins of the satellite elevation angle for all satellite passes during 24 hours. The thick red line indicates the mean value.**

The variation of the model error is significantly dependent on the elevation of the satellite, with higher values for low elevation angles. This can be interpreted as the NRTK system generally models the ionospheric error worse when the signal path between the satellite and reference station passes through more ionosphere. The shape is observed for all the considered stations for both days indicating that it is present at all locations at all times inside the interpolation area as well as in the extrapolation area. For greater distances and higher ionospheric activity an increase in the modeling error for the high elevation bins is observed.

### DISTANCE AND BACKGROUND IONOSPHERE DEPENDENCE

The elevation dependence for each satellite pass has been minimized by using a traditional mapping function based on the elevation of the satellite, Seeber (2003). Furthermore has the elevation mask in the following data processing been set to 20 degrees to minimize any contribution from the elevation dependency. Then, each satellite pass has been processed calculating the standard deviation of the model error over a period of 10 minutes. The mean value for all the visible satellites at a given time is plotted for the 9 stations for the two days analyzed in Figure 6. In the data processing, cycle slips were detected and observations referring to those periods have been removed.

For the blue lines in the plot, referring to day 51 the day with low ionospheric activity, a trend for the stations inside the interpolation area can be observed. The variation of the model error is in general increasing with a larger distance to the nearest NRTK reference station. Furthermore can a correlation with the daily ionospheric cycle be observed at greater distances.



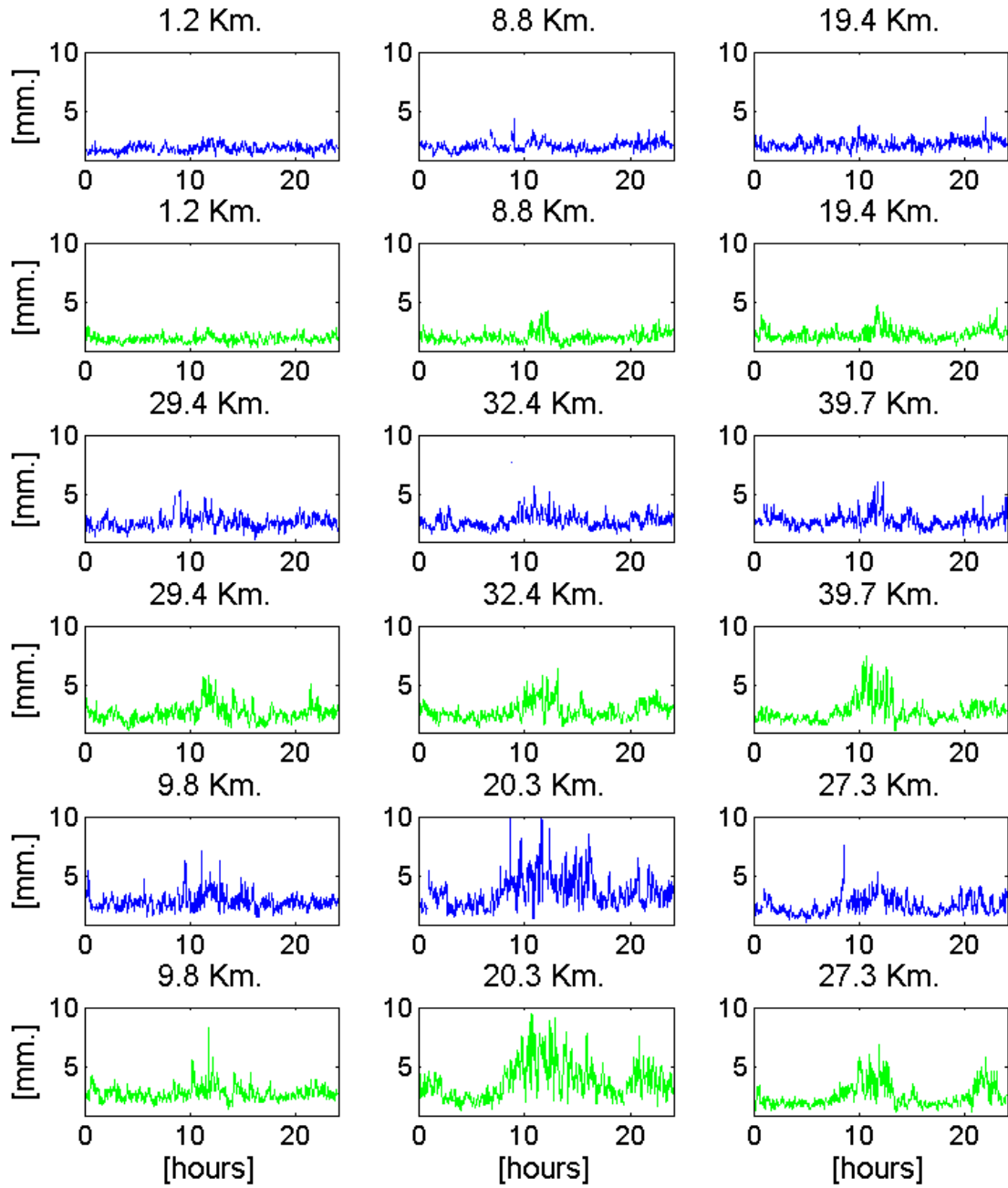


Figure 6: Standard deviation of L4-L4. Blue refer to day 51 with low ionospheric activity and green refer to day 45 with higher ionospheric activity. The upper 12 plots are for stations located inside the interpolation area and the lower 6 plots are for stations located in the extrapolation area. The distance to nearest NRTK reference station is shown as well.



The same trends can be observed for the green lines in the plots, referring to day 45 the day with higher ionospheric activity. Compared to the lines for day 51, the trend is magnified especially during mid day, where the daily ionospheric activity is also higher than for day 51.

Looking at the stations in the extrapolation area the last 6 plots in Figure 6, also reveal dependency on the distance to nearest NRTK reference station. For the closest one the pattern observed is similar as for the stations inside the interpolation area, which is expected because the distance to the interpolation area is relatively small. But the two other stations show another pattern. The daily cycle dependency is clearly visible for both stations, but the closest station has the largest magnification. This can be explained by looking at the location of the station compared to the interpolation area in the NRTK service. The closest station is placed north and east of the interpolation area, while the station further away is placed east of the interpolation area, which can be interpreted as the extrapolation conditions are better for this station.

A night contribution is slightly present for the green plots, especially in the extrapolation area. This night contribution is also present on the daily cycle, however it should not have that significant impact on the model error. A possible explanation could be that constraints on the ionospheric activity exist in the NRTK service processing during nighttime. This may result in a higher model error.

### IMPACT IN THE POSITIONING DOMAIN

The ionospheric model error will contribute to the position accuracy. Looking at the rule of thumb given in the following equation, see for instance Misra and Enge (2006).

$$\sigma_{3Dpos} = PDOP \cdot \sigma_{pseudo}$$

The contribution from the model error can be considered as the extra error compared to a single station (SS) solution and then the formula can be expressed as

$$\sigma_{3Dpos} = PDOP \cdot \sqrt{\sigma_{pseudo,SS}^2 + \sigma_{Model\_error}^2}$$

Though the model error analyzed in this paper contributes very little to the standard deviation of the pseudorange, this contribution will be magnified by the geometry for the satellite constellation, which is also changing over time.

Comparing a single station solution with the NRTK service solution, will give a higher standard deviation on the pseudorange accuracy, especially on low elevation satellites. Therefore a higher elevation mask should be considered. In situations with many visible satellites, this

should be preferred, since the PDOP will not be significantly affected. In situations with fewer visible satellites, increasing the elevation mask might increase PDOP giving the improved standard deviation on the pseudorange little effect.

The end user shall consider the time varying parameters of the satellite constellation as well as the ionospheric model error observed in this paper in the process of optimizing the position accuracy while he is doing fieldwork.

### CONCLUSION AND FUTURE WORK

Even though the ionospheric activity in general is low for the two considered days, the following dependencies can be observed for the ionospheric modeling error.

A dependency on the satellite elevation is observed at all stations both days reaching up to 10 mm. for low elevations.

With increasing distance to nearest reference station the ionospheric model error is also increasing. And this trend is magnified with higher ionospheric activity.

In the extrapolation area the ionospheric model error is dependent on the geometry of the nearby interpolation area, but shows the same elevation, distance, and ionospheric dependencies as with station inside the interpolation area.

Considering the coming solar maximum where the activity in the ionosphere are expected to increase to app. 5-6 times the current level, considerations regarding the modeling error should be performed. Designing or redesigning existing NRTK services should consider the station separation carefully in order not to degrade the position accuracy coming from the modeling error itself.

It is well known that the data lines from the reference stations in the NRTK service can break down for small periods of time. During these periods the distance to nearest reference station will increase, and will lead to higher ionospheric modeling error. In cases where the fall out station is a boundary station the modeling error may increase significantly as certain areas will now be in the extrapolation area.

Further tests of the ionospheric modeling error in the NRTK service shall be performed in order to better understand the correlation to the ionospheric activity. Campaigns performed over the year as well as campaigns in the coming year would be of great interest.

### ACKNOWLEDGMENTS

Leica Denmark, operating the Spidernet, the Swepos service in Sweden and Geoteam in Denmark operating

the GPSnet is acknowledged for providing the data used in this work. GPS Toolkit has been used to generate different kind of observations and is therefore also acknowledged

## REFERENCES

Takac, F., and Zelzer, O., (2008), The relationship Between Network RTK Solutions MAC, VRS, PRS, FKP and i-MAX, In: Proc of the ION GNSS 21st. International Technical Meeting of the Satellite Division, 16-19, September 2008, Savannah, GA.

Jakobsen, J., Knudsen, P., Jensen, A. B. O., (2008), Principle component analysis on absolute TEC values and its impact on Kalman filtering when using a priori information, In: Proc of ION National Technical Meeting 2008, San Diego, California, January 28-30

Seeber, G (2003). Satellite Geodesy, second edition, *Walter De Gruyter GMBH*.

Misra, P., Enge, P. (2006). Global Positioning System, Signals, Measurements, and Performance. *Ganga-Jamuna Press*.

Feng Y (2008). GNSS three carrier ambiguity resolution using ionosphere-reduced virtual signals. *Springer-Verlag*

# Appendix C

Jakobsen J, Pedersen SM (2009) Design of a GNSS kinematic slotcar test track. *Proceedings of the 13th IAIN World Congress in Stockholm. Published by the Nordic Institute of Navigation*, October 27-29 2009.

# Design of a GNSS kinematic slot car test track

*Jakob Jakobsen, DTU Space, National Space Institute  
Søren Møller Pedersen, DTU Space, National Space Institute*

## BIOGRAPHY

Jakob Jakobsen holds a M.Sc. in civil engineering from the Technical University of Denmark and is currently enrolled in a PhD study on kinematic GNSS. He has three years of experience as an administrator for a nationwide RTK-network and three years of experience in the field of Geographic Information Systems.

Søren Møller Pedersen joined the Danish Space Research Institute in 1998 as an electronic engineer. He has participated in the Jem-X Instrument flying project, a part of the Integral mission currently flying, in the field of PCB testing and verification. He has furthermore participated in developing electronics for space missions like ASIM and Exomars.

## ABSTRACT

When performing kinematic tests it is important to know the absolute coordinate in any given instance of time. An external logging system is often used, which must be synchronized in time with the data rate of the testing equipment. This task is difficult to perform with high accuracy and in the same time sustain advantages like portability, multiplicity, flexibility, and statistically.

A slot car track has been built, tested and verified in order to establish a reference geometry and to provide an overall absolute accuracy of 5 mm. in any given instance of time. It consists of various plates with implemented position sensors to make an external logging system of the car.

The verification of the track has shown that the reference geometry has an accuracy of 1.1 mm. level and that the position of the car interpolated between the position sensors are below 5 mm.

Preliminary kinematic tests have been performed and the functionality of the track is illustrated. This includes the absolute accuracy for the travelled geometry and the possibility to perform position comparison on an epoch by epoch basis with high accuracy.

## INTRODUCTION

In the field of surveying a well-known procedure for making tests of GNSS equipment is to put the GNSS antenna fastened on a tripod. The main function of the tripod is to maintain the antenna at the exact same location throughout the time period of the test. That is to have a reference point (X, Y, Z) fixed in an Earth Centered Earth Fixed, ECEF, coordinate system. This can for instance be used as comparison to the position generated by the testing equipment, but also in the GNSS observation domain to extract the geometric distance.

Locating the reference point in an absolute sense is important because it reveals any systematic errors in the testing equipment and not just relative errors.

Using a tripod as the reference point has further advantages and a few of these is listed below.

- Portable
- Multiple
- Flexible
- Statistical

The portability gives the user the possibility to perform tests in different locations, that is both indoor and outdoor, as well as various urban and countryside scenarios. Also multiple tripods can be setup with different equipment at the same time, whether this is testing under the same or deliberate different conditions. Since the tripod is static the generated statistical parameters of the test makes a good foundation for testing equipment whether the test is performed in the GNSS observation domain or the fixed coordinate is used as comparison parameter.

Making the transition from the static domain into the kinematic domain makes the testing procedure more difficult. This includes the transition from a reference point into a reference geometry and a tripod is no longer suitable for such a task. The coordinate is now a function of time.

Furthermore sustaining the advantages of portability, flexibility, multiplicity and statistically in the kinematic domain makes the design of an equipment similar to the tripod, very difficult.

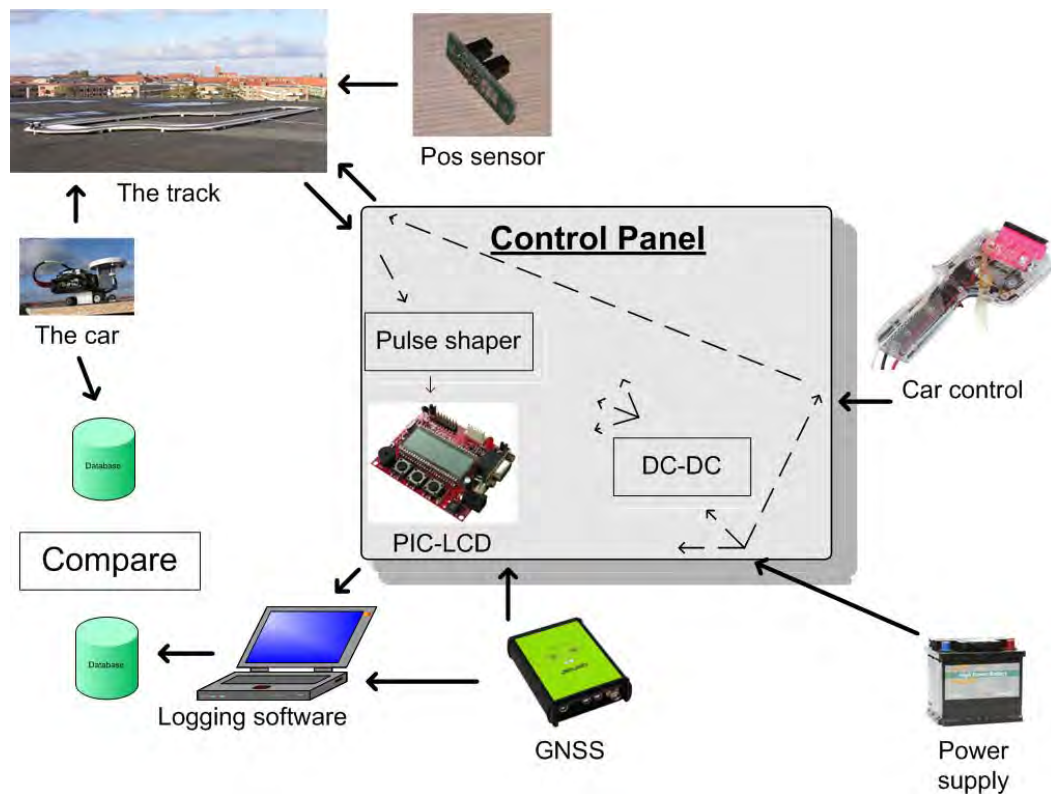


**Figure 1: The over all system design for the GNSS kinematic slot car test track.**

However in this paper a solution to the tripod in the kinematic domain is suggested in form of a prototype of a slot car track. The design and verification of the track is described. The solution consists of several plates to hold the geometry fixed in the time domain and an external logging system to locate the car, including the testing equipment, in the reference geometry as function of time.

### THE OVERALL SYSTEM DESIGN

In Figure 1 is the overall system design for the produced slot car test track illustrated. The system can be split up in the following main components:

- The track
- The car
- The position sensors
- The control panel, including a pulse shaper, a microcontroller, and the car control
- The logging software
- Time synchronization

In the following each component will be detailed described with focus on the function, performance and accuracy of the test track.

### THE TRACK

The track has been made of standard plates (244 x 122 cm.) of 16 mm. chip/particle board with melamine on each side. These large plates have been cut into different kind of plates listed below

- 2 x 180 degrees
- 4 x 90 degrees
- 6 x 45 degrees
- 19 x Straight

to form a maximum length route of 27.7 m. The plates can be assembled in various ways to setup different routes, which sustain the flexible property of the track.

On the top side two slots have been routed on each plate 100 mm. apart. A CNC router, has been used, which has an accuracy of app. 1/10 of a mm., see BENI (2009) for further details of the used CNC router. Copper tape has been fastened along each side of the slot providing the power to the car and along the tape the plates has been painted with an extra hard paint to make the surface rough.

On the back side of the plates routing has been performed to hold all the wiring apart of each other. Small holes along the two slots have been made to fit the designed position sensors. The sensors are separated by 20 cm. on the straight plates and by lengths between 10-14 cm. on turn plates, to give a better registration resolution in the turns.

The plates are assembled using dowels to ensure that the slots on the assembled plates are in the correct position, both horizontal and vertical and a clip is used to fasten the plates together in a firm way. This assembly ensures that the complete assembled track can be considered as one stiff system.

The turns have been designed in a specific way; see Figure 2, for an example of the 90 degree turn. Along the curve three different radiuses is used in order to make the entry and exit of the turn smooth and more coherent with the way actual roads are built. The other turns have been designed using the same principle. The location of the position sensors are also illustrated in the figure.

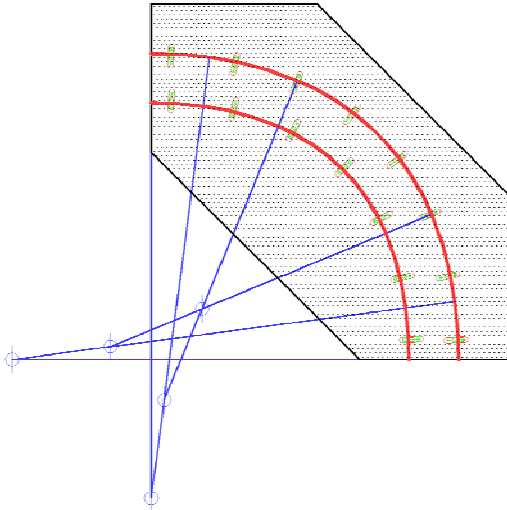


**Figure 2: Exit end entry radiuses for the 90 degree turn plates.**

The power and the direction of the car for each slot can be adjusted individually, hereby sustaining the multiple and flexible property of the track. Two cars can be tested on the exact same time switching the direction of each car individually. Furthermore ensures the routed accuracy of each slot, that the statistical property is sustained since the car is travelling in the exact same slot by repeating rounds.

## THE CAR

The used car is a standard Ready-To-Run, R2R, slot car from Parma PSE, see Parma PSE (2009) for a detailed description. The standard chassis is slightly modified in order to fasten a mount to hold the test equipment. Different motors, different motor pinions and gearing can be adjusted in order to make the driving capabilities of the car as desired. For instance if the weight of the test equipment is high, the car can be optimized to drive slower, but with a higher torque. On the other hand the car can be adjusted to accelerate faster or drive with higher overall speed as desired for the test. An example of a fully equipped slot car can be seen in Figure 3.

In the front of the car a tap is sliding into the track slot and the car is rotating around this point while moving along the track. This point is defined as the reference point, and will remain well known no matter how the car is rotating. Therefore has the GNSS antenna phase center been fixed just above this point.

The testing equipment shall be fastened to the mount on the car including GNSS receiver and antenna, cables and power supply.



**Figure 3: The R2R slot car fully equipped with GNSS testing equipment**

To give a feeling of the kinematic properties for the car, average and maximum velocities for a R2R car with no equipment on and for a car optimized for driving with a total of app. 800 g. is listed in Table 1. These values are however very dependant on the driver capabilities and the assembly of the tested route.

	Average [m/s]	Max. [m/s]
<b>R2R car setup</b>	2.9	6.8
<b>Total weight of 800 g.</b>	0.5	2.1

**Table 1: Average and Max. velocities of the car for different weights.**

Maximum total weight of the car and testing equipment with the current available motors and gearing is app. 1.5 kg.

## THE POSITION SENSORS

Position sensors have been placed on each plate at known coordinates. When using the sensors the car can be positioned at the time the car passes the sensor. The car detection principle for the position sensors are based on an opto coupler. That is when a car passes, an infrared light is broken, which cause the out coming signal line to go high.

The tap on the slot car is app. 20 mm. long, resulting in an out coming pulse width of app. 20 ms. for a car passing by with a velocity of 1 m/s.

The signals from the position sensors use the same wire one for each lane, so the individual sensor cannot be determined only by looking at the out coming signal. Instead a separate sensor has been placed in each lane in order to detect rounds. When a round is detected the counted pulses can be compared to the known number of position sensors. If correct the individual position sensor can be identified by the sequence in which the pulses arrive. The total number of signal lines are therefore 4, two for each lane. In total 352 position sensors have been implemented in the plates.

## THE CONTROL PANEL

A control panel has been built in order to assemble the different wires in the system and to control which part of the system which is turned on and off. The power consumption for all the sensors can be rather high, so switching off unused sensors will ensure that the battery is not drained too quickly, thereby extending the testing period in cases where a permanent power supply is not present.

A pulse shaper, a microcontroller and a DC-DC converter is placed inside the control panel. The position sensors, the microcontroller and the pulse shaper need 5 V., while the external GNSS receiver and the car need 12 V. to operate.

The control panel also holds the connection for the hand speeders (to control the speed of the cars) and the connection to the logging software on a laptop via DB9 serial communication.

## THE PULSE SHAPER

The signal lines can in this implementation be considered a huge antenna picking up all kind of electromagnetic noise. That is noise from the motor on the car as well as noise external to the system.

This noise is different in shape, size and width and has shown to cause false detections of a passing car.

To filter out this noise a pulse shaper has been designed. There are 4 identical ports and in Figure 4 is the principle for a correct detected pulse via the pulse shaper illustrated for one port.

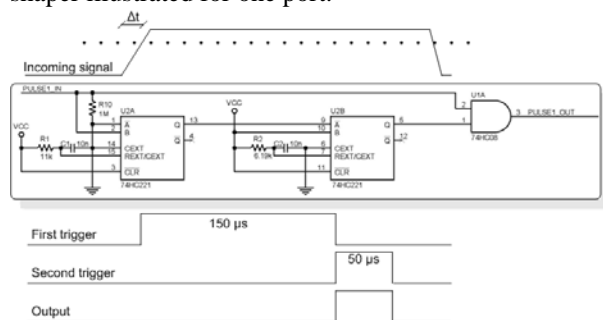


**Figure 4: Correct detection of a pulse via the pulse shaper.**

When a pulse is detected on the incoming line, whether this is noise or not, two one-shots are triggered. On the IC circuit there is a Schmidt Trigger, so only Voltages above 3.3 V is considered. This is illustrated by the dotted line on the incoming signal. The first one-shot outputs a pulse with a width of app. 150 μs. On the falling edge of this the second one-shot is triggered, which has a shorter length. The second one-shot and the original signal line is compared using an AND gate, thereby outputting a pulse to the microcontroller if the original signal line has a width larger than the first one-shot.

Spikes and pulses with a width shorter than the first one-shot are removed in this way, unless a spike occur twice with the second spike in the time window of the second one-shot. Therefore is the width of the second one-shot small and the width of the first long.

With the implemented pulse shaper, the considered noise has shown to be removed and the success rate of pulse detection is sufficient to count the correct number of position sensors for one round detection.

The  $\Delta t$  and the width of the first one-shot will cause a detection delay later on in the microcontroller. The  $\Delta t$  are small, app. 10 - 20 μs and varying, but will not contribute significantly on the coordinate of the car. The width of the first one-shot can be considered a constant, which can be subtracted from the registered time.

## THE MICROCONTROLLER

The microcontroller used is a PIC18F8490 from microchip placed on a development board called PIC-LCD, see Olimex (2009) for further details.

The microcontroller is part of the time synchronization procedure, described later. It receives pulses from the the 4 signal lines from the track and pulses coming from the external GNSS receiver as a pulse pr. second, PPS. In order to detect the pulses as quick as possible interrupts are used.

The internal oscillator in the microcontroller is used as the timing and it has a time resolution of 0.03 ms. corresponding to 32768 oscillations pr. second. Considering a speed of the car on 10 m/s, this results in a resolution in the horizontal domain of 0.3 mm., which is considered to be in the noise limit.

The external GPS receiver is set up to output a pulse per second, PPS, and each time a PPS is detected the internal oscillator in the microcontroller is reset.

When a signal from a position sensor is detected the fractional part a second can be stored and outputted to the logging software.

## TIME SYNCHRONISATION

The actual time synchronisation to the desired reference time is performed in the logging software, see Figure 5. The input needed for this is coming from the external GNSS receiver as well as the microcontroller.

One input line from the microcontroller to the logging software consists of an ID and a number. The ID can be 5 different values

- A PPS
- A pulse on lane 1
- A round on lane 1
- A pulse on lane 2

- A round on lane 2

The number holds the integer value of the microcontroller oscillations. This value is transformed to decimal seconds in the logging software by dividing it with 32768. For the PPS line, the number will be zero.

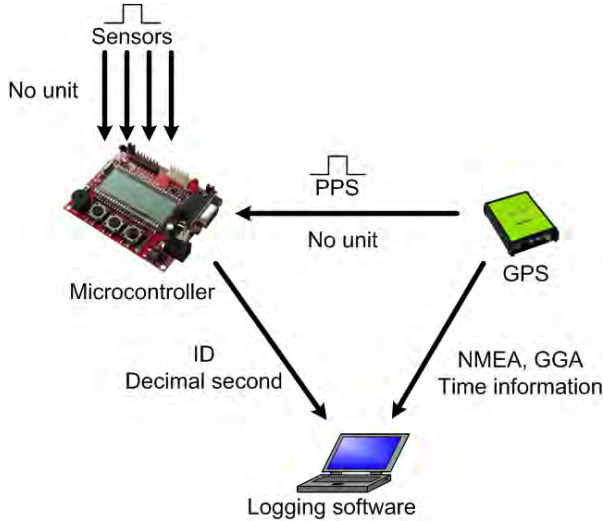


**Figure 5: The time synchronization procedure.**

One input line from the external GNSS receiver to the logging software consists of a GGA line in the NMEA 0183 format outputted each second, see NMEA (2008) for further details. This line holds information of the GPS time, position, and fix and is always outputted after the PPS.

By using the information from these two lines the integer second from the GGA line can be assigned to each PPS from the microcontroller line. The decimal value of a second of the triggered position sensor can then be summed and the GPS time synchronisation is complete.

## THE LOGGING SOFTWARE

A logging software has been programmed in order to keep control of the current test and of the current track. The software is programmed in c# using the Object Oriented Analysis and Design, OOAD, approach.

The main function of the software is basically a database to store useful rounds. In Figure 6 a screen dump can be seen.

Verification of the time synchronisation is continuously performed by verification of the incoming GGA line and by ensuring that the time information in the GGA line corresponds to the number of received PPS lines from the microcontroller.

When a logging session is started the software continuously verifies the correct number of position sensors, when a round is detected. In case of a false number an alarm is issued to the operator. The timing information is assigned to the position sensors as well

as a number of parameters. The information given in each exported line is given in the following.

- Sensor number
- Length to previous position sensor
- Length to next position sensor
- Passing time in the reference time frame
- Average speed in m/s since the last position sensor
- x coordinate in the local track coordinate system
- y coordinate in the local track coordinate system

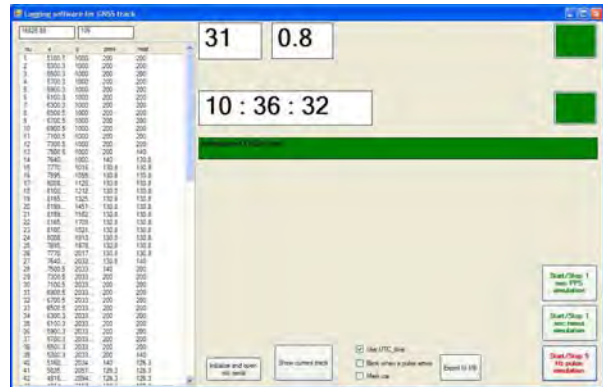


**Figure 6: Screen dump of the logging software.**

The information in the exported file can be used to resample the car coordinate in the sampling rate of the testing equipment on the car. Thereby calculating a reference coordinate for comparison.

Other features have been implemented in the logging software in order to give the operator a better control with the testing procedure:

- Blinking window, when a position sensor is triggered a window is blinking once. This can be used when the exact location of the position sensor needs to be determined. For instance to place the car in order to perform static measurements to position that position sensor in a global coordinate system
- Display of current velocity, in order to give the user a possibility to control the current speed of the car
- Display of current location of the car on a map in real time, in cases where the track is not visible from the location of the control panel

## VERIFICATION OF THE COORDINATES

The position sensors on each plate are placed with known coordinates, that is the neighbouring accuracy of the routing is performed with 1/10 mm. By looking at each type of plate the plate coordinate for the sensor will therefore be known very precisely.

When the plates are assembled the coordinates for each position can be calculated in a local track coordinate system. This is in the ideal world not considering any



production errors and small adjustment of the direction when two plates are assembled.

Therefore a verification of the local system position sensor coordinates for a larger assembled track needs to be verified.

For this procedure special marking blocks have been produced in order to mark the exact triggering point of the position sensor. By sliding this block over a position sensor the exact triggering point can be determined and a tap on top of the block can be used in the survey procedure.

15 blocks have been placed various places at an assembled track with a total length of 16.7 m., see Figure 7 for the test setup. A forward intersection has been used to calculate the local track coordinates for the points, that is angular observations to each block from two free setups and one distance measurement. The accuracy of the coordinates for the blocks using this survey method is assumed to be at the 1/10 mm. level.



**Figure 7: The setup for the verification of the position sensor coordinates.**

A 5 parameter helmert transformation has been performed to transform the coordinates produced by the logging software into the coordinate system of the surveying. The result of this is an average standard deviation of 1.14 mm. on the horizontal coordinates and a scaling factor of 0.999672.

Using these results it can be concluded that an external survey of each position sensor coordinate does not need to be performed each time a new track is set up. Orienting the track in a global coordinate system is enough to determine the absolute coordinates of each position sensor independent of the assembled route.

## VERIFICATION OF THE INTERPOLATION BETWEEN POSITION SENSORS

The output from the logging software is a timestamp for a car pass at a position sensor. In order to estimate the position of the car at any given instance of time, an interpolation between the position sensors need to be performed.

This interpolation can be performed in the horizontal plane, but since the trajectory of the car is well known

and a mathematical relation exist between the length and the local track coordinate, this interpolation can be performed in the 1 dimensional length domain.

A verification of the interpolation has been performed by using a running window of 5 sequential timestamps. The 3rd time observation is excluded from the interpolation and compared to a interpolated value based on the other 4 observations.

The result of this analysis shows a standard deviation of 13.5 ms. which correspond to 6.85 mm., because the car travelled at app. 0.5 m/s during this verification.

The actual needed interpolation is performed using half the distance as in this analysis, and therefore it is concluded that the accuracy of the interpolation is < 5mm. under normal operation. That is no sudden change in the velocity of the car.

## VERIFICATION OF THE FUNCTIONALITY BY KINEMATIC TESTS

In order verify the overall functionality of the designed slot car test track a preliminary kinematic test has been performed. The test is made on the roof of the National Survey and Cadastre in Denmark. The onboard equipment consists of a Delta TRE\_G3T Javad GNSS receiver logging phase data with a rate of 10 Hz. The used antenna is Novatel ANT-A72GLA4-TW-N, a L1 and L2 flight antenna.

Three known local coordinate points on the track has been measured with static observations in order to orientate the track in a global coordinate system.

Two measuring techniques is used

- Precise Point Positioning, PPP using GAPS v3.4, see Leandro (2007)
- Post Processed, PP, kinematic using Trimble Total Control, TTC

A convergence time of 30 minutes is used for the PPP procedure and a reference station placed app. 50 m. away is used in the PP kinematic case. Multiple rounds with varying speed are then performed.

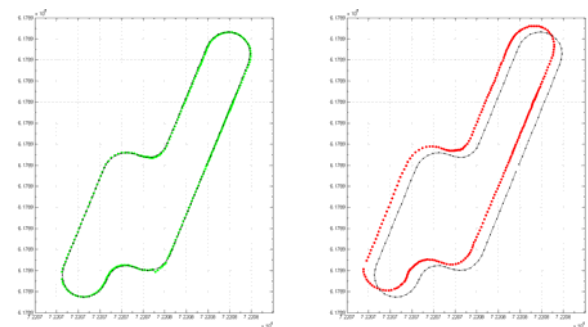


**Figure 8: Results for the first round of the kinematic test. The green refers to PP kinematic, the red refers to PPP, and the black is the reference geometry. The grid size is 50 cm.**

In Figure 8 is the result for the first round illustrated. The two trajectories have the same shape and size, but the PPP is shifted by app. 20 cm.

In Figure 9 is the result for the 10th round illustrated. The absolute accuracy of the PPP procedure is still worse than the PP kinematic, but the results are not at the same place as the first round.

A shift in the horizontal plane from round to round is detected in the data material and can also be inferred from the figures. Whether this is caused by an antenna phase wind up error, a PPP modelling error, or a too short convergence time is unsure, but by using an absolute trajectory this shift can be determined. This illustrates the functionality of the test track.

Looking at the PP kinematic procedure for the 10th round also reveals some deviation from the reference geometry and further analysis could be carried out to investigate the reason.

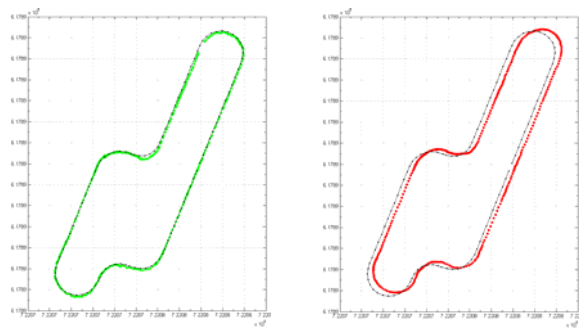


**Figure 9: Results from the 10th round of the kinematic test. The green refers to PP kinematic, the red refers to PPP, and the black is the reference geometry. The grid size is 50 cm.**

In Figure 10 is two graphs shown for a resampled interpolation in the time domain. The left plot shows a correct interpolation, where the velocity of the car is almost constant. Each position from the two methods can be compared to the interpolated value.

On the right plot a troublesome interpolation is shown. The velocity of the car was near zero for app. one second between two position sensors, causing a wrong interpolation. This can however be detected in the data processing, so errors caused by a certain velocity change can be removed.

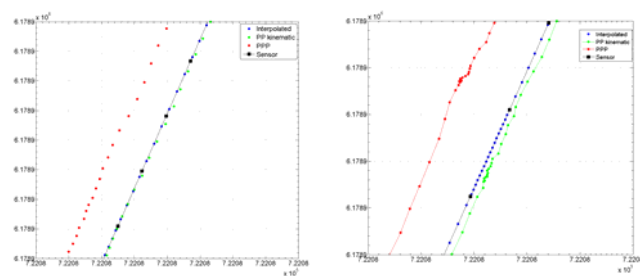


**Figure 10: Correct and troublesome resampled interpolation in the time domain. The grid size is 10 cm.**

## LIMITATIONS OF THE TRACK

Throughout the work the limitations of the test track has become very clear. These include especially the rain due to the chosen material of the track. When performing tests outside the weather prediction must be considered with care and the track shall not be setup, in case of rain.

Furthermore is the chosen design of the plates constraining the geometry of the test track to the horizontal plane. Tests can be performed with a fixed height value, but a true 3D reference geometry cannot be performed.

The interpolation has shown to be the largest error source in the system and should be performed with care. However a trained operator can control the car without large accelerations and a reasonable interpolation can be performed.

## CONCLUSION AND FUTURE WORK

A prototype of a GNSS kinematic slot car test track has been built, tested, and verified with an accuracy of app. 5 mm.

The largest error source in the system is the interpolation error and the reference geometry of the assembled track is at the 1.1 mm. level.

The test track includes, to a certain degree, the advantages from the tripod, that is

- Portability, the track can be transported and set up in various scenarios, both indoor and outdoor
- Multiplicity, two cars can be operated at the same time
- Flexibility, the track can be assembled in various ways and the car can drive in both directions
- Statistical, the well known reference geometry makes a good foundation for statistics by repeating rounds

Several projects for the use of the track are in the pipeline. This includes, among others, mapping of indoor multipath for varying velocity and testing of an onboard unit used in a road user tolling scenario.

## ACKNOWLEDGEMENTS

The following people are acknowledged for their contribution to this work: Michael Hassel Avngaard from DTU Space, National Space Institute, for his ideas related to the electronic implementations. Casper Jepsen, Paul Johan Reiter and Bo Normann Hansen from the National Survey and Cadastre for help during the kinematic test. Henrik and Jan Nielsen from BENI: Furniture production and design for production of the slot car track plates.

## REFERENCES

BENI furniture production and design (2009), CNC router details, <http://www.beni.dk/mask0.html>.

Leandro, R.F., M.C. Santos, and R.B. Langley (2007). GAPS: The GPS Analysis and Positioning Software – A Brief Overview. In *Proceedings of ION GNSS 2007*, Fort Worth, TX. (2007).

Olimex (2009), PIC-LCD development board details, <http://www.olimex.com/dev/pdf/PIC/PIC-LCD.pdf>

NMEA 0183 v4.0 (2008), The National Marine and Electronic Association standard, <http://www.nmea.org>

Parma PSE (2009), R2R slot car details, [http://www.shopatron.com/products/productdetail/1/32+Womp+Womp+Steel+Chassis/part\\_number=572/137.0.1.1.6083.36166.36168.36328.0?](http://www.shopatron.com/products/productdetail/1/32+Womp+Womp+Steel+Chassis/part_number=572/137.0.1.1.6083.36166.36168.36328.0?).



# Appendix D

Jakobsen J, Knudsen P, Jensen A (2010) Analysis of local ionospheric time varying characteristics with singular value decomposition. *Journal of Geodesy* 85(7):449-456, URL <http://dx.doi.org/10.1007/s00190-010-0378-2>.

# Analysis of local ionospheric time varying characteristics with singular value decomposition

Jakob Jakobsen · Per Knudsen · Anna B. O. Jensen

Received: 8 January 2009 / Accepted: 10 March 2010 / Published online: 23 April 2010  
© The Author(s) 2010. This article is published with open access at Springerlink.com

**Abstract** In this paper, a time series from 1999 to 2007 of absolute total electron content (TEC) values has been computed and analyzed using singular value decomposition (SVD). The data set has been computed using a Kalman Filter and is based on dual frequency GPS data from three reference stations in Denmark located in the midlatitude region. The station separation between the three stations is 132–208 km (the time series of the TEC can be freely downloaded at <http://www.heisesgade.dk>). For each year, a SVD has been performed on the TEC time series in order to identify the three time varying (daily, yearly, and 11 yearly) characteristics of the ionosphere. The applied SVD analysis provides a new method for separating the daily from the yearly components. The first singular value is very dominant (approximately six times larger than the second singular value), and this singular value corresponds clearly to the variation of the daily cycle over the year. The second singular value corresponds to variations of the width of the daily peak over the year, and the third singular value shows a clear yearly variation of the daily signal with peaks around the equinoxes. The singular values for each year show a very strong correlation with the

sunspot number for all the singular values. The correlation coefficients for the first 5 sets of singular values are all above 0.96. Based on the SVD analysis yearly models of the TEC in the ionosphere can be recomposed and illustrate the three time varying characteristics of the ionosphere very clearly. By prediction of the yearly mean sunspot number, future yearly models can also be predicted. These can serve as a priori information for a real time space weather service providing information of the current status of the ionosphere. They will improve the Kalman filter processing making it more robust, but can also be used as starting values in the initialization phase in case of gaps in the data stream. Furthermore, the models can be used to detect variations from the normal local ionospheric activity.

**Keywords** GNSS · Time varying ionosphere · Kalman filter · Singular value decomposition

## 1 Introduction

GNSS satellite signals are affected while being transmitted through the ionosphere, the part of the Earth's atmosphere extending from the surface of the Earth to an altitude of about 1,000 km. The effect is a function of the amount of free electrons along the signal path which is measured by the total electron content (TEC). See for instance [Hunsucker and Hargreaves \(2003\)](#) for an introduction to the ionosphere.

The ionosphere is dispersive for radio waves, and for the GPS signals the ionospheric effect is therefore different for the L1 and L2 frequencies. The main effects on the satellite signals are the group delay and the phase advance. These are equal in size, but with opposite sign for the code and phase observations. An introduction to the ionospheric effect on GNSS signals is provided for instance by [Misra and](#)

**Electronic supplementary material** The online version of this article (doi:10.1007/s00190-010-0378-2) contains supplementary material, which is available to authorized users.

J. Jakobsen (✉) · P. Knudsen  
National Space Institute, Technical University of Denmark,  
Copenhagen, Denmark  
e-mail: [jj@space.dtu.dk](mailto:jj@space.dtu.dk)  
URL: <http://www.heisesgade.dk>

P. Knudsen  
e-mail: [pk@space.dtu.dk](mailto:pk@space.dtu.dk)

A. B. O. Jensen  
AJ Geomatics, Brønshøj, Denmark  
e-mail: [aj@ajgeomatics.com](mailto:aj@ajgeomatics.com)  
URL: <http://www.ajgeomatics.com>



Enge (2006). Further, satellite signals can also be affected by small scale irregularities in the ionosphere, which can cause severe amplitude fading and phase scintillation effects. See for instance Yeh and Liu (1982) or Aarons (1982) for an introduction and global morphology of the phenomena.

The ionospheric effect on the satellite signals induces an error which must be handled in the positioning process when GNSS is used for positioning and navigation. With data from permanent continuously operating GNSS reference stations, where the station coordinates are very well estimated, the ionospheric effect on the satellite signals can be extracted and used for ionospheric modelling. Several techniques for estimation of TEC from GNSS satellites signals have been published, see for instance Komjathy (1997) or Schaer (1999).

For grid based regional or global ionosphere modelling various interpolation techniques are used, for instance linear interpolation or multiquadric interpolation as described by Skone (1998). Other examples are statistically based spatial interpolation techniques like kriging, which can be used for the generation of a global ionospheric model (Orus et al. 2005). The use of spherical harmonics for global or large scale models is also well known and discussed, e.g. by Schaer (1999).

Precise ionospheric modeling will improve the accuracy of the position of single-frequency GNSS receivers (Lou 2001). Furthermore precise ionospheric modeling is also important for other space-based observation systems as well as for communication systems and space weather studies. The observed rapid evolution of the ionosphere currently defies sufficient modeling to allow its prediction to future time epochs and therefore studies of its time varying behavior are needed.

The ionosphere, in the midlatitude region, is in its nature varying over time. The main characteristics include the daily cycle with a peak at 14:00 local time and a low, almost constant activity, during nighttime. Further, a yearly cycle with peaks around equinoxes, and finally a 11-year time period correlated with the sunspot number as described in e.g. (Hargreaves 1992).

The speed of the propagation of radio waves depends upon the number of free electrons. The TEC is defined as the number of electrons in a tube of  $1\text{m}^2$  cross section extending from the receiver  $u$  to the satellite  $s$ , see Eq. (1) from Kaplan and Hegarty (2006)

$$\text{TEC} = \int_u^s n_e(l) dl \quad (1)$$

where  $n_e(l)$  is the electron density along the signal path. TEC is measured in TEC units (TECU). 1 TECU equals  $10^{16}$  electrons/ $\text{m}^2$ .

The ionospheric delay,  $\delta_I$  expressed in measurements of carrier phase can be written (to a first order) as in Eq. (2).

$$\delta_I = -\frac{40.3 \cdot \text{TEC}}{f^2} \quad (2)$$

where  $f$  is the frequency of the signal. See for instance Hofmann-Wellenhof et al. (2008).

The TEC has different characteristics for varying latitude and thus an important factor for obtaining a local accurate model is to use data from local GNSS reference stations, as described in Misra and Enge (2006). For instance, in Denmark at approximately  $56^\circ\text{N}$  latitude the length of daylight varies considerably during the year, compared to lower latitudes. Therefore, the daily cycle of the ionosphere varies more over the year. Also, in the case of a real time space weather service, providing information of the local current status of the ionosphere, it is important to have a good local a priori knowledge of the time varying characteristics of the ionosphere. This knowledge can be used to make the data processing in a Kalman filter more robust and to estimate parameters in cases where the filter needs to be reinitialized. The a priori information can be generated by looking at local time series of the time varying ionosphere.

## 2 Data and location

Observations from three dual frequency GPS receivers have been used. The reference stations are located in Denmark with a station separation of approximately 132–208 km. The triangle and geographic relation can be seen in Fig. 1. The GPS observations are stored in the RINEX format with a sampling rate of 30 s, and an elevation mask of  $15^\circ$  has been



**Fig. 1** Reference stations in Denmark used in the data processing

applied. Three stations have been used, instead of just one, in order to provide a better estimate of the ionosphere above the center mark. The stations are maintained and operated by the National Survey and Cadastre in Denmark.

The center mark of the triangle is at approximately 56°N latitude, just below the auroral oval under normal ionospheric activity. During storm periods, the auroral oval can extend to lower latitudes and affect the GNSS signals received in Denmark. During these periods the time varying characteristics of the ionosphere will be different.

### 3 Computation of the time series

A time series of TEC values is computed using a Kalman filter. The principle for the observation model, simplified to include one receiver, is shown in Fig. 2. A single layer model, where the ionosphere is compressed into an infinitesimal shell at the peak of the electron density, is used. In this data processing, the peak is assumed to be at a height of 400 km. The ionospheric pierce point, IPP, is the intersection of the shell and a direct line from the satellite (SV) to the GNSS receiver (U1).

The observation equations for the two carrier phase measurements,  $L1$  and  $L2$ , can be expressed in units of meters for satellite  $s$  and receiver  $u$  as, see Feng (2008).

$$L1_u^s = \rho_u^s + \delta_{orb,u}^s + c(\delta t^s - \delta t_u) + \delta_{I,u,1}^s + \delta_{trop,u,1}^s + \lambda_1 (N_{u,1}^s + \phi_{u,1} - \phi_1^s) + \epsilon_{u,1} \quad (3)$$

$$L2_u^s = \rho_u^s + \delta_{orb,u}^s + c(\delta t^s - \delta t_u) + \delta_{I,u,2}^s + \delta_{trop,u,2}^s + \lambda_2 (N_{u,2}^s + \phi_{u,2} - \phi_2^s) + \epsilon_{u,2} \quad (4)$$

where  $\rho$  is the geometric distance,  $\delta_{orb}$  is the orbital error,  $c$  is the speed of radio waves in vacuum,  $\delta t$  is the clock error

for all components,  $\delta_I$  is the ionospheric phase delay,  $\delta_{trop}$  is the tropospheric propagation delay,  $\lambda$  is the wavelength,  $N$  is the integer ambiguity,  $\phi$  is the initial phase,  $\epsilon$  is the receiver phase noise, including the phase multipath, subscript 1 and 2 refer to the  $L1$  and  $L2$  carriers.

By taking the difference of Eqs. (3) and (4), the geometry free solution  $L4$  can then be expressed as in Eqs. (5)–(7), see Figs. 1 and 2 and the Eqs. (2), (3), and (4).

$$L4_u^s = L1_u^s - L2_u^s \quad (5)$$

$$= 40.3 \left( \frac{1}{f_2^2} - \frac{1}{f_1^2} \right) \text{TEC} + \lambda_1 (N_1^s + \phi_{1,u} - \phi_1^s) - \lambda_2 (N_2^s + \phi_{2,u} - \phi_2^s) \quad (6)$$

$$= cnv \cdot \text{map}(\alpha_u^s) \left( \text{TEC}_{\text{cen,vert}} + \frac{\partial \text{TEC}}{\partial \text{lat}} (\text{lat}_u^s - \text{lat}_{\text{cen}}) + \frac{\partial \text{TEC}}{\partial \text{lon}} (\text{lon}_u^s - \text{lon}_{\text{cen}}) \right) + c_u^s \quad (7)$$

where  $cnv$  is given by  $40.3 \left( \frac{1}{f_2^2} - \frac{1}{f_1^2} \right)$ ,  $\text{map}$  is the mapping function given by  $\frac{1}{\cos \alpha}$  (see Seeber 2003),  $\alpha$  is the zenith angle at the IPP, subscript  $\text{cen}$  refers to the center of the triangle, subscript  $\text{vert}$  refers to the vertical value,  $\text{lat}$  and  $\text{lon}$  are the latitude and longitude,  $c$  is a constant.

The  $L4$  observation consists mainly of the delay caused by the ionosphere. In Eq. (7), this delay is split into three parts in order to represent the TEC at the center point. These are the absolute TEC and the gradients in the latitude and longitude of the TEC. The connection between the slant delays and the vertical is performed by the mapping function.

Another part of the  $L4$  observation is the constant  $c$ . This constant consists of the initial phase for the satellites and receivers and the integer ambiguities. It is assumed that the initial phases do not change from one epoch to another and that no cycle slips occur. It is therefore only the three ionospheric parts, that vary from epoch to epoch.

The number of observations for  $m$  epochs, each with  $n$  visible satellites will be  $n \cdot m$ , and the number of unknowns will be  $n + 3m$ . The unknowns can therefore over time be estimated using a Kalman filter. The Kalman filter is a dynamic filter that essentially can be described by five equations given in Eqs. (8)–(12) (see Welch and Bishop 2006).

$$\mathbf{K}_k = \frac{\mathbf{P}_k^- \mathbf{H}_k^T}{\mathbf{H}_k \mathbf{P}_k^- \mathbf{H}_k^T + \mathbf{R}_k} \quad (8)$$

$$\hat{\mathbf{x}}_k = \hat{\mathbf{x}}_k^- + \mathbf{K}_k (\mathbf{z}_k - \mathbf{H}_k \hat{\mathbf{x}}_k^-) \quad (9)$$

$$\mathbf{P}_k = [\mathbf{I} - \mathbf{K}_k \mathbf{H}_k] \mathbf{P}_k^- \quad (10)$$

$$\hat{\mathbf{x}}_{k+1}^- = \mathbf{A}_k \hat{\mathbf{x}}_k + \mathbf{B}_k u_k \quad (11)$$

$$\mathbf{P}_{k+1}^- = \mathbf{A}_k \mathbf{P}_k \mathbf{A}_k^T + \mathbf{Q}_k \quad (12)$$

In this processing the term  $\mathbf{B}_k u_k$  in Eq. (11) is set to zero, because there is no input from observations outside

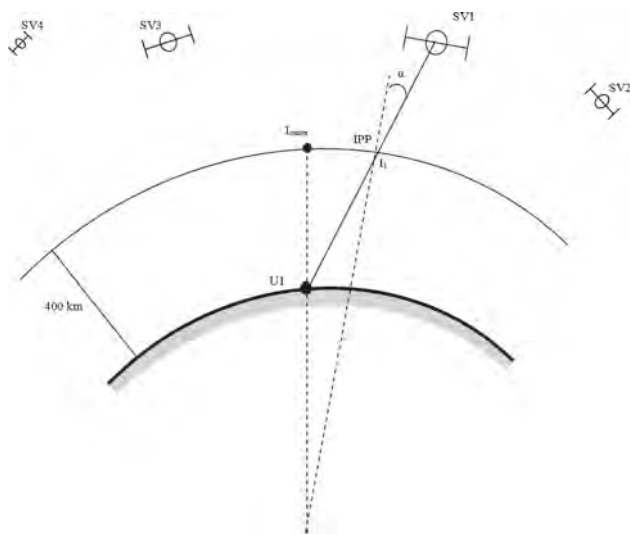


**Fig. 2** Illustration of the observation model for one receiver (Seeber 2003)



the system. The  $\mathbf{A}$  matrix equals the identity matrix, because it is assumed that there will be no change in the ionosphere from epoch to epoch. The connection between the observations,  $z_k$ , and the estimates,  $\hat{x}_k$ , the  $\mathbf{H}$  matrix, is provided in Eqs. (13) and (14). The observations are given in Eq. (7).

$$\mathbf{H} = \begin{bmatrix} \text{cnv} \cdot \text{map}(\alpha_u^{s1}) & \cdots \\ \text{cnv} \cdot \text{map}(\alpha_u^{s1})(\text{lat}_u^{s1} - \text{lat}_{\text{cen}}) & \cdots \\ \text{cnv} \cdot \text{map}(\alpha_u^{s1})(\text{lon}_u^{s1} - \text{lon}_{\text{cen}}) & \cdots \\ 1 & 0 \cdots \\ 0 & 1 \cdots \\ \vdots & \vdots \ddots \end{bmatrix}^T \quad (13)$$

$$\hat{x} = \begin{bmatrix} \text{TEC}_{\text{cen,vert}} \\ \frac{\partial \text{TEC}}{\partial \text{lat}} \\ \frac{\partial \text{TEC}}{\partial \text{long}} \\ c_u^{s1} \\ c_u^{s2} \\ \vdots \end{bmatrix} \quad (14)$$

For an explanation of the remaining variables the reader is referred to Welch and Bishop (2006).

The observation model was implemented in the Kalman filter using Matlab, and nine full years of data from the GNSS reference stations, described above, were processed to obtain absolute vertical TEC values for the center point every 30 s through the 9 years. When a cycle slip was detected the observation from the relevant satellite was reinitialized for future epochs. The parameters for the Kalman filter were saved for every processed hour and reused when a new RINEX file was loaded.

During the processing of the three time series, data gaps in the RINEX files were observed. Values originating from initialization of the Kalman filter immediately after the data gaps, have been removed. The computed TEC time series from the entire period 1999–2007 can be freely downloaded from <http://www.heisesgade.dk>.

The processed time series of vertical TEC has been verified by comparing it to the final global ionospheric maps produced by the International GNSS Service, IGS (see <http://www.igsb.jpl.nasa.gov/components/prods.html> for further explanation). The maps are available every second hour, and the vertical TEC has been extracted at the location of the considered center point for all of 2003. The difference between the two time series has a standard deviation of 1.9 TECU and is normally distributed with an offset of 1.8 TECU. The correlation coefficient between the two time series is 0.96. The IGS maps are global and the long wavelength of the ionospheric variation is weighted higher. An offset to a momentary value from a local model must therefore be expected. This verification of the processed TEC time series is considered satisfactory in order to perform the singular value decomposition analysis.

#### 4 SVD analysis on the TEC time series

The singular value decomposition (SVD) is a technique for decomposing a matrix into a product of three factors. A plot of the elements will reveal recognizable patterns, when the data set corresponds to samples of continuous variables. This is described by, e.g. Preisendorfer and Mobley (1988).

For a given  $m \times n$ ,  $m \geq n$  real valued matrix  $\mathbf{A}$  the equation for SVD of  $\mathbf{A}$  can be written as in Eq. (15) from Parker (2004).

$$\mathbf{A} = \mathbf{U}\mathbf{S}\mathbf{V}^T \quad (15)$$

where  $\mathbf{U}$  is a  $m \times m$  matrix,  $\mathbf{V}$  is a  $n \times n$  matrix,  $\mathbf{S}$  is a diagonal matrix of size  $m \times n$ .  $\mathbf{U}$  and  $\mathbf{V}$  are both orthogonal matrices.  $\mathbf{S}$  is a diagonal matrix of nonnegative values, called the singular values of  $\mathbf{A}$ , and all other values are zero.

The TEC time series, computed using the Kalman filter, has been organized into 9 yearly  $96 \times 365$  matrices, where each of the 96 values per day are the mean over 15 min. Each yearly matrix corresponds to the  $\mathbf{A}$  matrix in Eq. (15). The  $\mathbf{U}$  matrix will correspond to the daily variation and the  $\mathbf{V}$  matrix will correspond to the yearly variation. The SVD is performed using the LAPACK routine (Anderson et al. 1999).

#### 5 Results

An example of the computed TEC time series can be seen in Fig. 3. Three summer days as well as three winter days for 2001, 2004, and 2007 are illustrated. The 24 hour daily signal, the width of the daily peak between summer and winter time, and the size of the daily signal for high, medium, and low ionospheric activity is clearly visible.

In Fig. 4, the result for the SVD analysis is illustrated. Three years (2001, 2004, and 2007) have been chosen in order to represent high, medium, and low ionospheric activity. For the results for all years, the reader is referred to the additional information (electronic supplementary material). The first singular value is illustrated on the left side. A very clear daily signal of the total electron content is observed in the  $\mathbf{U}$  matrix. This is expected as the Kalman filter smoothes the data sequentially, epoch by epoch. The signal has approximately the same shape and magnitude for all the 9 years, which also can be inferred from the figure. It should be noted, that the signal is always positive, meaning that this signal will always be present.

In the  $\mathbf{V}$  matrix for the first singular value, it is observed how this daily signal varies through the year. The signal is noisy indicating that there is a very low correlation of the size of the daily signal from day to day. The signal can be divided into two trends based on the years with high or with low ionospheric activity. From 1999 to 2003 (represented by year 2001 in the figure), the signal is higher during the

**Fig. 3** Example of the computed time series in UTC time for three summer days (Day of year 173–175) and three winter days (Day of year 11–13) in 2001, 2004, and 2007

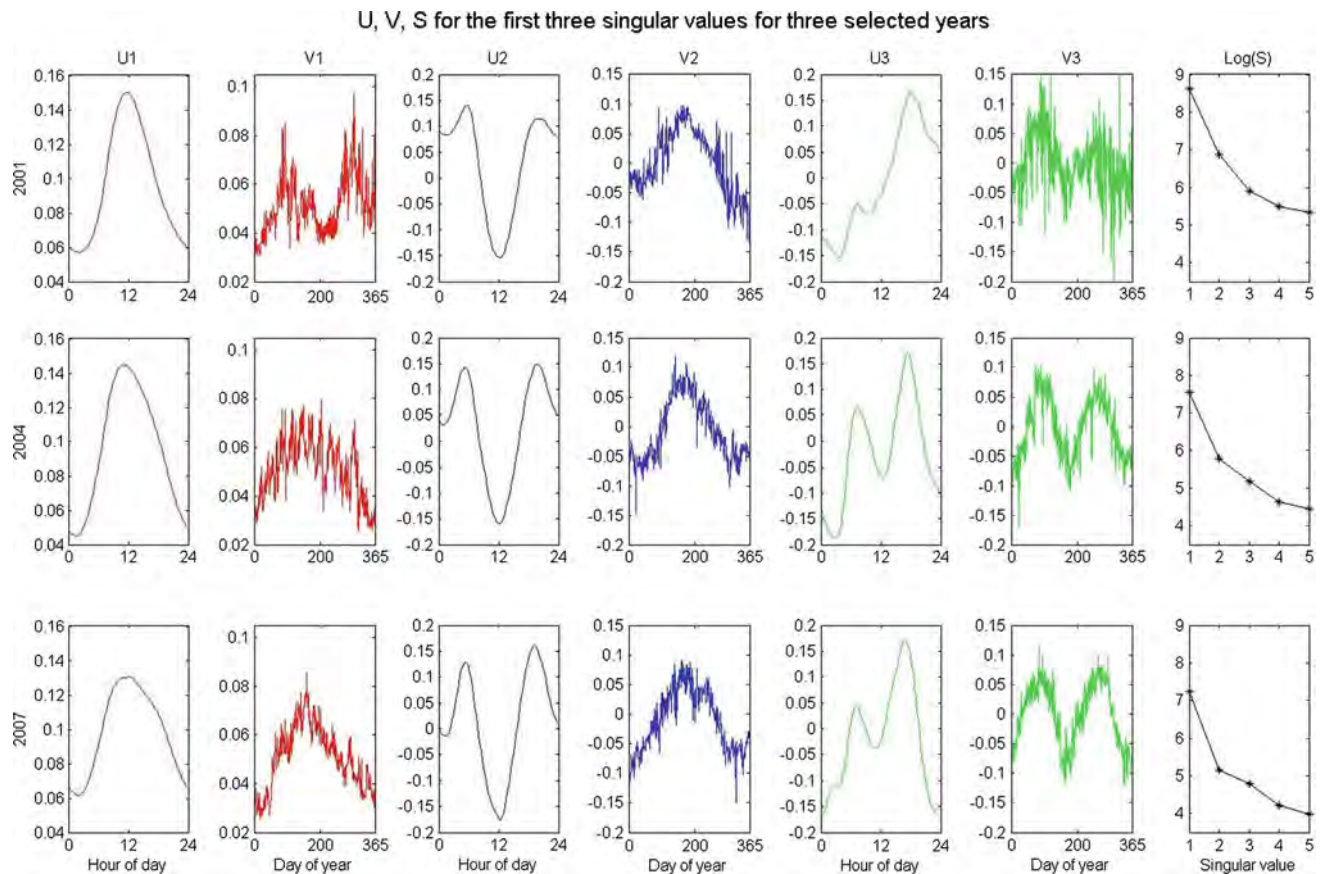
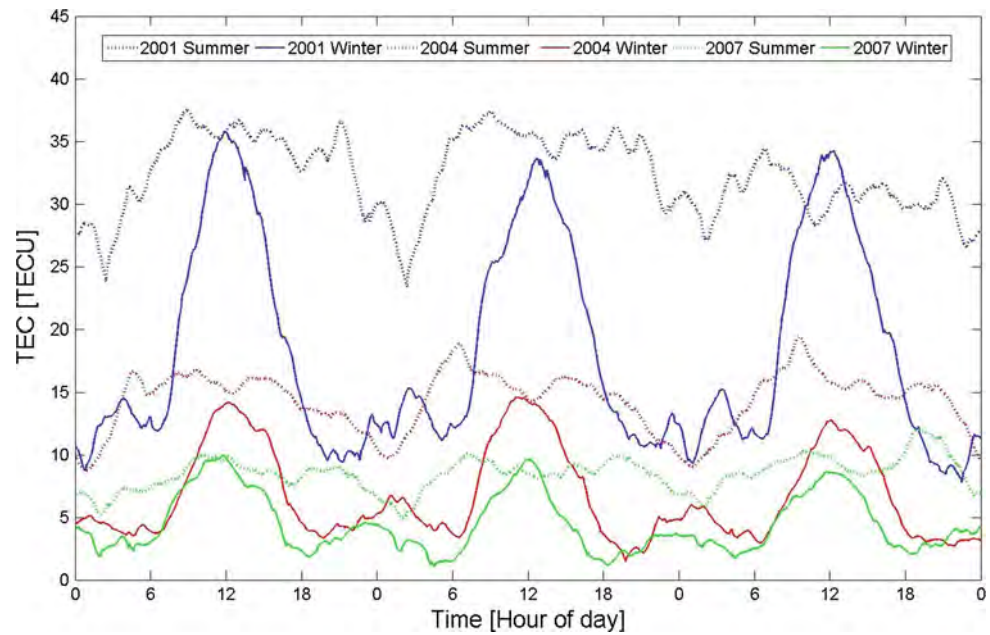


**Fig. 4**  $U$  and  $V$  matrices for the first three singular values for three selected years. The time axis is in UTC time for the  $U$  matrices and in day of year for the  $V$  matrices. The first five singular values in the  $S$  matrix are illustrated to the right

equinoxes and from 2004 to 2007 is the daily signal stronger in the early summer. Furthermore, the signal is less noisy for 2007 than for 2004. This can be interpreted as during

solar max the influence from the solar wind is the dominating factor. This influence is semiannual as described by [Rishbeth et al. \(2000\)](#). During more relaxed solar activity

**Table 1** Correlation coefficients for the singular values for each year and the yearly mean sunspot number

Singular value	1	2	3	4	5
Corr. Coef.	0.96	0.97	0.98	0.99	0.96

years, the UV radiation becomes more dominant indicated by the reduced noise for 2004 and 2007 and the signal becomes annual.

The first five singular values are illustrated to the right on Fig. 4. The ratio between the first and the second is approximately six meaning, that the first singular value dominates the time series for the total electron content. The singular values for each year also show another behavior. Each set of singular values 1–5 over the 9-year period has been correlated with the yearly mean sunspot number. The correlation coefficients for the first five singular values are listed in Table 1, but the remaining singular values (up to 96) show similar behavior. The correlation coefficients indicate a strong correlation of the total electron content with the sunspot number.<sup>1</sup>

For the second singular value, see Fig. 4 in the middle, another clear daily signal is observed in the **U** matrix over the years. The signal is positive in the morning and in the evening and negative during midday. Thus, this signal will determine the width of the daily peak as well as it will damp the peak at 1400 hours local time. The yearly signal in the **V** matrix also shows a clear trend over the years. It is highest in the summer and lowest in the winter. The signal has the same low noise for all three years and the day to day correlation is therefore better. This corresponds very well to the variation caused by the length of daylight in the midlatitude region, which is the same for all the years and varies over the year very smoothly.

The third singular value is shown to the right in Fig. 4. The daily signal in the **U** matrix, shows two maxima. The second maximum is very clear for all the years while the first maximum is similar for the years 2004 and 2007. The signal is both positive and negative, meaning that it will correct the daily signal as shown for the first singular value. It will correct the afternoon depletion of the electron content, so the depletion will appear slower. When looking at the yearly trend, in the **V** matrix, it can be observed that the depletion will be emphasized during the equinoxes. The yearly signal also shows less noise for the years with less ionospheric activity.

For the fourth and following singular values, there are no recognizable patterns over the years in the daily and the yearly signals. They can therefore be considered as noise and will be discarded in the recombination of the ionospheric models.

<sup>1</sup> The used Sunspot Number is the monthly mean number from the Space Weather Prediction Center (<http://www.swpc.noaa.gov/ftpdir/weekly/RecentIndices.txt>).

## 6 Recomposition of yearly ionospheric models

Based on the SVD analysis, where the shape and daily variation over the year was identified for the first three singular values, a model of the time varying ionosphere for each year can be recomposed. The resulting local TEC models for three selected years are illustrated in Fig. 5. The daily signal over the year has been smoothed in order to obtain a yearly trend and to suppress the day to day variation of the size of the daily signal. For an illustration of all the years, the reader is referred to the additional information (electronic supplementary material).

The models clearly illustrate the three ionospheric time varying characteristics. Especially, not only the effect from the 11-year period can be seen with significant higher values for 2001, but also the effects during the equinoxes are more clear during 2001. It can also be verified that the variation caused by the length of daylight is similar for all of the models. The relative effect from the second singular value,

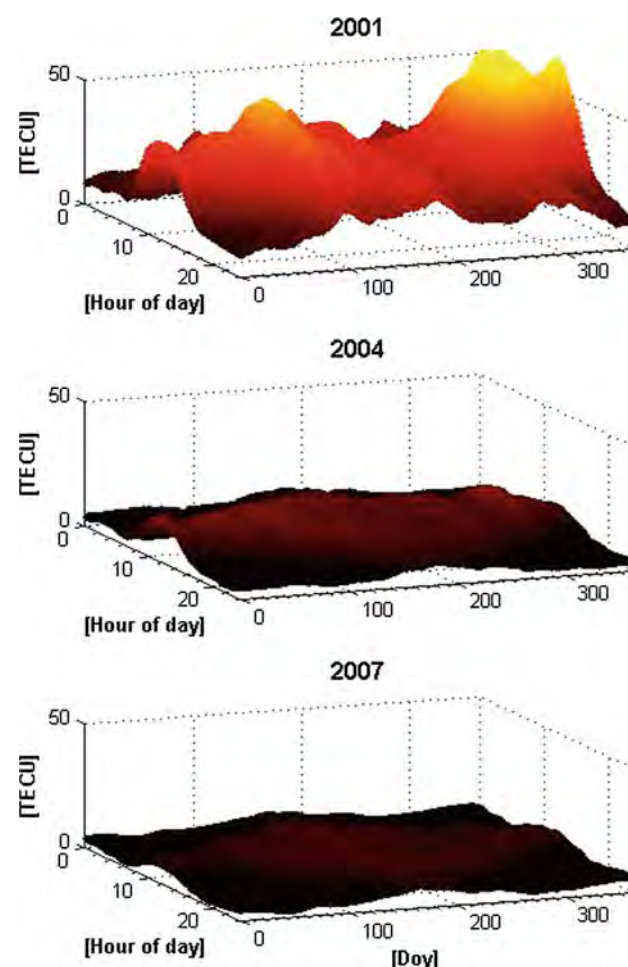
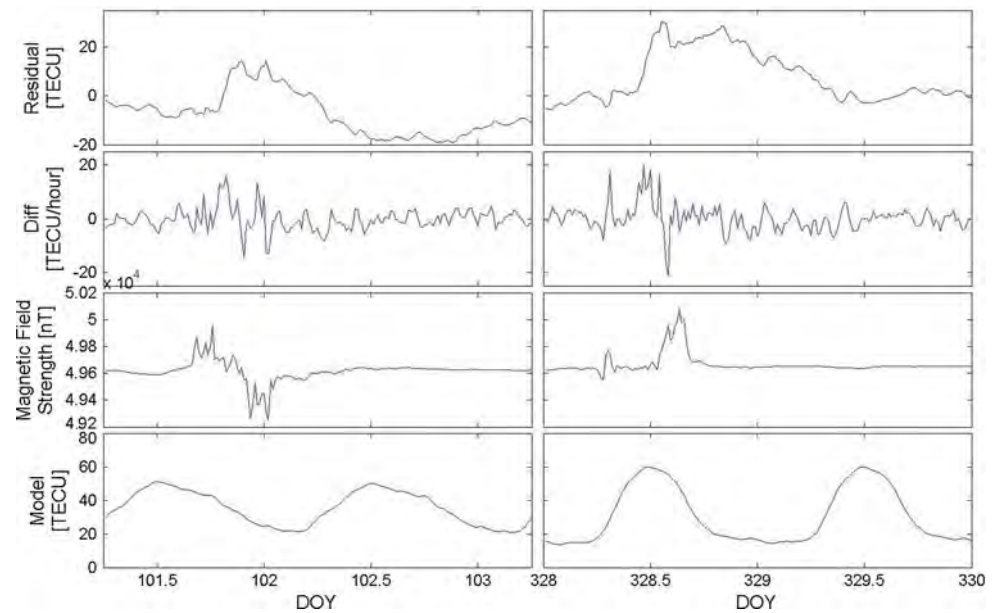


**Fig. 5** Recomposed ionospheric models for three selected years based on the first three singular values



**Fig. 6** Example of two events in 2001. The *first* row shows the residual signal, the *second* shows the differentiation of the residual signal with respect to time, the *third* shows the geomagnetic observation data, and the *fourth* shows the recomposed model



the damping of the 1400 hour local peak, is more visible for 2004 and 2007, than it is for 2001.

An important factor for the time varying characteristics of the ionosphere is the day to day variation. The recomposed models can be used to detect variations from the normal activity, which is of interest for analysis of local space weather studies as well as space weather predictions.

Subtracting the recomposed models from the original time series results in a residual matrix. In Fig. 6, two events during 2001 are illustrated. The first is the evening/night between 11th and 12th of April and the second is in the midday/afternoon the 24th of November. Both events are major storms with high  $K_p$  values and an impact of  $-270$  and  $-220$  nT in the Dst index.<sup>2</sup> The residual signal, the differentiation of the residual signal with respect to time, the geomagnetic observations,<sup>3</sup> and the recomposed model is illustrated for both events.

For the April event, an increase in the TEC from normal activity is observed in the evening, which decreases during the night and becomes negative until the middle of the next day. The differentiated residual signal shows, that the TECU values are fluctuating more in the evening, which are correlated with the local geomagnetic observations. The same correlation between fluctuating TEC and geomagnetic observations are observed for the November event.

These two events also show correlation with global indexes, but this is not consistent for all studied events during 2001. This indicates, that local storms in Denmark can be

detected and using a combination of local TEC observations with local geomagnetic observations will give a more reliable estimation of the ionosphere variation, than when using global indices or models.

## 7 Conclusion and future work

The SVD analysis performed on the computed TEC time series provides a new method for separating the daily from the yearly components. The first singular value is very dominant (approximately six times larger than the second singular value) and this singular value corresponds clearly to how the daily cycle varies over the year. The second singular value corresponds to how the width of the daily peak varies over the year and the third singular value shows a clear yearly variation of the daily signal with peaks around the equinoxes.

The singular values for each year show a very strong correlation with the mean yearly sunspot number with correlation coefficients above 0.96 for the first five sets of singular values.

These three signals, together with the mean sunspot number, can be used to recompose local yearly models of the TEC. In this work, models have been recomposed for Denmark, but the same analysis should be applied at other latitudes and regions in order to validate the procedure and models.

By using a prediction of the yearly mean sunspot number future yearly models can be predicted. This can be used for a real time space weather service providing information of the current local status of the ionosphere. It will contribute to a more robust processing of the Kalman filter by providing information of the general change from one epoch to the next and can be used to generate starting values during initialization of the Kalman filter.

<sup>2</sup> The indices used are from the World Data Center for geomagnetism, Kyoto, <http://wdc.kugi.kyoto-u.ac.jp/>.

<sup>3</sup> Data are downloaded from the World Data Center for Geomagnetism, Edinburgh, for the observatory Brorfelde at latitude 55.625 and longitude 11.672.

The models can also be used to detect abnormal variations in the ionosphere by looking at the difference between the model and the observed value, the residual. A correlation between the differentiated residual and local external geomagnetic observations has been found for a number of events during 2001. This shows the potential for combining these two different types of local observations to provide a more reliable local space weather service.

**Acknowledgments** C. C. Tscherning, University of Copenhagen, is acknowledged for his contribution in the SVD analysis and for his comments through the work. P. Jarlemark from the Technical Research Institute of Sweden is acknowledged for giving access to his expert knowledge of the Kalman filter. The remote Sensing and Geomagnetism group at the Danish Meteorological Institute is acknowledged for making the geomagnetic observations available.

**Open Access** This article is distributed under the terms of the Creative Commons Attribution Noncommercial License which permits any noncommercial use, distribution, and reproduction in any medium, provided the original author(s) and source are credited.

## References

- Aarons J (1982) Global morphology of ionospheric scintillations. *Proc IEEE* 70(4):360–378
- Anderson E, Bai Z, Bischof C, Blackford S, Demmel J, Dongarra J, Croz JD, Greenbaum A, Hammarling S, A McKenney DS (1999) LAPACK users guide, vol 3. Society for Industrial and Applied Mathematics, Philadelphia
- Feng Y (2008) Gns three carrier ambiguity resolution using ionosphere-reduced virtual signals. *J Geodesy* 82:847–862
- Hargreaves J (1992) *Principles of ionosphere*. Cambridge University Press, Cambridge
- Hofmann-Wellenhof B, Lichtenegger H, Wasle E (2008) *GNSS—global navigation satellite systems*. Springer, Wien
- Hunsucker R, Hargreaves J (2003) *The high-latitude ionosphere and its effects on radio propagation*. Cambridge University Press, Cambridge
- Kaplan E, Hegarty C (2006) *Understanding GPS, principles and applications*. 2. Artech House, INC, Norwood
- Komjathy A (1997) Global ionosphere total electron content mapping using the global positioning system. Technical Report no. 188, Department of Geodesy and Geomatics Engineering, University of New Brunswick
- Lou N (2001) Precise relative positioning of multiple moving platforms using gps carrier phase observables. Tech. Rep. 20147, University of Calgary
- Misra P, Enge P (2006) *Global positioning system, signals, measurements and performance*, 2nd edn. Ganga-Jamuna Press, Lincoln
- Orus R, Hernandez-Pajarees M, Juan JN, Sanz J (2005) Improvement of global ionospheric vtec maps by using kriging interpolation technique. *J Atmos Solar Terr Phys* 67:1598–1609
- Parker RL (2004) *Geophysical inverse theory*. Princeton University Press, Princeton
- Preisendorfer R, Mobley CD (1988) *Principal component analysis in meteorology and oceanography*. Elsevier, Amsterdam
- Rishbeth H, Muller-Wodarg CF, Zou L, Fuller-Rowell TJ, Millward GH, Moffett RJ, Idenden DW, Aylward AD (2000) Annual and semiannual variations in the ionospheric F2 layer: II. physical discussion. *Ann Geophys* 18:945–956
- Schaer S (1999) Mapping and predicting the earth's ionosphere using the global positioning system. Ph.D. Thesis, Astronomical Institute of the University of Berne
- Seeber G (2003) *Satellite geodesy*, vol 2. Walter de Gruyter, GmbH, Berlin
- Skone S (1998) Wide area ionosphere grid modelling in the auroral region. UCGE Reports, Number 20123, Department of Geomatics Engineering, The University of Calgary
- Welch G, Bishop G (2006) An introduction to the Kalman filter. Department of Computer Science, University of North Carolina
- Yeh KC, Liu C (1982) Radio wave scintillations in the ionosphere. *Proc IEEE* 70(4):324–360